EXPERIMENTAL VALIDATION OF MICROSEISMIC EMISSIONS FROM A CONTROLLED HYDRAULIC FRACTURE IN A SYNTHETIC LAYERED MEDIUM

by

Russell Roundtree

A thesis submitted to the Faculty and the Board of Trustees of the Colorado School of Mines in partial fulfillment of the requirements for the degree of Doctor of Philosophy (Petroleum Engineering).

Golden, Colorado

Date _____

Signed: _____
Russell Roundtree

Signed: _____
Dr. Jennifer L. Miskimins
Dissertation Advisor

Golden, Colorado

Date _____

Signed: _____
Dr. Erdal Ozkan
Professor and Head,
Department of
Petroleum Engineering

ABSTRACT

A controlled hydraulic fracture experiment was performed on two medium sized (11" x 11" x 15") synthetic layered blocks of low permeability, low porosity Lyon's sandstone sandwiched between cement. The purpose of the research was to better understand and characterize the fracture evolution as the fracture tip impinged upon the layer boundaries between the well bonded layers. It is also one of the first documented uses of passive microseismic used in a laboratory environment to characterize hydraulic fracturing.

A relatively low viscosity fluid of 1000 centipoise, compared to properly scaled previous work (Casas 2005, and Athavale 2007), was pumped at a constant rate of 10 mL/minute through a steel cased hole landed and isolated in the sandstone layer. Efforts were made to contain the hydraulic fracture within the confines of the rock specimen to retain the created hydraulic fracture geometry.

Two identical samples and treatment schedules were created and differed only in the monitoring system used to characterize the microseismic activity during the fracture treatment. The first block had eight embedded P-wave transducers placed in the sandstone layer to record the passive microseismic emissions and localize the location and time of the acoustic event.

The second block had six compressional wave transducers and twelve shear wave transducers embedded in the sandstone layer of the block. The intention was to record and process the seismic data using conventional P-wave to S-wave difference

timing techniques well known in industry. While this goal ultimately not possible due to the geometry of the receiver placements and the limitations of the Vallene acquisition processing software, the data received and the events localized from the 18 transducer test were of much higher numbers and quality than on the eight transducer test.

This experiment proved conclusively that passive seismic emission recording can yield positive results in the laboratory. Just as in the field, this provides one of the best far field (away from the well bore) measurements to assess hydraulic fracture behavior. It also provides a calibration tool to extend laboratory results to field scale endeavors.

The identification of strong microseismic activity at stress states far below fracture initiation confirms that rocks are critically stressed meta-stable materials and that microseismicity is caused by stress changes, not fractures directly.

Advancements are necessary to fully exploit the potential of the microseismic method in laboratory sized samples. Both processing and visualization enhancements are necessary to realize the full benefits of this promising technology in the laboratory environment.

TABLE OF CONTENTS

LIST OF FIGURES

LIST OF TABLES

ACKNOWLEDGEMENTS

As the saying goes, “it takes a village”, but never more so than in the case of deciding to do a PhD in later life. With age one tends to accumulate several not-easily-deferrable obligations, couple that to half the energy level of a younger person, and you have yourself a challenge.

No one can possibly be more instrumental in this dissertation getting done than my Advisor, Professor, Mentor, and Friend; Jennifer Miskimins. Her tenacity, patience, faith, and just plain goodness will mark my life for all of time and for the good fortune of crossing her path.

Another committee member of mine is also worthy and due of some special accolades. Mike Batzle was one of the most honorable and distinguished people I have ever known. Always there and ready to roll up his sleeves and get ‘right in the middle of it’. He was the quintessential ‘Renaissance’ man. Full of theory and practice at the same time. A ball of unending energy that we should all aspire to have. He motivated more people than any other professor I have ever known. It is with great sadness that I did not finish this dissertation before Mike passed away. I hope he can look down on this work and take pride in playing a significant part in it. I only have one other advanced degree, but it was also marked by the loss of someone close to me. There shall be no more.

Sid Green and all the fine folks at TerraTek Labs out in Salt Lake deserve a special mention due to the help, design, and debate about the project and its objectives.

An extra special mention goes to Aniket Surdi, who as a young intern was fascinated with this project and later became one of their experts on the Vallene acoustic emission technology. Schlumberger's acquisition of TerraTek in the middle of this project created some obstacles but these were soon overcome with the help of many within Schlumberger. A special mention goes out to Joel Le Calvez for his advice, interest, and patience along the way.

Of course my family and friends are all just and due a giant thank you for the patience and tolerance of an occasionally 'not-at-my-best' interaction with me while I was playing student a couple decades too late. But a special thanks I must extend to my two wonderful kids; Ryan and Karina. They have held a patience and faith in their father all the way down this path. I had to speed things up at the end to get across the line before they do.

CHAPTER 1

INTRODUCTION

For unconventional petroleum development many oil- or gas-bearing formations are produced from laminated strata through which we must place hydraulic fractures to make them economic. According to the Energy Information Administration (EIA 2009) unconventional gas resources are estimated at 13,427 Tscf which represent 50% of global gas resources, as is illustrated in Figure 1.1. In a recent study by Dong et al. (2011), they estimated gas-in-place in the top 14 major tight gas plays in the U.S. to be between 8,748 and 13,105 Tscf. Figure 1.2 shows the major tight gas plays in the U.S. Since the downturn in commodity prices in 2008, the vast majority of the North American unconventional resource development has been in shale which provide better economics that the tight gas plays active prior to the downturn in gas prices.

Combinations of sandstones and mudstones, chalks and marls, or shales and dolomites or limestones, in laminated sequences are the source of many of our unconventional reservoir rocks today. The constant drive to optimize massive hydraulic fracture treatments in these formations has provided the impetus for the work presented here: to better understand and characterize the behavior of cracks at material property interfaces between lithologies.

Materials science experts have long known that three factors primarily control if, and how, cracks will behave at the boundaries between different materials. These three factors of: stress, mechanical properties, and interface adhesion, are often interrelated as is the case of layered sediments that have become lithified into cohesive rock layers.

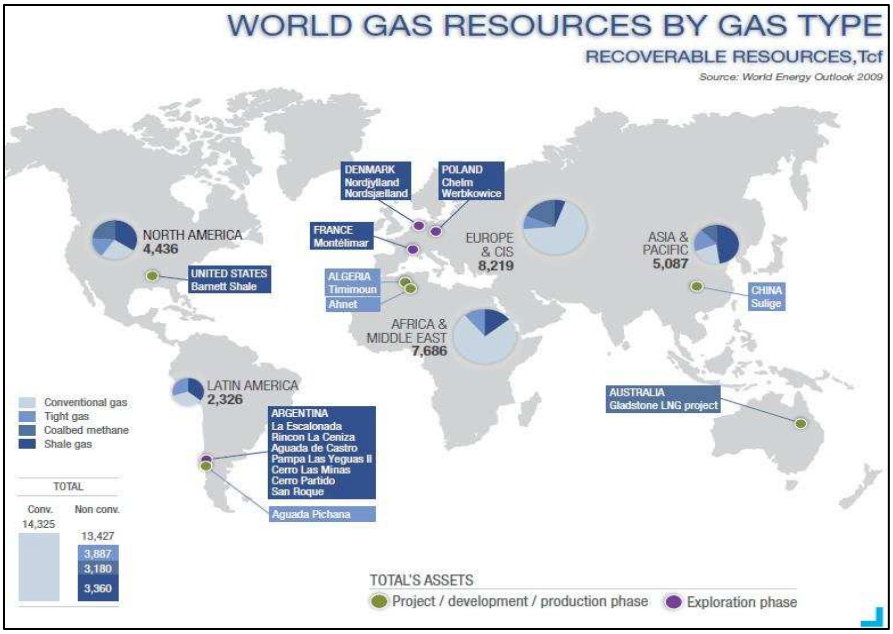

Figure 1.1 - Gas resources in the world as of 2009 (from www.total.com/en/our-energies/natural-gas-/exploration-and-production/our-skills-and-expertise/unconventional-gas/challenges-201901.html, 2012).

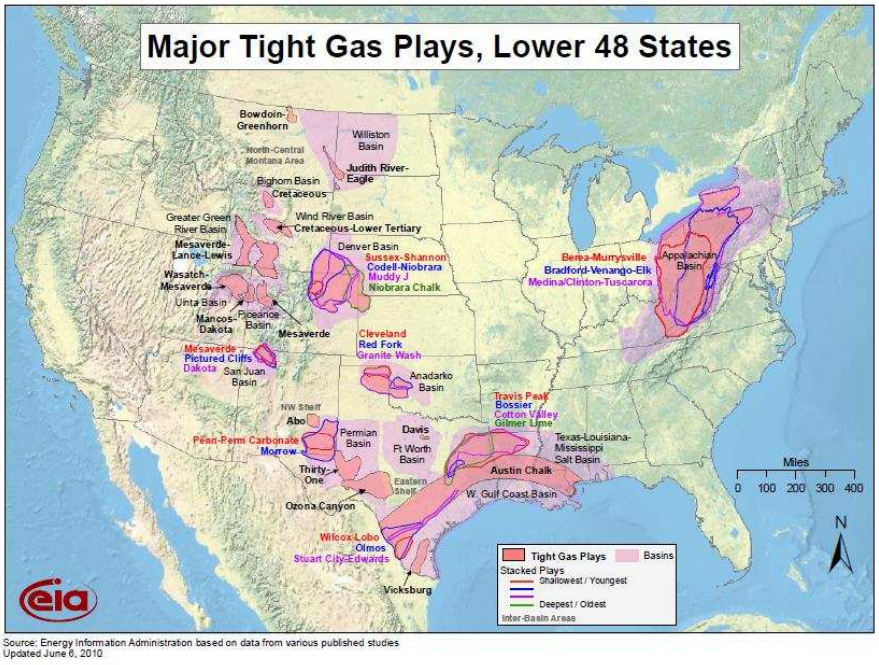

Figure 1.2 - The major tight gas plays in the United States (from www.naturalgas.org/overview/unconvent_ng_resource.asp, 2011).

Distinct layers in rock can often be described as a fractal type of problem with massive units of a primarily dominant lithology and rock fabric almost always containing stringers of a different rock make up. This character continues as one reduces the scale of investigation approaching the level of individual grain layers being deposited. This should not be surprising considering the episodic nature of sediment transport and resulting deposition.

A key factor for the petroleum engineer to understand is how this obviously heterogeneous nature of rock layers will affect the predicted shape and growth of a hydraulic fracture as the tip of the fracture approaches a boundary between lithologies. Much of the analytical work in this area has been done in the aerospace industry where extensive research has been conducted on metals and the boundaries between different types of metal. These efforts on the analytical side have been extended for elastic layered rocks and anisotropic fracture toughness (Nuller et al. 2001). The experimental work here builds on the prior work, both from Delft University (Groenenboom 1998), as well as the three theses from the FAST consortium at Colorado School of Mines (Casas 2005), (Athavale 2007), and (Alqahtani 2010). The research here extends the work with actual rock materials with controlled bonding at the interfaces and investigates the acoustical emissions as the sample is stressed to in-situ conditions and then hydraulically fractured.

1.1 Research Motivation

Early experimental work conducted at TU Delft University, Delft, The Netherlands, investigated how fractures initiated and reoriented away from the wellbore given different orientations of the wellbore and the stress field (Wiejers et al. 1992). The

breakthrough findings in this study were to experimentally see how quickly the fractures can reorient themselves away from the localized stress disturbance invoked by the presence of the borehole (Kirsch 1898). The Colorado School of Mines' FAST Consortium has funded a series of efforts to better understand hydraulic fracture behavior at controlled interface boundaries. Some significant findings from this work were the impact of the permeability of the discontinuity (Casas 2005), the effect of adhesion across interface boundaries (Athavale 2007), and the shear stress induced across material property boundaries (Alqahtani 2010), to hydraulic fracture growth.

The previous FAST work pioneered the use of relatively large (30" x 30" x 36") rock samples loaded in a tri-axial stress frame to mimic in-situ stress conditions of the reservoir. Building on prior results, the work presented here implements the use of small scale microseismic diagnostics to monitor hydraulic fracture growth on laboratory scale samples of real and synthetic rocks. The use of acoustic transducers to detect seismic emissions and localize the source of the seismic energy have been in widespread use in the oil industry as the primary method of microseismic fracture diagnostics now for many years (Warpinski et al. 2001). But the use of this technology in the laboratory is very limited and brings many challenges to the processing of the information that are not the case in field examples.

The goal with this research is to provide an avenue to better understand the hydraulic fracture response in a realistic synthetic rock sample with well understood material interface properties as the fracture approaches the material boundary. Further, during the hydraulic fracturing process the seismic emissions were recorded as the fracture evolved using a similar localization technique to map the dynamic fracture

growth in time and space. The benefit over a field example is that the sample is then disassembled to compare the actual fracture geometry to that indicated by the microseismic emission results. Quantification of the errors one can expect between these two independent measures of fracture geometry is then compared.

1.2 Thesis Objectives

The main objective of this study is to validate the effective use of a small scale seismic monitoring system in physical model study of rock samples in a tri-axial stress frame during hydraulic fracturing operations. The specific behavior of the hydraulic fracture and its geometry are investigated to better understand and predict this phenomenon in the presence of material property differences. Finally, comparing these geometries physically, and through indirect microseismic emission mapping allows us to better understand the degree of error one should expect in actual field measurements of a similar nature. The specific objectives then are:

1. Prove the effective use of a seismic acquisition system in the laboratory conditions for hydraulic fracture testing;
2. Better understand the behavior of the controlled hydraulic fracture as it impinges upon a known material boundary interface; and,
3. Quantify the differences between the physical fracture dimensions and those indicated by indirect microseismic mapping.

1.3 Future Applications

With independent confirmation of the physical model results for hydraulic fractures approaching a material boundary, we may be able to validate our current

analytic and numerical models of this phenomenon. The results may be of sufficient quality to allow calibration of these models to produce better representations of reality in our predictions of stimulation treatments.

The use of microseismic measurements will allow us to assess the level of confidence we can have in the processed results from typical field examples as it is virtually impossible to get actual 'mine-back' results of this scale in the field. Understanding the uncertainty in the fracture geometries predicted by the commonly used, and relatively expensive microseismic mapping process will prevent misinterpretation and give confidence in our conclusions about overall stimulation effectiveness.

Lastly, the use of a passive (microseismic) seismic acquisition system for lab testing is still in its infancy. While several advancements have been made since the original laboratory work was done here, several challenges await the proper acquisition, processing, and interpretation of these results. This experiment was one of the first to explore these challenges and propose solutions to further the use of this technique in the laboratory.

CHAPTER 2

LITERATURE REVIEW

This chapter provides a summary of the relevant publications done by other investigators in the key areas related to this experimental work. In brief, a review of the underlying technologies and processes of hydraulic fracturing, factors controlling fracture height growth, prior laboratory experimental results, use of acoustic monitoring systems, and an overall summary of fracture diagnostics are covered. Brief reviews of the prior results from the other three CSM FAST projects that preceded this work (Casas 2005, Athavale 2007, and Alqahtani 2010) are provided in Appendix A for reference.

2.1 Hydraulic Fracturing

Hydraulic fracturing may be defined as the process of creating a fracture, or fracture system, in a porous and permeable medium by injecting a fluid under pressure through a wellbore in order to overcome in situ stresses and cause the material to fail (Howard and Fast 1970). When the first hydraulic fracture operation was done on the Klepper No. 1 well in 1947 (Howard and Fast 1970), it is very unlikely that anyone could have imagined just how prevalent the practice would become in the coming decades of the US oil and gas industry, nor just how low of porosity and permeability our reservoir rocks would become.

In the early days of hydraulic fracturing, pumping jobs were relatively small (a few thousand gallons of water), used cross-linked polymer agents to create relatively viscous fluid systems, and utilized a host of proppant types to hold the dilated fracture open post treatment (Howard and Fast 1970). Over the years these practices have

been optimized and scaled up such that in today's shale basin development it is not uncommon to use 500,000 gallons of water and 1,000,000 pounds of sand per stage and upwards of 50 stages on today's long lateral wells (Vincent 2013). In general, pumping rates, slurry volumes, and numbers of stages have gone up, while viscosities, proppant size, and stage spacing have gone down.

In most modern horizontal well hydraulic fracturing operations, high pressure pumping units on the surface are combined through a manifold to pump the mixture of fluid, chemicals, and proppant down the wellbore under pressure. This slurry gains pressure from the hydraulic head due to the true vertical depth of the well, but loses pressures due to friction of the slurry against the borehole wall. The well is fractured in stages usually a few hundred feet in length by isolating this portion of the wellbore and establishing connection to the reservoir to begin injecting the slurry into the formation (Vincent 2013).

Operations begin at the toe of the well and proceed towards the heel until the entire reservoir zone has been stimulated. The well is flowed back to recover as much of the injected fluid volumes as possible while leaving as much of the sand propping the fractures open as is possible (Vincent 2013).

For each individual stage a series of events takes place and can be split into three distinct processes: 1) a crack is initiated from the wellbore when the net pressure within the wellbore exceeds the formation breakdown pressure, 2) the crack is extended until either the design volume has been placed or until a screen out occurs due to excessive formation leak-off, or sand pack off within the fracture, and 3) the crack

closes down on the trapped proppant as the fracturing fluids leak-off into the formation (Chudnovsky et al. 2001).

The role of viscosity, wall building properties, and leak-off were well studied by Howard and Fast (1970) albeit fluid systems continue to evolve to this day. Analytic models were derived for linear elastic media being fractured with simple bi-wing fracture geometries using Newtonian fluids (Perkins and Kern 1961 and Geertsma and de Klerk 1969). In the late 1980's the Gas Research Institute (GRI) funded a tremendous amount of research into the assessment, development, and exploitation of unconventional oil and gas deposits. Most of the work was done on tight sand deposits where the assumptions of simple bi-wing fractures was usually appropriate. Factors controlling height growth of these simple fractures were analyzed and the role of both stress changes and material property changes assessed (Warpinski et al. 1990).

With the opening of the Barnett shale, and subsequent shale basins, the nature of the fracture geometries soon demonstrated that fractures in these shale basins were often far more complex than those in the tight sand reservoirs previously studied through the GRI funded research (Fisher et al. 2002). Previously the fracture treatment design goals of length, width, and height were suddenly augmented by also pursuing "complexity" as shown in Figure 2.1. Along with far more complex fracture geometries in these shale basins, the use of low viscosity "slick water" fluid systems was successfully utilized; often with lower proppant loading and smaller proppant sizes than were used in the tight sand fracs previously. The limited examples of mine backs (or coring through a hydraulically fractured zone) showed that rarely was there just one fracture plane,

instead a limited ‘zone’ was fractured with a complex pattern of sub-parallel fractures (Warpinski et al. 1981 and 1993).

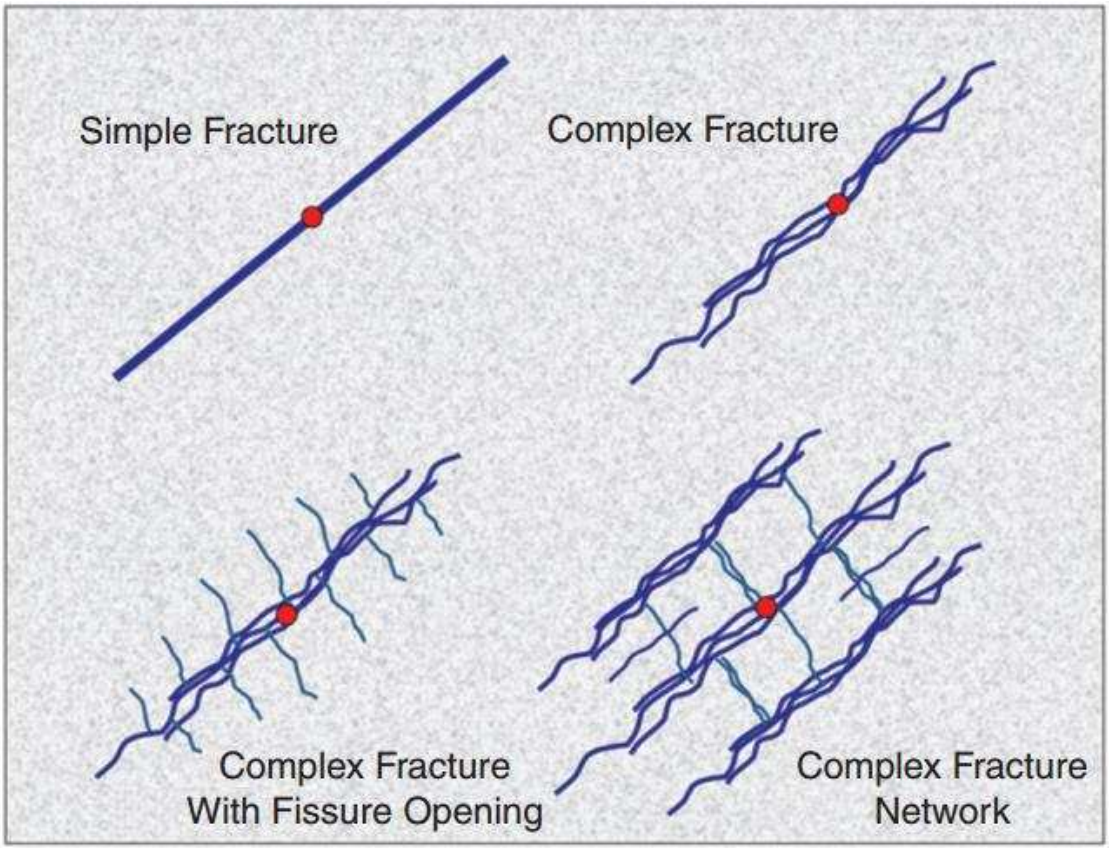

Figure 2.1 – Example of increasing levels of complexity in the created and/or energized natural fracture system from Fisher et al. 2002, “Fracture Complexity Scale”.

2.2 Hydraulic Fracture Height Containment

With limited hydraulic horsepower and available slurry, no other parameter proves to be more limiting in terms of constraining the possible length of stimulated reservoir rock than does the height of the fracture. If fractures grow disproportionately out of zone, they not only rob most of the hydraulic horsepower and slurry for the

stimulation treatment, they also run the risk of communicating with water bearing formations that may render the well uneconomical to produce. Hence, understanding the factors that control fracture height growth and the behavior of fractures crossing lithologic boundaries are paramount to optimizing stimulation treatments.

Cleary (1978) provided perhaps the most significant work in understanding the critical effect of the fracture intensity (K_I) as the fracture tip approaches and crosses a material boundary. In 1982, Warpinski et al. clarified the dominant effect controlling fracture growth across two materials of different properties as being primarily that of stress; not moduli. However, in this same paper the origin or the stress contrasts across material boundaries is in fact often due to a significant change in the Poisson's ratio between them.

Teufel and Clark (1984) analyzed the fracture's tendency to cross a material boundary interface based on the ratio of the shear modulus between the materials supplying the low boundary arrest condition, but also in dilithologic material, found a high contrast arrest boundary due to the induced horizontal stress in the presence of high overburden stress. Hence, two arrest conditions were found with fractures tending to propagate across the material boundaries between these two limits.

Field examples of fracture height growth are difficult to quantitatively identify the mechanism(s) for which fracture growth is arrested vertically but several qualitative investigations have been done. Miskimins and Barree (2003) investigate the potential factors arresting vertical fracture height growth in sandstone/siltstone sequences of the Mesa Verde formation in Wyoming. The conclusion being that a host of factors, such as

shear slippage at the lithology interface, contrasting mechanical properties, and in-situ stress differences across the interfaces are probable causes for the observed behavior. Even in the event that a fracture does cross a lithological interface, combinations of fracture tip blunting, fracture width constrictions, and fracture offsets all contribute to inhibiting overall fracture height growth.

Lastly, Fisher and Warpinski (2011) demonstrate through both volumetric limits in potential height growth for the largest slurry volumes used in the industry, but also in a wealth of height information from microseismic surveys in virtually every North American basin, that hydraulic fractures tend to be very well constrained in terms of height growth. Even in the presence of strong vertical faulting, the possibility of extending fractures vertically to the deepest potable water aquifers is, with any realistic injection volumes and available pumping horsepower, impossible.

2.3 Experimental Laboratory Work

Several investigators have pursued laboratory tests to better understand and characterize hydraulic fracture behavior. Early results tended to be focused on defining the role of stress contrast in controlling fracture orientation and shape (Warpinski et al. 1985). Later, samples of two or three different material properties were used to determine whether the material property differences or the stress contrasts were the dominant factor controlling fracture behavior (Warpinski et al. 1982). In the end it was found that stress contrast is the dominant factor but that stress contrast is usually primarily due to material property differences so they both matter; just one more directly than the other.

In 1984, Teufel and Clark published their important work based off of Teufel's 1979 PhD whereby they were able, in the laboratory, to identify two zones of crack arrest driven by completely different phenomenon (interface containment on the low side and stress containment on the high side). In the range between these two conditions, the fracture could cross the interface between materials.

In hindsight, many of the early lab results were suspect and sometimes conflicting in their conclusions due to improper scaling from field scale to that in the laboratory. In the early days, laboratory parameters were often set to the same range as field parameters. It wasn't until much later that theoretical studies revealed the degree to which these parameter should be scaled to replicate the quasi-static fracture growth in the laboratory that was seen in the field. The papers from de Pater et al. (1994), and later followed up by Bunger et al. 2005, to a large extent provided the theoretical background for properly scaling lab experiments and were the foundation of all the FAST Consortium work laboratory work conducted and discussed herein. But even to this day significant questions remain in terms of the ability to generate a true quasi-static fracture and to understand the size of the process zone about the fracture tip relative to the sample sizes used in most lab experiments.

2.4 Acoustic Monitoring in the Laboratory

Early work utilizing acoustic monitoring to help dynamically characterize the growing hydraulic fracture in the laboratory were focused primarily on active seismic methods (Savic et al. 1991 and 1993). Novel approaches to not only directly map the acoustical impedance contrast created by the advancing fracture, but to also detect the

diffraction off the advancing fracture tip have been used to help dynamically map the fracture in laboratory experiments (Groenenboom et al. 2001).

The mining industry pioneered most the work in the use of measuring passive acoustic emissions as a precursor for rock failure and the safety issues related to this. Adapting these passive monitoring approaches and technologies to the laboratory has been relatively wide spread for rock strength testing and various failure mechanism studies (Fortin et al. 2006).

Combining the passive acoustic emission studies with active seismic tomography to assess the changes in the velocity of the material after either a passing hydraulic fracture or a collapsing pore structure due to very high compression stress has been recently done by Stanchits et al. (2009 and 2011). Changes in the compressional velocity field in the disturbed rock zone show conclusive reductions in velocity in excess of 1% and as much as 10% in the event of complete rock failure.

Utilizing both compressional and shear wave transducers has been reported in the two aforementioned Stanchits et al. (2009 and 2011) papers. However, the utility of the shear wave data is dubious at best due to the extreme ray path variation into both the shear and compressional wave transducers (personal communication, Stanchits, Salt Lake City, January, 2015). In essence, with small blocks in a lab setting, every transducer is going to pick up both compressional and shear wave information regardless of the type of transducer used. This information was not known when the data were collected for the lab work reported in this dissertation.

Granitic samples were used in a laboratory experiment published by Ishida (2001) where both fine grained and coarse grained samples were used. Nine acoustic sensors were placed on the bi-axially stressed block. Two different fluids (water and oil) were used producing significantly different results. The water fluid (1 cp) was found to penetrate existing fracture planes in the rock and propagate the fractures along those planes even though a differential horizontal stress of 6 MPa was present. The viscous oil fluid (80 cp) produced the expected result of propagating a relatively planar fracture in the direction of maximum horizontal stress. Twelve acoustic sensors were placed on the top and bottom of the block. Very sophisticated analysis of the waveform data allowed for source characterization for the different experiments. The water fracture test generated predominantly shear failures from the source characterization of the acoustic events. The oil fracture test generated predominantly tensile events from the same analysis methods of the acoustic data. The urethane sheath provided an approximate even mixture of shear and tensile failure mechanisms. The effect of grain size also had an effect. Coarse grain samples were dominantly shear failures whereas fine grained samples were predominantly tensile failures.

Acoustic emission testing has accelerated since the early days of the research presented herein. Funding has increased for laboratory hydraulic fracture investigations in both petroleum and geothermal applications. At the 31st European Working Group on Acoustic Emissions conference in June of 2014, an interesting poster was given where more controllable fracture growth was able to stop the fracture inside the block. This alleviated the problems described later in this experimental work around being able to stop a growing fracture before it purged its fluid outside the block. This has been

perhaps the most challenging problem with laboratory size samples. In the poster presented at this conference (Molenda et al. 2014) a novel approach was taken to place an impermeable sheath within the borehole preventing 'poroelastic' effects of a fluid penetrating the rock. The authors claim to be able to therefore very precisely control the fracture growth and arrest it within the block. However, this fluid-less fracturing accurately models true hydraulic fractures in the earth remains to be seen.

At the ARMA conference in 2015 Goncalves da Silva et al. (2015) describe the work at MIT using a uniaxial stressed rock sample with two competing slots to establish fractures off the weakness at the tips of the slots when water pressure is increased within the slots. Unique to their experimentation is the use of a transparent window through which low speed cameras photograph the gradual fracture and then a very high speed camera captures the rupture phenomenon once the fracture starts. The optical photography along with eight microseismic sensor data are then used to understand the unique dual slot fracture behavior.

Perhaps the best paper on acoustic emissions published so far is the fine work of Stoeckhert et al. (2015). Their June 2015 paper published in the Journal of Rock Mechanics and Geotechnical Engineering is the finest I have come across. They provide a thorough background to the work they propose investigating: the effect of fracturing on anisotropic solids. The material they chose to represent an anisotropic solid is slate. They compare this to a 'relatively' isotropic solid of sandstone. Using the impermeable sheath method described above they are able to mitigate the effects of the pore fluid propping the fracture as it grows. They articulate the findings of the previous authors of having both stable and controllable fracture growth, but also the ability to

cycle an existing fracture several times. Using the Vallene 5 system, the same system used in the research presented here, they use ten small transducers which they claim give better precision to the localization of events. The fluid-less fracture propagation induces a much higher degree of tensile failures, especially near the borehole. They introduce a novel approach based on first motion polarity statistics to characterize the source mechanism without having access to shear wave data. Using finite element modeling and linear fracture mechanics physics, they are able to quantify the differences between fracture behavior in an isotropic versus anisotropic solid which is corroborated by the experimental data. This is by far and away the most comprehensive acoustic emission paper on experimental hydraulic fracturing tests I have found. Unfortunately, they never used a true hydraulically propped fracture so the effects of using the fluid to extend the fracture are missing from this work.

2.5 Interaction with the Natural Fracture System

While laboratory sized samples can often accurately represent relatively homogeneous rock material, extrapolating these findings to the field scale will always be plagued with the fact that most unconventional reservoirs are naturally fractured to one extent or the other. The formation of hydrocarbon in the source rock and its expulsion pressures usually provide enough drive to naturally fracture unconventional reservoirs. Sometimes these fractures are active shear planes with very high intrinsic permeability. More often they have been completely filled with calcite or some other secondary cement. Sometimes they are a plane of weakness, and at other times they are not.

Potluri, et al. (2005), extends the fracture propagation approach taken by Warpinski et al. (1982) and Teufel and Clark (1984), and extend this analysis to quantify

how these hydraulic fractures can interact when coming in contact with the natural fracture system. Their findings conclude that the proximate factor determining how a hydraulically created fracture will interact with an existing natural fracture system are the differential stress, the angle of intersection, and the fracture toughness. Jeffery et al. (2009), extend the above observations into a 2D fluid coupled model to allow these interactions to be predicted and calibrated in the fracture design process.

Bahorich et al. (2012), and Wu and Olson (2014), have taken the early simple 2D models and developed for 3D models to handle the interaction between hydraulically created fractures and their interaction with a natural fracture system. These models are now quite sophisticated and have been calibrated with microseismic and net pressure history match techniques. It is safe to assume that almost all field scale stimulation efforts in unconventional resource development will encounter and interact with a natural fracture system. Laboratory results will not likely have such an interaction.

CHAPTER 3

EXPERIMENTAL BLOCK DESIGN, CONSTRUCTION, AND PROPERTIES

This chapter contains a description of the design objectives in the construction of the synthetic rock sample used for this phase of the height containment FAST Consortium experiment. Construction details and the resulting blocks physical properties are summarized.

3.1 Construction Details

The primary technology being introduced in this fourth phase of the ongoing study of hydraulic fracture behavior at different material interfaces is the use of an acoustic measurement system to detect the microseismic events produced by the advancing fracture as it impinges upon a material boundary. Synthetic blocks with known mechanical properties were used to test the acquisition system and experimental design. Once confidence was established with the stress loading, viscosity, and fluid rates, the first carefully constructed synthetic block (Figure 3.1) contained a layer of Lyons sandstone sandwiched between two cement sections. Careful preparation and loading of the blocks to closely approximate the in-situ conditions of similar tight gas sand reservoirs being exploited in western Colorado and Wyoming was an important aspect of this phase of the project.

Lyons sandstone was selected as the natural rock material for its ready availability, apparent homogenous nature, very low clay content, relatively low porosity, and very low permeability (Sonnenberg and Weimer 1981). While visual inspection would indicate that the Lyons sandstone has a very homogeneous nature, scratch tests performed by Athavale (2007) on similar Lyons samples showed significant changes in

the compressive strength across the bedding planes (see Figure 3.2). The source of these strong rock strength variations is likely to be the secondary episodic calcite cementation of the hematite coated grains. With these properties, this option was chosen as a natural rock material very representative of tight gas deposits being hydraulically fractured in unconventional oil and gas plays in the US.

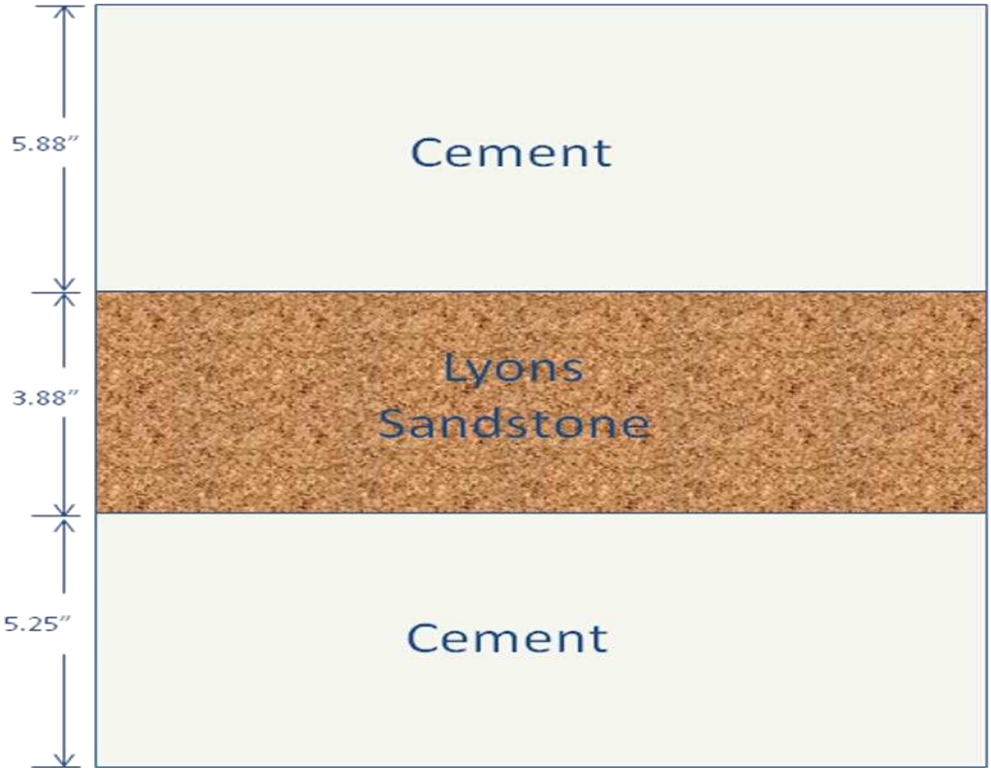

Figure 3.1 – Synthetic layered blocks used in both tests.

Five cement only and two cement with sandwiched Lyons sandstone layered blocks were carefully constructed each to an oversized dimension of 12”x12”x18”. The decision was made to use a 15.8 pound per gallon (ppg) slurry mixture due to the higher Young’s modulus (approximately a factor of two between 15.8 ppg and 16.2 ppg, see

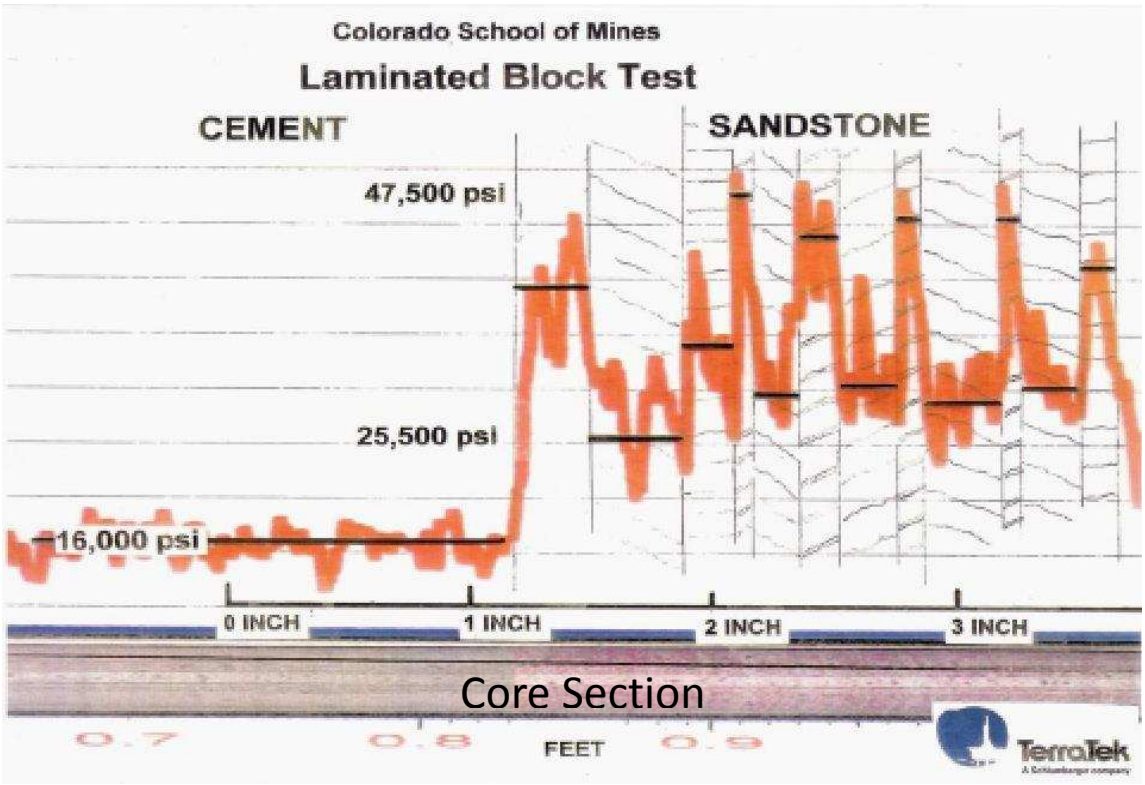

Figure 3.2 – Scratch test showing the compressive strength variability in a core sample of Lyons sandstone (Athavale 2007). The orange line is a measure of the compressive strength (psi) from 16,000 – 47,500 psi.

Table 3.1) contrast with the Lyons sandstone layer (Athavale 2007). Halliburton graciously provided the Portland cement and mixing instructions to comply with standard NIST preparation guidelines (Ferraris 2001). Mixing the cement and water mixture with an agitation device and using the same setting time prior to the slurry being added to the form were exercised as best as is possible under lab conditions.

The wooden forms used to hold the blocks were all exactly the same size of 12” x 18” x 12” internal dimensions with the 18” representing the vertical height of the resulting block. Waterproof wafer board was the material used for the sides and was reinforced with additional material on the outside of the form. The inside surfaces were

then coated with melted-in paraffin to insure a completely sealed form that would not desiccate the cement slurry while it cured.

The top of the form opening was 12” x 18” corresponding to the sides of the block to facilitate constructing the layered block design. In this manner, for the sandwiched sandstone layer blocks, the layer of Lyons sandstone, precut to the 12” x 12” dimension, was slid into the form sitting on edge at the pre-marked locations in the form. This then created a void on each side of the sandstone layer into which the cement slurry was poured. The slurry was poured on each side to an equivalent level as it was filled so as to not move the heavy Lyons sandstone block. Once filled to the top of the form, the cement slurry was vibrated aggressively to remove all entrapped and entrained air to both strengthen the cement and to provide the best possible adhesion to the Lyons sandstone layer. The blocks were kept hydrated with wet diapers for three days as the blocks cured prior to being transported to Salt Lake City for final preparation at the TerraTek lab.

Two cement blocks and the two composite layer Lyon’s sandstone blocks were then cut down to final dimensions of 11”x11”x15” to fit in the small tri-axial load frame at TerraTek as shown in Figure 3.3. The cement test blocks were provided to TerraTek as per their request to allow them to test their equipment with the new acoustic acquisition system and to test the hydraulic fracturing capabilities with different viscosities and rates of fluids.

Once the blocks were cut to the final dimensions, a 1-1/4 inch borehole was drilled in the exact center of the specimen through the top surface. It was drilled to the depth where the fracture was to be initiated in the specimen. A one-inch outside

Figure 3.3 – TerraTek small load frame tri-axial press located at TerraTek laboratories in Salt Lake City, Utah.

diameter stainless steel casing was epoxied in the annulus, sealing the inside of the casing from contact with the rock sample except at the location of fluid injection (Figure 3.4). This 'open hole' section of the borehole was 1".

It was found during the first two tests of the cement blocks that the fracture would initiate horizontally and then try to rotate to vertical. Two remedies were taken to help overcome this stress contrast at the right angle bottom of the cylindrical borehole: 1)

first the bottom of the borehole would be slightly deepened and filed with a plug of epoxy that would form a bit of a meniscus to distribute the load more evenly across the bottom of the borehole, and 2) to facilitate the fracture initiation, and to create a more controllable fracture at lower initiating pressures, a vertical slot was etched with a diamond tool into the formation along both sides of the open borehole section in the orientation of maximum horizontal stress. These two measures rectified the tendency to initiate the fracture horizontally.

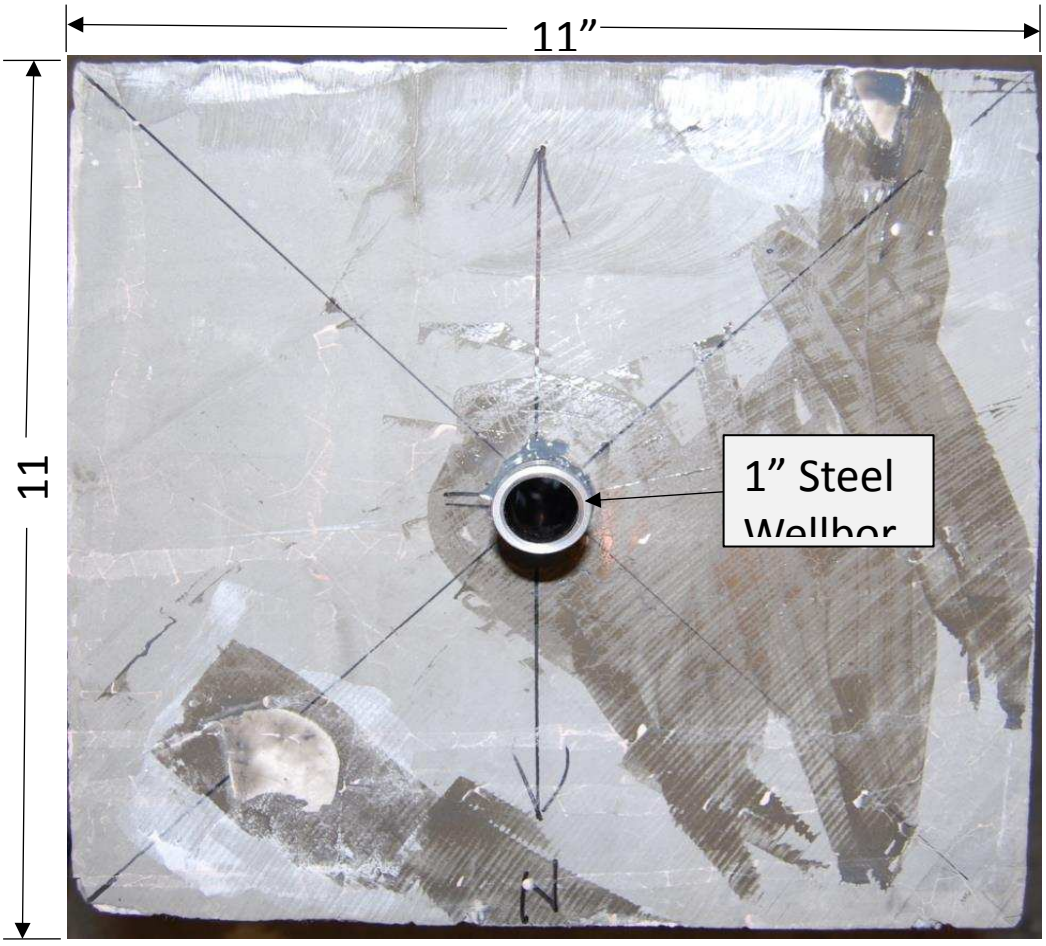

Figure 3.4 – Sample block with 1” borehole casing epoxied in place.

3.2 Physical Properties of Block Materials

With only slight fabrication changes between the blocks prepared for Athavale's 2007 work and the work presented here, the decision was made to not repeat the static moduli testing nor scratch tests that were done in his work (Table 3.1).

Table 3.1 – Athavale's 2007 Block Properties

Material	Static Properties		Dynamic Properties	
	Young's Modulus (psi)	Poisson's Ratio	Young's Modulus (psi)	Poisson's Ratio
Lyon's Sandstone	6.28E+06	0.15	6.09E+06	~0
15.8 ppg Cement	1.29E+06	0.23	2.76E+06	0.15
16.2 ppg Cement	2.20E+06	0.3	3.00E+06	0.16
Epoxy	4.41E+06	0.39	1.76E+06	0.11

However, density, porosity, permeability, and velocity measurements were made on the 15.8 ppg cement and Lyons sandstone samples from which dynamic moduli values were computed (Table 3.2).

Table 3.2 – Physical Properties of Samples

Material	Density (g/cm^3)	Porosity (percent)	Perm (µd)	Vp (ft/s)	Vs (ft/s)	Young's Modulus (psi)	Poisson's Ratio
Cement	1.92	n/a	n/a	12057	7323	3.34E+06	0.21
Sandstone	2.33	12%	51	14219	10267	6.33E+06	~0

Interestingly, the two Young's modulus values for the Lyons sandstone are easily within the experimental error of measurement and the dynamic Poisson's ratio again produces a value of virtually zero in the dynamic test. Perhaps this is due to the complete absence of any pore fluid to increase the compressional wave velocity more than the shear wave velocity in the laboratory samples. Due to the expectation that the cement samples were in fact much more competent due to the removal of entrapped air, and the close correspondence in values for the Young's modulus from the Lyons sandstone samples, the values for the dynamic Young's modulus were used. However, due to the repeated unrealistic values for the Poisson's ratio from the dynamic measurements, static values for the Poisson's ration of 0.21 for cement and 0.15 for sandstone were used in the scaling model computations.

3.3 Scaling Model Results

Performing scale model experiments is a relatively recent achievement in the history of hydraulic fracturing and one that holds much promise. Several analytical models (Perkins and Kern 1961 and Geertsma and de Klerk 1969) are available for simplistic hydraulic fracture geometries under constraining assumptions. These models have provided a framework to guide field scale hydraulic fracture treatment design and have driven incremental improvements over many years. Unfortunately, these models do not, and probably cannot, include the complexities of real world cases. There is not a high degree of confidence in the actual geometry of a field level hydraulic fracture being accurately predicted from the treatment design as modeled.

With very few exceptions (Warpinski et al. 1981), it is virtually impossible to verify the actual fracture geometry for a field level treatment. Models are seen as largely

inadequate to confidently predict actual fracture geometry. The tools available for far field (measures taken away from the bore hole) fracture diagnostics likewise have fairly high levels of uncertainty to quantify actual fracture geometry. This leaves the hope that scale model lab experiments, properly designed and conducted, can provide the actual fracture geometry that corresponds to a specific pumping treatment. The costs and time required to do these laboratory level experiments is small compared to field level tests.

Further, it is possible to cycle through a far broader range of parameter values to validate their impact on the final result. The results of laboratory hydraulic fracturing tests are far from conclusive and occasionally contradictory (Bunger et al. 2005). The reasoning behind this dilemma is the process used to convert realistic field level hydraulic fracture treatment variables, estimates of the rock properties and stress state, as well as the final fracture geometry, to lab scale. Early work by de Pater et al. (1994), attempts to produce a cohesive approach to scale field level hydraulic fracture treatment variables to the lab scale. Bunger followed this with a more robust approach in 2005 which to this day provides the best methodology to properly scale field level hydraulic fracture treatments to the laboratory scale (Green 2015). Both approaches are summarized here.

3.3.1 de Pater et al. (1994) Approach

The de Pater approach is manifested from the original work of defining and using dimensionless groups (Langhaar 1951). Four differential equations were analyzed for 1) crack extension assuming the LEFM (Linear Elastic Fracture Mechanics) assumptions, 2) conservation of mass for fluid including the Carter's leak-off formulation, 3) equation

of motion for fluid flow within the crack (Navier-Stokes), and 4) elastic deformation in response to a viscous fluid pressure. Dimensionless groups were then established for the physical variables in these governing equations in dimensionless form. These dimensionless groups are:

Experimental time: $N_t = \frac{ti}{{r_w}^3}$ (3.1)

Crack energy: $N_\Gamma = \frac{\Gamma}{\bar{\mathrm{E}} r_w} = \frac{{K_{IC}}^2}{4\bar{\mathrm{E}}^2 r_w}$ (3.2)

Elastic deformation: $N_{\bar{\mathrm{E}}} = \frac{\bar{\mathrm{E}}{r_w}^3}{12i\mu}$ (3.3)

Leakoff: $N_{C_l} = C_l\sqrt{\frac{r_w}{i}}$ (3.4)

Confining stress: $N_{\sigma_{hmin}} = \frac{\sigma_{hmin}}{\bar{\mathrm{E}}}$ (3.5)

Where:

N_t = Experimental time

N_Γ = Crack energy

$N_{\bar{\mathrm{E}}}$ = Elastic deformation

N_{C_l} = Leakoff

$N_{\sigma_{hmin}}$ = Confining stress

$\bar{\mathrm{E}}$ = plane strain modulus (psi) defined as $\bar{\mathrm{E}} = \frac{E}{4(1-\nu^2)}$

E = Young's modulus (psi)

i = injection rate (in^3/sec)

K_{IC} = fracture toughness ($psi \cdot in^{1/2}$)

C_l = leakoff coefficient ($in/sec^{1/2}$)

r_w = wellbore radius (in)

t = experiment time (sec)

Γ = separation energy (lbF/in)

μ = viscosity (cp)

v = Poisson's ratio

σ_{hmin} = minimum stress orthogonal to fracture face (psi)

As long as the hydraulic fractures in question are quasi-static, are appropriately parameterized, and the assumptions in the governing equations are valid, one can scale a field level hydraulic fracture treatment to the laboratory scale by finding equivalent values for the dimensionless groups.

For the specific case of a radial fracture in a linear elastic material, with negligible leakoff and fracture toughness, de Pater et al. (1994) derived the following dimensionless forms to model the fracture:

Fracture propagation: $$\frac{r_f}{r_w} = \gamma_r \left(\frac{t}{\tau^*}\right)^{\frac{4}{9}} \quad (3.6)$$

Characteristic time: $$\tau^* = \left(\frac{r_w^2}{i}\right)^{\frac{3}{4}} \left(\frac{12\mu}{\bar{E}}\right)^{\frac{1}{4}} \quad (3.7)$$

Dimension net pressure: $$\frac{p_{net}}{p^*} = \gamma_p \left(\frac{t}{\tau^*}\right)^{\frac{-1}{3}} \quad (3.8)$$

Characteristic net pressure: $$p^* = \left[\left(\frac{\bar{E}}{r_w}\right)^3 12\mu i\right]^{\frac{1}{4}} \quad (3.9)$$

Dimensionless width: $$\frac{b_w}{b^*} = \gamma_b \left(\frac{t}{\tau^*}\right)^{\frac{1}{9}} \quad (3.10)$$

Characteristic width: $$b^* = \left(\frac{12\mu i r_w}{\bar{E}}\right)^{\frac{1}{4}} \quad (3.11)$$

Where: r_f = fracture radius (in.)

τ^*= Characteristic time (sec)

p_{net} = net pressure (psi)

p^* = Characteristic net pressure (psi)

$\gamma_r, \gamma_p, \gamma_b$ = functional coefficients (.083, 1, and 1 here)

b_w = Characteristic frac width at wellbore (in.)

b^* = Characteristic width (in.)

These dimensionless forms allow one to alter the different operating variables to find an equivalent set in the lab that would correspond to an equivalent field level example. The de Pater paper further derives the expression for a radial crack in a linear elastic medium for the fracture intensity as below:

$$K_I = K_{IC} = \frac{2}{\pi}\left[p_{net}\sqrt{\pi r_f} - (p_{net} + \sigma_{hmin})\sqrt{2\pi\omega}\right] \quad (3.12)$$

Where: ω = effective fluid lag zone (in.)

K_I = stress intensity factor (psi·in$^{1/2}$)

K_{IC} = fracture toughness (psi·in$^{1/2}$)

Note the characteristic $\sqrt{r}$ behavior in the first term is for a radial crack. The second term encompasses the complexity involved in the coupling of the LEFM fracture tip and the viscous fluid deformation behind the advancing tip. The ω variable is the lag distance between the fracture tip and the advancing fluid in the crack. For field level examples, this distance is often considered zero and this term is ignored. However, in the laboratory, this simplification is likely to produce invalid results due to the fact that the geometry for a small lab experiment will have a considerable lag distance relative to the fracture length.

If lab determined values for fracture toughness (K_{IC}) are in fact an intrinsic rock property and remain constant regardless of scale, then at the field level scales the fluid pressure component ($p_{net}\sqrt{\pi r_f}$) and the lag zone component ($(p_{net} + \sigma_{hmin})\sqrt{2\pi\omega}$) become much larger than the fracture toughness value. Hence, for field level hydraulic fracture models, the fracture toughness can often be assumed to be negligible and fracture extension is dominated by viscous forces (Mack and Warpinski 2000).

However, at the laboratory scale, the fracture toughness cannot be ignored and in some cases, may dominate the fracture propagation dynamics. This requires the

laboratory setup to be able to create net pressures much higher than the fracture toughness, i.e.,

$$p_{net}\sqrt{\pi r_f} >> K_{IC} \tag{3.13}$$

Another laboratory constraint was discovered by Johnson and Cleary (1991) when they performed lab experiments in zero toughness materials (the crack was already there and the materials were simply held together with a confining stress). They found that at low ratios of confining stress to fluid net pressure (less than three), the fracture extension rate was related to the confining stress. Ratios of confining stress to net pressure above three no longer showed this effect. For this work, all lab experiments use as a base case a pressure differential between confining stress and net fluid pressure of at least three.

Using the de Pater analysis method, Casas (2005) computed a set of scaling factors for the key operating variables in the laboratory experiment as shown in Table 3.3:

Table 3.3 – Calculated Scaling Factors between Lab and Field Scale

Wellbore scaling factor	Time scaling factor	Injection scaling factor	Viscosity scaling factor	Fracture toughness scaling factor	Leakoff scaling factor	Confining stress scaling factor
Sr_w	St	Si	Sμ	SK_{IC}	SC_l	$S\sigma_{min}$
0.214	617	1.60E-05	617	0.463	0.009	1

3.3.2 Bunger et al. (2005) Approach

Casas (2005) was not able to utilize the results from the Bunger paper which was published soon after the scaling analysis Casas did in his work. But the second thesis in the series (Athavale 2007) was able to utilize both approaches. TerraTek seems to be most comfortable with the 'M-factor" type analysis that Bunger introduced in his 2005 paper and is summarized below. Athavale actually uses a hybrid where he first constrains the physical sample size and the experiment time following the guidelines in Bunger. He then uses a classical de Pater approach to compute the equivalent scaling factors.

Bunger et al. (2005), did a rigorous mathematical analysis of the partial differential equations governing a radial crack driven with a Newtonian fluid of viscosity μ, through a permeable brittle elastic solid characterized by a Young's modulus E, a Poisson's ratio of v, a fracture toughness of K_{IC}, and a Carter leakoff coefficient C_l. An interesting difference with Bunger's et al. approach allows one to specify the maximum sample size for the laboratory specimen. This then drives the calculation of the intrinsic fracture length and time scale for the laboratory experiment. These two values must be known a priori in the de Pater et al. approach which is a limitation in the method.

In the mathematical analysis that Bunger undertakes, three distinct regimes of fracture propagation are identified with different governing processes dominating their behavior in each. The system of equations has three invariants ($\mathcal{M}$, Σ, and $\mathcal{C}$) with three characteristic time scales (t_m, t_0, t_c) as follows:

$$M = \left(\frac{t_m}{t}\right)^{2/5} \tag{3.14}$$

$$\Sigma = \left(\frac{t}{t_0}\right)^{1/5} \tag{3.15}$$

$$C = \left(\frac{t}{t_c}\right)^{3/10} \tag{3.16}$$

$$t_m = \left(\frac{\mu'^5 Q_0{}^3 E'^{13}}{K'^{18}}\right)^{1/2} \tag{3.17}$$

$$t_0 = \frac{K'^6}{\sigma_0^5 E' Q_0} \tag{3.18}$$

$$t_c = \left(\frac{K'^4 Q_0}{C'^5 E'^4}\right)^{2/3} \tag{3.19}$$

Where: t_m, t_0, t_c = characteristic time scales

μ' = channel viscosity ($\mu' = 12\mu$)

Q_0 = injection rate (in^3/sec)

E' = plane strain modulus (psi) ($E' = \frac{E}{4(1-\nu^2)}$)

K' = defined as (psi·in$^{1/2}$) $K' = 4\left(\frac{2}{\pi}\right)^{1/2} K_{IC}$

σ_0 = confining stress orthogonal to the fracture face (psi)

C' = modified Carter leakoff coefficient (in/sec$^{1/2}$) ($C' = 2C_l$)

C_l = Carter leakoff coefficient (in/sec$^{1/2}$)

Two fractures are similar if they have equivalent values for the three invariants M, ∑, and C. Hence, the three time scales associated with those invariants, t_m, t_0, and t_c, are the key to selecting the operating parameters for laboratory designed experiments. These intrinsic time scales are all independent of each other in that viscosity only appears in the t_m term, stress only appears in the t_0 term, and leakoff only appears in the t_c term. Each characteristic time scale is associated to a particular aspect of fracture evolution.

Intuitively, the initiation of every fracture will be dominated by the ∑ factor and its t_0 term. This is because at fracture initiation, there is no leakoff yet. Nor is there a fluid filled crack applying fluid pressure to extend the crack. Likewise, it is intuitively obvious that the dominant factor at the end of the fracture is the C factor and its associated t_c term due to the fact that the fracture stops growing when the leakoff consumes all available fluid and conveyed net pressure previously used to grow the fracture. The starting and ending points for the growth of a fracture are known. What is not known is the path taken between them. For this, Bunger et al. introduces a table of states to classify the dominant factor controlling fracture growth for the possible combinations of the three M, ∑, and C invariants as shown in Table 3.4:

According to Bunger et al., every fracture begins with the first state in the list and ends with the last state in the list. How the fracture gets between these two end points is, however, dependent on the treatment variables, the operating practices, and of course, the media. In a Monte Carlo simulation, Bunger et al. however points out that almost all the time the combination of variables will take the fracture down the 'M' paths.

Table 3.4 – Limiting Regimes for Radial Fracture Evolution

	Parameter Values $\mathcal{M}$	Σ	$\mathcal{C}$	Existence Criteria
O	$\gg 1$	$\ll 1$	$\ll 1$	–
M	$\gg 1$	$\gg 1$	$\ll 1$	$\varphi_1 \gg 1, \varphi_2 \ll 1$
K	$\ll 1$	any	$\ll 1$	$\varphi_1/\varphi_2 \ll 1$
$\tilde{O}$	$\gg 1$	$\ll 1$	$\gg 1$	$\varphi_2, \varphi_2/\varphi_1 \gg 1$
$\tilde{M}$	$\gg 1$	$\ll 1$	$\gg 1$	$\varphi_1 \gg 1, \varphi_2/\varphi_1 \gg 1$
$\tilde{K}$	$\ll 1$	any	$\gg 1$	–

Where:

$$\varphi_1 = \frac{t_m}{t_0} \tag{3.20}$$

$$\varphi_2 = \frac{t_0}{t_c} \tag{3.21}$$

Athavale created two synthetic block samples; one of cement and one of a six layer composite block. One limitation of the two scaling techniques presented here is that they only allow one number for the intrinsic rock properties like Young's modulus, Poisson's ratio and fracture toughness. With a highly variable layered rock sample, such as the six layer block, averages of these parameters had to be calculated. Utilizing the knowledge that the maximum stress and the direction of primary material property change was vertically, the method to calculate the properties for the effective medium was to calculate the Reuss bound which corresponds to a constant stress state at the boundary.

Potential errors in this approach are that the volume component of each medium is given equal weight based on its volumetric contribution. One could imagine that the material properties of the rock unit into which the fracture initiates, or the one in which it predominately travels, will have far more bearing on the fracture propagation behavior than, for example, the rock properties of the very top or very bottom rock layer in the six layer stack.

The derived values of the scaling factors for Athavale's work on the pure cement and the composite blocks are given in Table 3.5. Note that Athavale reduced viscosity from about 600,000 cp in the Casas test to 100,000 cp but held the low rates used in the Casas tests.

Table 3.5 – Scaling Factors for Cement and Composite Blocks (Athavale, 2007)

Wellbore scaling factor	Time scaling factor	Injection scaling factor	Viscosity scaling factor	Fracture toughness scaling factor	Leakoff scaling factor	Confining stress scaling factor
Sr_w	St	Si	Sμ	SK_{IC}	SC_l	$S\sigma_{min}$
0.214	507	1.94E-05	507	0.463	0.01	1

Athavale demonstrated the ability to incorporate the recently published guidelines from Bunger to be able to adjust the time and injection rates for the smaller block used in the 11 inch tri-axial press. However, even at rates as low as 1 cm^3/min, the fracture was not contained within the block and purged the fracturing fluid to the outside of the block. It was not clear if this undesirable behavior was due to the rate, the viscosity, or the unbonded interfaces which could have provided a conduit to the edge of the block

without causing the fracture to purge. This dilemma helped guide some of the changes to the block tests presented herein.

The same basic rock materials and scaling approach were taken in this third experiment with a few notable exceptions. One important change was to simplify the complexity of the composite block so only three layers of very well controlled materials were used. Second, to better replicate a material interface subjected to very long term lithification processes and overburden stress, great care was used to get the best possible cement-to-sandstone bond. One theory causing the fracture to blow out the side of the block was that the very viscous fluids were causing a relatively wide aperture crack to form. In an attempt to arrest the fracture while still in the block, a decision was made to lower the viscosity of the injected fluid allowing a narrower aperture crack to form and propagate. In Table 3.6, see the relative scaling factors derived for both of the single layer blocks used in this third laboratory hydraulic fracturing test.

Table 3.6 - Scaling Factors for Both Single Layer Blocks

Wellbore scaling factor	Time scaling factor	Injection scaling factor	Viscosity scaling factor	Fracture toughness scaling factor	Leakoff scaling factor	Confining stress scaling factor
Sr_w	St	Si	Sμ	SK_{IC}	SC_l	$S\sigma_{min}$
0.33	86	4.18E-04	86	0.57	0.01	1

To test this theory, and to get field scaled viscosities closer to those being used in slickwater shale treatments rapidly dominating the industry at the time, the decision was taken to drastically reduce the viscosity from the 100,000 cp used in Athavale's test to just 1000 cp. This would allow a much narrower aperture crack to be created and

hopefully provide a more controllable fracture. To stabilize the quasi-static crack grow with such a low viscosity fluid, the rate was increased to 10 cm^3/min. In summary, viscosity was reduced by a factor of 100 but rate was increased by a factor of ten. The net combined parametric change was a reduction by one order of magnitude.

Lastly, a horizontal cut four inches long and about ½ inch deep was made in the center of the sandstone layer. This would allow, in the event that the fracture extended all the way to the block face, the fluid in the crack to escape through this cut and hopefully preserve the shape and size of the hydraulically created fracture when the block was split open after being removed from the press (Figure 3.5).

Figure 3.5 – Block after fracture showing pressure release cut on the outside of the block.

3.4 Seismic Acquisition

This experiment was the first time the TerraTek labs had attempted recording acoustic emissions for an oil and gas type application. Most of this work has been done in the mining industry or materials science applications to quite different ends. Instead of simply 'picking up noise', which is often the main goal in mining applications to indicate something has moved and may continue to do so, or in materials science to identify where a first failure point needs additional reinforcement, in oil and gas the goal is to identify each and every acoustic emission. Characterizing where it came from, when it occurred and even learn something for the source that generated the acoustic energy in the first place are important objectives.

Seismic work has been done in the laboratory setting for some time by several researchers (Savic et al. 1991) and (Groenenboom et al. 2001), but usually this consists of using a known active source to interrogate the medium and then measure the response. Some success has been reported to detect the advancing fracture tip and also measuring the dilated fluid filled crack behind it.

Passive seismic receiver use in the lab to quantify hydraulic fracturing processes is relatively new and certainly was with these experiments being the first conducted at the TerraTek labs in August 2008 and February 2009. Many aspects of passive seismic recording are the same or similar to those used with active recording (with a controlled source), but there are also differences that will be pointed out along the way.

Two different experiments were attempted at the TerraTek labs. The first was using eight compressional wave (P-wave) receivers. The second was using six three-

component receivers recording a compressional wave and two orthogonal shear wave components (eighteen total channels). There were a couple reasons for pursuing the shear waves. First is that the primary energy source associated with microseisms in the earth is believed to be predominantly shear motion across critically stress discontinuities in the rock. The second reason is that the primary mechanism for locating microseismic sources depends on recording both the P-wave and the shear wave for a specific event and then taking the time difference between those two arrivals to predict a distance to the source.

3.4.1 Seismic Recording System

TerraTek procured and deployed the Vallene AMSY-5 digital control and recording system along with eight channels of low noise preamplifiers and individual 16 bit A/D converters cable of sampling up to 40 Mhz. Each channel has analog high pass and low pass filters to reject noise. The system continuously digitizes incoming signals into a buffer. When a signal crosses a threshold set by the user, the system will take the contents of buffer and flush it to storage. The user can control the threshold trigger, as well as, the length of the leading and trailing window lengths to be stored to disk, as well as, any analog filtering to condition the incoming signals. The system can be seen in Figure 3.6 being bench tested prior to placing the block sample in the tri-axial press.

The decision was made to run the preamplifiers at 34dB of gain due to no one having previous experience in the size of signals expected to see. The recording rate was selected to be 2.5 Mhz with a 25.3 dB threshold and a 2048 sample window. A low pass filter was set at 95 Khz and a low pass (anti-alias) filter was set to 1 Mhz. This

combination of parameters was selected based on successful bench testing of the sample while in active calibration mode.

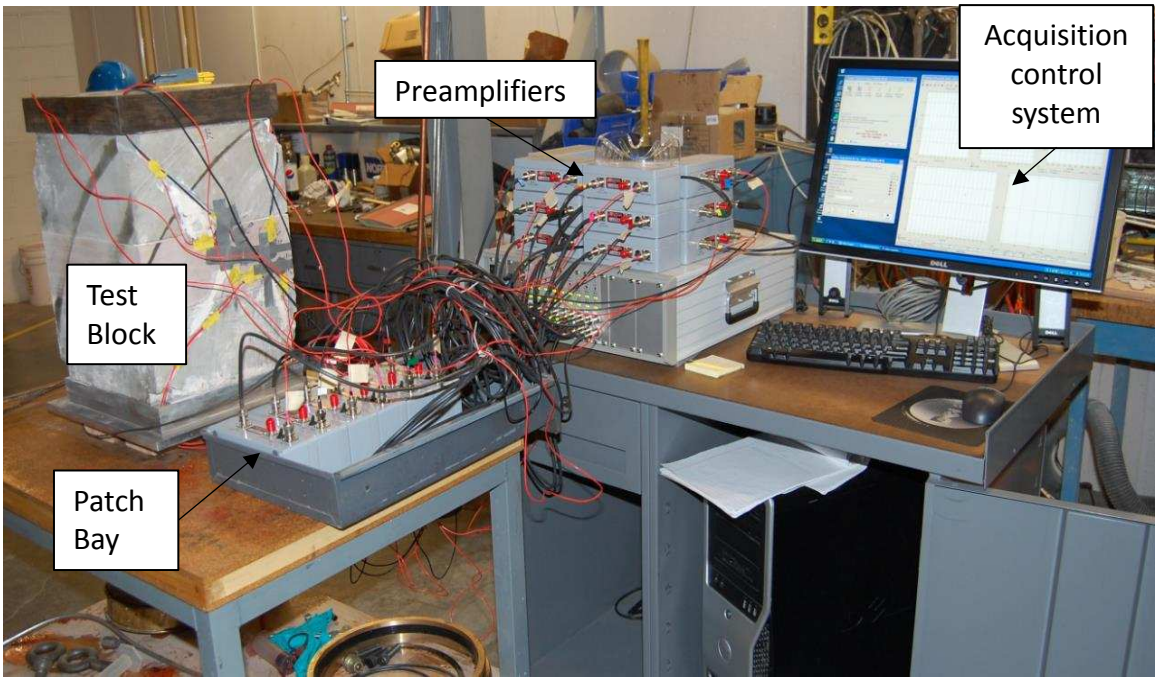

Figure 3.6 – Vallene AMSY-5 acoustic emission recording system connected to one of the test blocks prior to placing the block in the triaxial test frame.

The receivers for the first test were the Dunegan Engineering SE150-M compressional wave receivers. They are made with a fully enclosed and isolated 0.8 inch enclose that is about ½ inch thick. They are of ceramic piezoelectric design with large, sensitive wafers. The shear wave sensors for the second block test were the Dunegan Engineering SH225-M models of similar size, sensitivity, and construction as the P-wave sensors. Due to the fact that the receivers must be inside the tri-axial press, one inch cylindrical cavities a little over a half inch deep were drilled into the sides of the laminated block to facilitate housing the receivers while the sample was under stress

without damaging the receivers (Figure 3.7). The receivers were coupled to the rock face with the use of a small amount of Silly-puddy. Cable channels were also cut into the rock face to protect the cables while in the press. Duct tape was placed over the receivers and cables to hold everything in place loading and unloading the sample from the press (Figure 3.8).

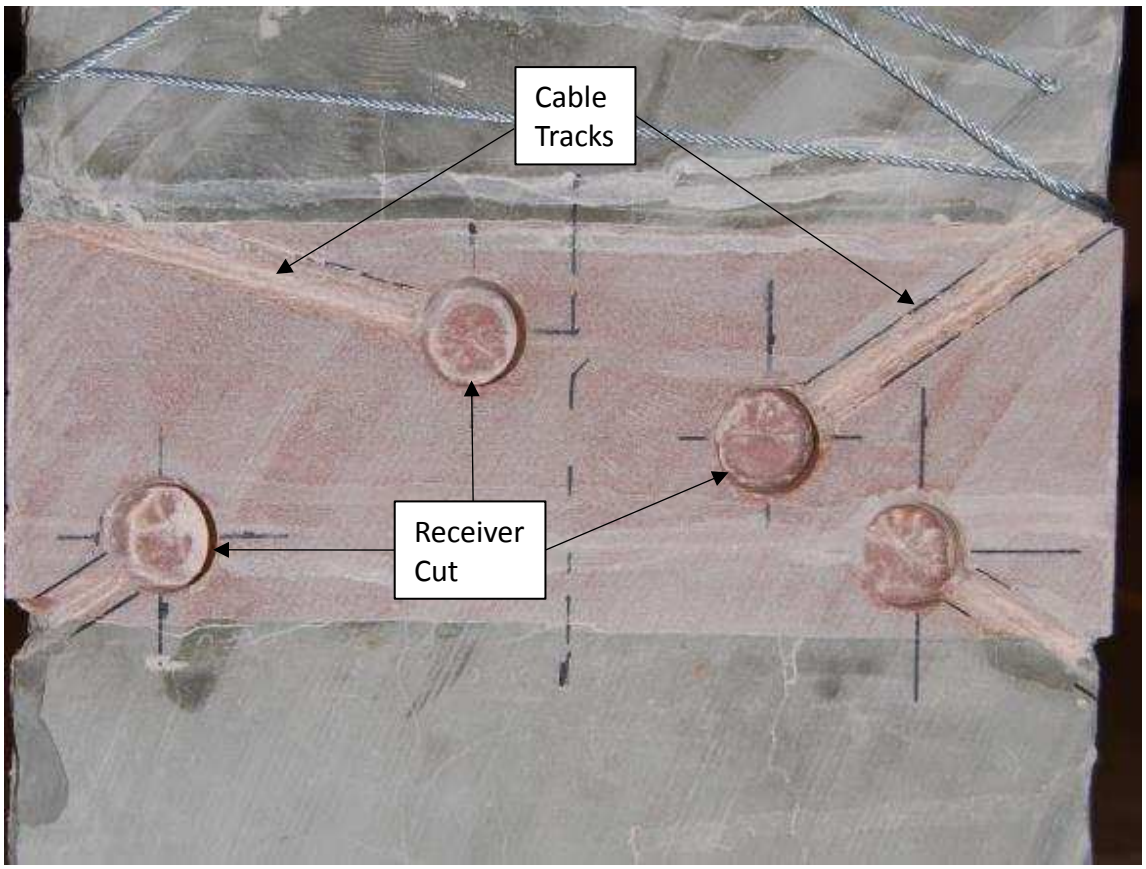

Figure 3.7 – Receiver cut-outs and cable tracks. In this figure, the cut outs are all located in the Lyons sandstone layer.

The Vallene AMSY-5 system has several convenient subsystems to make the work of seismic emission studies much easier. One of these is the ability to either transmit signals by sending an electrical pulse to the receiver, turning it into a source, or

Figure 3.8 – Receivers and cables protected with duct tape and ½" of high density foam prior to being place in the tri-axial test frame.

to record the incoming signals from the receivers. During the calibration phase, the system will round-robin activate each receiver as a source, one at a time, while

recording on the other channels. This not only checks the equipment if it is working, but also allows one to interrogate the rock media and determine the velocities for each ray path between all receivers. Table 3.7 shows the results of the auto calibration velocities between each pair of the eight receivers.

Table 3.7 – Stressed Block Auto Calibration Velocities (ft/s)

Receiver	1	2	3	4	5	6	7	8
1		9974	10108	11099	11070	12146	12901	14485
2	9266		10187	12220	12198	13841	14248	15088
3	10155	10218		9827	8941	10127	12448	13993
4	12142	12283	10016		9165	9872	12490	14173
5	11289	12227	8949	9113		8833	10217	13434
6	12176	13850	10156	9912	8773		8220	12825
7	13121	14226	12416	12494	10802	8225		7377
8	14514	15091	13986	14182	13429	12809	7364	

In both the calculation of the auto calibration velocities, as well as locating microseismic events within the block, an assumption is made that the time pick was made correctly and that the events were from a direct arrival waveform. Both of these assumptions can be in error. Having a high fidelity picking algorithm, hopefully based on a cross correlation of signals, helps to eliminate picking the wrong event. The Vallene system seems to do this function pretty well. However, the bane of seismic emission work in laboratory samples is the presence of non-direct-arrival energy. Each of the six free surfaces of the block specimen provides an excellent reflecting acoustic impedance contrast. It is not dissimilar to trying to find where one is standing in a house of mirrors.

So many reflections coming from so many different directions are bound to confuse reality. The Vallene microseism event location software (and to be fair, just about everyone else's too) assumes the energy is via direct arrival and positions the microseism accordingly. This is usually a reasonable assumption in field scale microseismic surveys due to the fact that there are no free boundaries so effective at reflecting energy back. But for laboratory experiments, this is a major source of errors.

3.4.2 Receiver Placement Strategy

Even when all recorded energy is a direct arrival, an ambiguity can develop if the signal from a source arrives at two different receivers at very nearly the same time. This is due to the fact that the location algorithm depends on the Time Difference of Arrival (TODA) in the travel times to two different receivers. This localization technique was first developed in World War I to locate artillery by using an array of acoustic receivers in a fixed position and noting the *difference* in the time arrivals. A requirement to find a uniquely located event in 3D is to have four receivers producing three unique time differences.

One of the ways to help mitigate the detrimental effects of near-simultaneous arrivals of acoustic energy at two different receivers is to calculate the travel times for a certain geometry and then position the receivers to prevent this from happening. Most commercial packages that perform this task use a ray tracing algorithm and can handle complex layer and receiver geometries as well as a complex velocity model. However, none were found that can handle the scale of a sample only 11 inches on a side.

As a result, an Excel spreadsheet is included in Appendix B where only a constant velocity in the desired layer (the Lyons Sandstone) was included. The expected fracture plane was gridded into 12,320 grid cells each 0.1 inches on a side. The travel times using the Lyons sandstone velocities were calculated from each grid cell (potential microseism source) to each live receiver on the block. The receivers were then moved to minimize the number of nearly-similar time differences between every possible pair of receivers for every grid cell.

This analysis is what drove the decision on where to place the receivers on the outside of each block in the experiments. A tolerance of one microsecond was used to declare a time difference too small to be able to differentiate and hence a source of ambiguity. The single plane fracture model contained 12,320 cells which produced 357,309 possible combinations of travel time differences. Twelve percent (41,805) of these travel time differences were found to be within the threshold of one microsecond of each other.

However, the TODA algorithm only needs four or five reliable channels with identified time picks (five is best according to Vallene), producing three or four time differences, to uniquely locate the source of the acoustic emission. All time differences picked beyond that number simply help the algorithm to converge on a solution and produce a quality factor assessment (the LUCY factor) of the localized event. Of all the cells in the model, with eight active receivers, there was not one cell where less than the minimum number of reliable time differences occurred. Hence, the location positioning of the receivers, even for the worst case fracture location, indicates that the receivers, if all functioned properly, could localize a microseismic event at any one of the cells in the

model. The resulting receiver locations for the two blocks are shown in Figure 3.9.

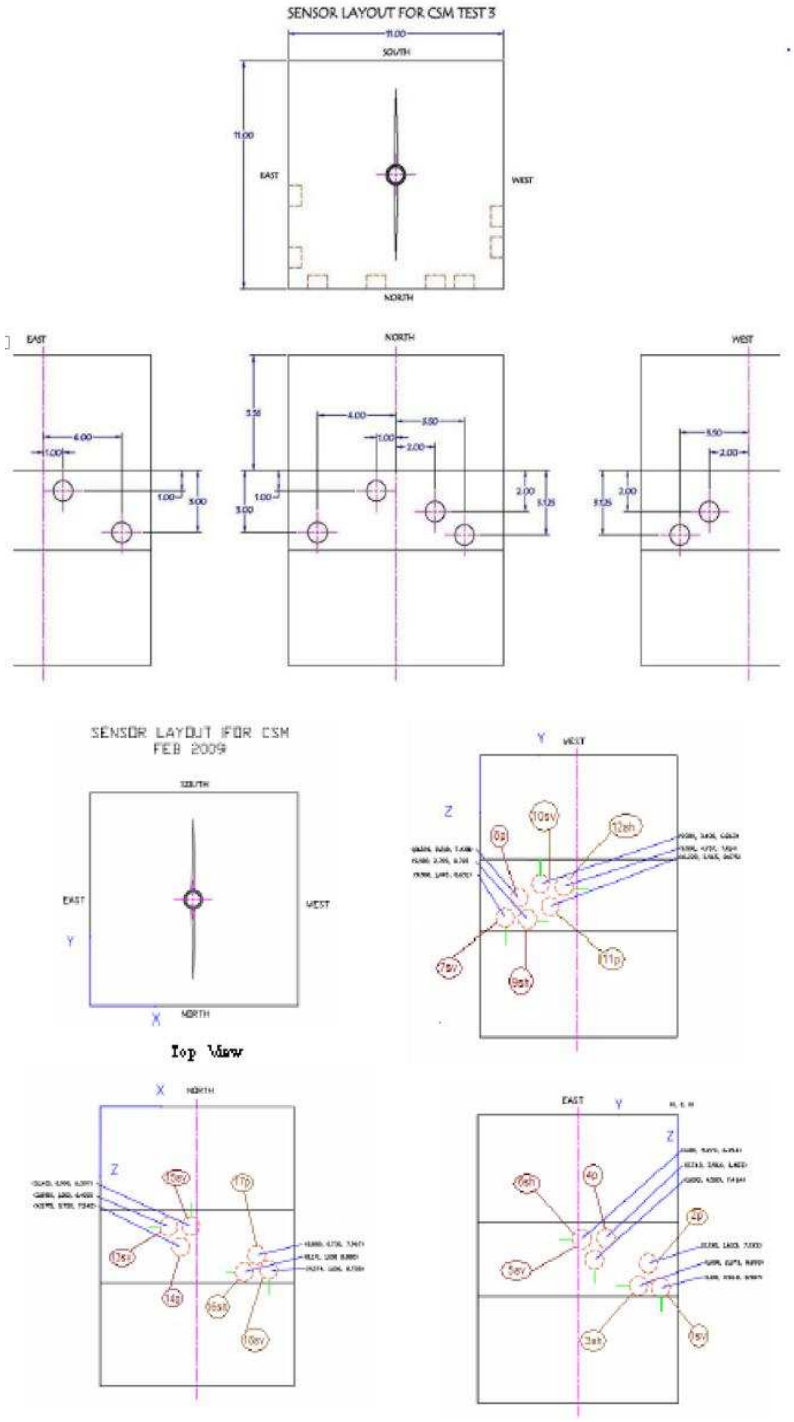

Figure 3.9 – Receiver placement for 8-sensor P-wave test. Brown circles indicate location of embedded receiver.

3.5 Laboratory Set-Up

The TerraTek laboratory located in Salt Lake City, Utah, is one of the world's premier drilling and completions testing facilities. In addition to all the supporting equipment and infrastructure, the basic lab set-up used in these two block tests consists of a tri-axial press, with pressure monitoring equipment on each of the three principle axes in the press, a high pressure pumping unit to send highly pressurized fluid down the wellbore of the specimen, and a recording system to keep track of the pressures and volumes. For the specific tests done as part of this research, the addition of the acoustic monitoring system was also included and explained in detail in the former section.

The small test frame was used because of the relative ease and lower cost for doing the tests. Essentially, specimen size is what determines which test frame to use. The maximum specimen size for the small load frame is 11" x 11" x 15" high. All samples were built slightly larger than this and then cut down with the large diamond saw at the lab to final dimensions. The small load frame has the capabilities shown in Table 3.8.

In essence, there are four welded metal bladders, called flatjacks, (Figure 3.10) that apply opposing forces on each of the four vertical sides of the specimen inside a very rugged steel frame. Each flat jack has its own intensifier capable of maintaining a constant stress upon the face of the block. Each pair of opposing sides can have a different stress applied to the face of the specimen to create a differential horizontal stress capable of mimicking in situ conditions of the subsurface. The surface area of the flat jacks does not completely cover the entire surface of the block so there is an

efficiency correction to the actual applied stress. For the small test frame this correction is 87% and is automatically backed out of the recorded pressures and stored ten times a second.

Table 3.8 – Terratek Small Test Frame Capabilites

Terratek's Small Block Polyaxial Stress Frame Maximum Capabilities	
Rock size (with pore pressure)	11" x 11" x 15" high
Rock size (without pore pressure)	10" x 10" x14" high
Central Borehole	1.5" diameter
Vertical Stress	4500 psi
Horizontal Stress 1	3000 psi
Horizontal Stress 2	3000 psi
Horizontal Stress Difference	2000 psi
Borehole Pressure	5000 psi
Pump Intensifier Volume	0.18 gal / 700 cc
Injection Rate	4 gpm / 1500 cc/min
Injection Pressure	2000 psi

The vertical (overburden) stress is applied through a different system with a vertical ram energized through an actuator and provides the highest external stresses. Any cables that run inside the test chamber must avoid being crushed by the vertical ram, or the flatjacks. When the cables must be run under the flat jacks, protective channels must be cut into the rock face to protect them (Figure 3.7). The sample is then lifted with a crane and gently lowered into the load frame (Figure 3.11). Teflon sheets are applied to the surface of the block to allow a low friction slip surface as the block moves when the horizontal stresses are applied to it. Once it gets centered in the frame,

no more movement should occur. The flat jacks are then inserted in the small space between the specimen and the load frame. Then wedge shims are inserted to take up the remaining space so that the flat jack does not have to expand to the point of rupture under pressure.

Figure 3.10 – High pressure flat jack shown on its side.

All cables are safely routed out of the vessel and the system is tested one last time to make sure everything is working (Figure 3.12). Then the vertical ram is placed against the top surface and the whole thing bolted in place. The borehole must then be connected to the high pressure fluid pumping system. The system must be purged of all air to minimize the compressibility of the borehole fluid. All connections must be tested

Figure 3.11 – Test block being lowered into the test frame.

for leaks prior to the vertical ram being put into place and the chamber sealed with the four large bolts used to constrain the vertical stress applied to the block. The actuator pushes the ram to make contact and apply the vertical stress to the block.

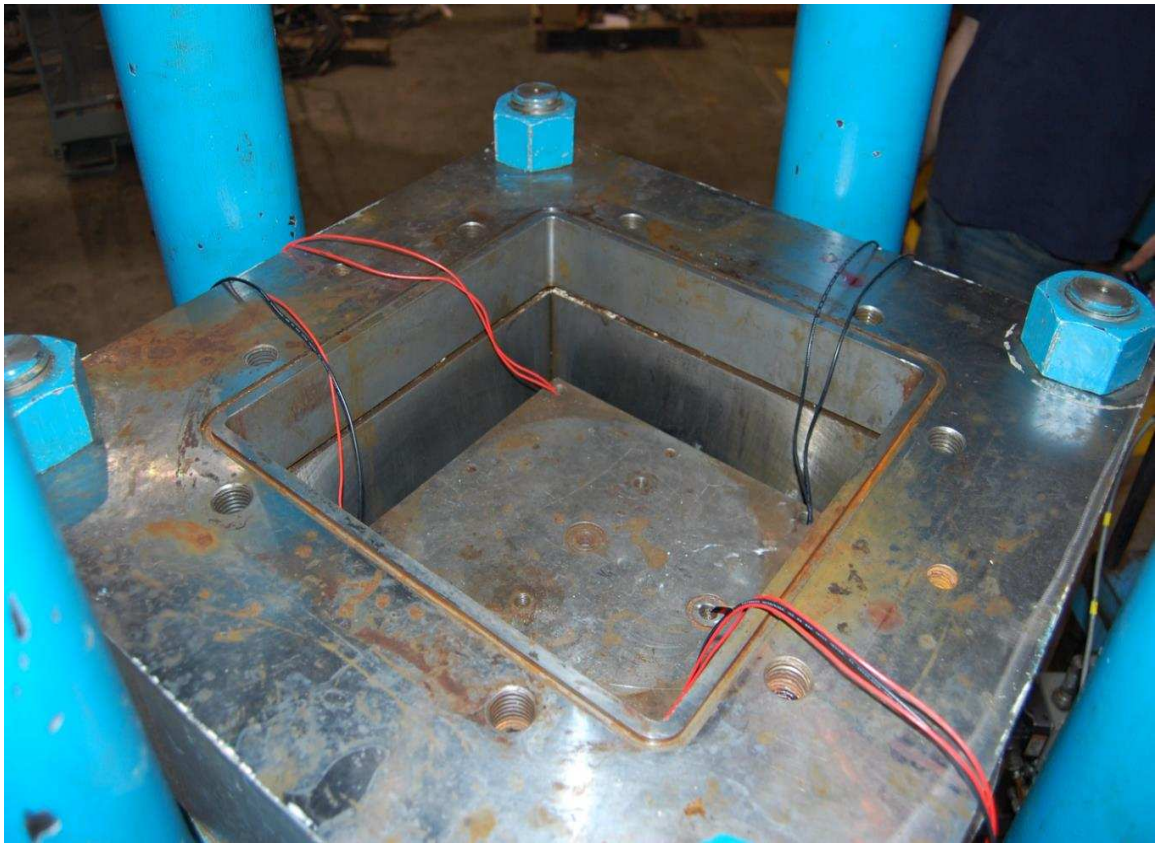

Figure 3.12 – Specimen in test frame ready for the vertical ram to be inserted and pressure applied. The wires running to the various acoustic sensors can be seen draped over the sides of the test frame.

CHAPTER 4

STRESS LOADING, PRESSURE, AND ACOUSTIC RESULTS

This chapter reviews the actual physical processes employed, and the results obtained therefrom, for the two layer sandstone block experiments conducted in August 2008 and February 2009. Details of how and why the blocks were carefully placed under the stress conditions they were, and the results of the fluid injection and associated acoustic monitoring results are presented.

4.1 Stress Loading

The purpose of laboratory testing is to be able to extrapolate the results to meaningful predictions at the field scale. It turns out that mimicking the in situ stress state of a petroleum reservoir is more difficult than one would initially think. With the exception of pore pressure, all in situ variables in this test were intended to parallel those expected in a real world environment. The difficulties in getting a dehydrated sample fully saturated, and verifying it as such, were beyond the scope of these tests. Working with dehydrated samples also simplifies some of the variables in the interpretation of the results.

Athavale (2007) produced, via the finite element stress modeling of his complex seven layer block, stress profiles in several directions. Due to edge effects on the block, he averaged the stress profiles for multiple slices taken vertically across the block width to produce the bold black profile you see in Figure 4.1. As can be seen, the layer with the lowest Poisson's ratio (the Lyons sandstone) translates the maximum (vertical) stress into a horizontal stress that augments those being applied by the stress frame. As can be seen, in Figure 4.1, the minimum modeled average value in the seven layer

block at the base of the Lyon's sandstone is about 900 psi. The maximum modeled average value occurs at the epoxy layer, which has a very high Poisson's ratio and gets up to about 2700 psi. Even for the difference between Lyons sandstone and 15.8 ppg cement, an increase in the minimum horizontal stress of about 300 psi is expected.

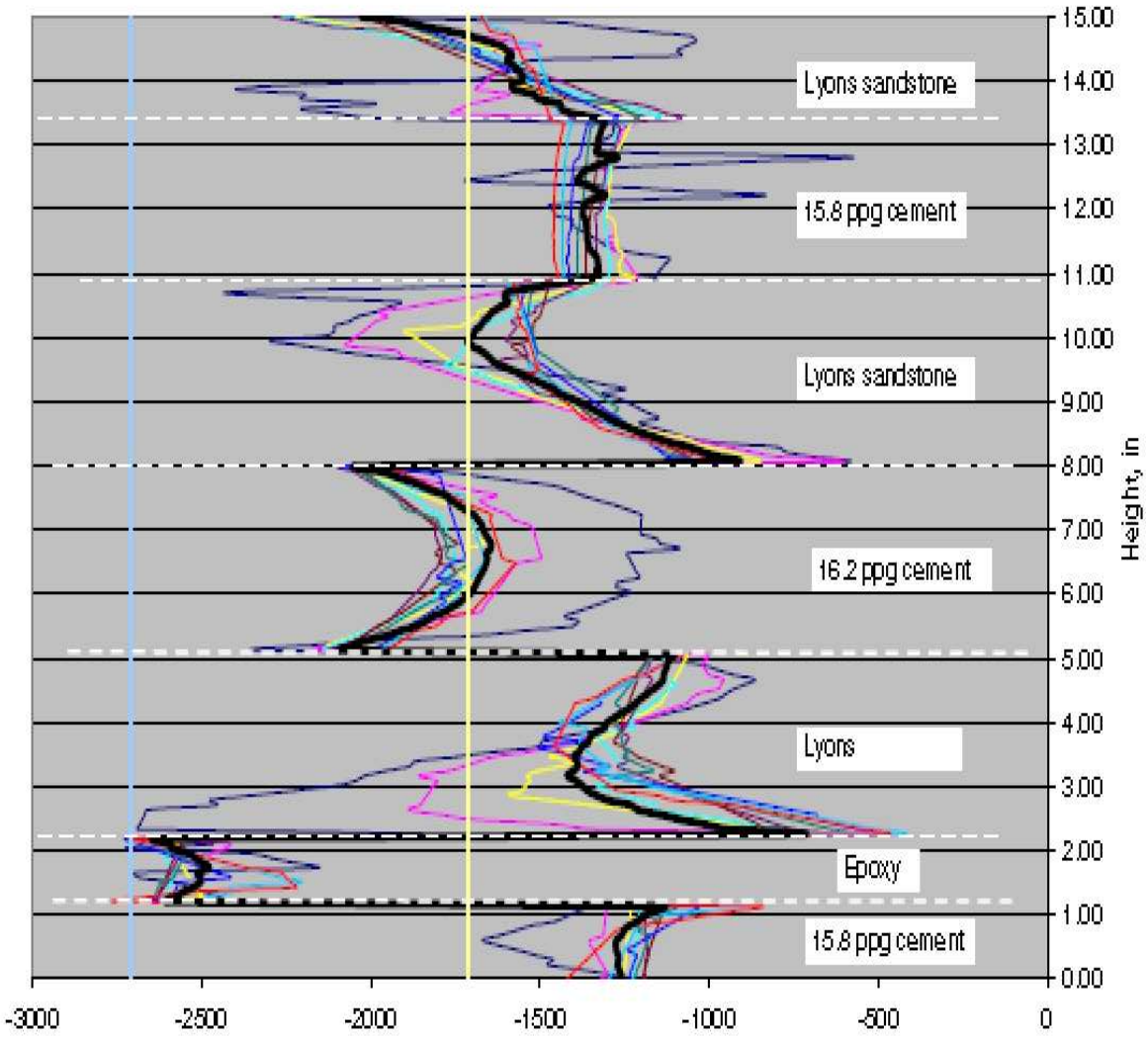

Figure 4.1 – Vertical profile for minimum horizontal stress plotted in cross section for the Athavale seven layer composite block. Each material boundary is represented by a dashed white line. The minimum horizontal stress is plotted in a series of different color curves and an average of all those curves as a bold black curve. Values vary by as much as 2500 psi at material boundary interfaces as annotated on the x-axis (From Athavale 2007).

During the stress modeling work, it became apparent that the sequence of stress loading in fact did matter. It is not uncommon for tri-axial stress work to first load the two horizontal directions of the block to allow it to most easily move to the neutral location in the tri-axial press, and then once centered, apply the overburden (vertical) stress. This however may not mimic the manner in which sediments were deposited, buried, and lithified in the real world. In Figure 4.2, one can see that applying a stress across brittle layers, thereby allowing the softer layers between them to 'feel' the stress, will produce a different result than applying a stress along the brittle layers, thereby shielding the softer layers from some of the applied stress burden.

As a result of this realization in Athavale's work, a stress loading path was developed that would most closely follow the expected path of real sediments at depth, versus one most experimentally convenient. In Table 4.1 the discreet steps used to pressure up the blocks to in situ conditions are listed. A few minutes of stabilization were allowed for at each stress step before increasing the stress in the next step. Note that steps no larger than 1000 psi in size were taken in any single step and that no over-stressing occurred (going beyond the final stress and then relaxing back to the final value). Interestingly, at each of these stress changes (even as small as 200 psi), a tremendous surge of microseismic activity would occur. This result was not expected and is discussed in Chapter 5.

With the block now loaded to the final stress state in a manner similar to what happens in the real world, several finite element stress models were built for the three

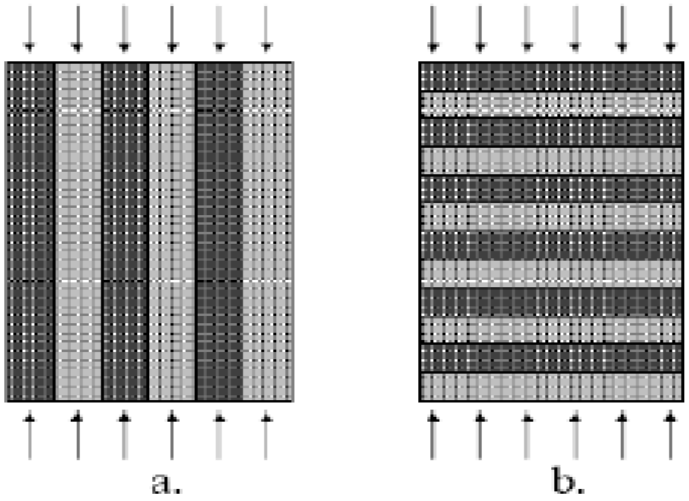

Figure 4.2 – a) stress along layers vs. b) stress across layers. The alternating colors of each layer of black and grey are meant to have different rock moduli properties. Depending on how the stress arrows are applied, a different resulting 'effective moduli' is calculated. This can be seen where in sample a), the stiffer layers will take more of the applied load than they can in sample b). Due to the orientation of the contrasting stiffness layers, the overall sample will exhibit different stiffness characteristics with the same stress applied in one orientation relative to the other (from Athavale 2007).

Table 4.1 – Stress Loading Sequence

Overburden Stress (psi)	**Maximum Horizontal Stress (psi)**	**Minimum Horizontal Stress (psi)**
0	0	0
200	**200**	**200**
2000	200	200
2000	1000	1000
3000	1000	1000
3000	1400	1400
3000	2000	1400
4000	2000	1400
4000	2400	1400
4200	2400	1400

layer block used in this test (Alqahtani 2010). First a solid block (no well bore) was modeled to see the effects of the differential stress applied to the block shown in Figure 4.3. The colors represent the modeled shear stress with a maximum concentration of about 600 psi (opposite colors of different directions at the top and bottom of the layer). This shear stress is created simply by the translation of the maximum (overburden) stress into horizontal stress through Poisson's ratio. Up to 600 psi of additional stress in the horizontal direction due to overburden should be expected, and it will be localized along the material property boundary between the cement and the Lyons sandstone.

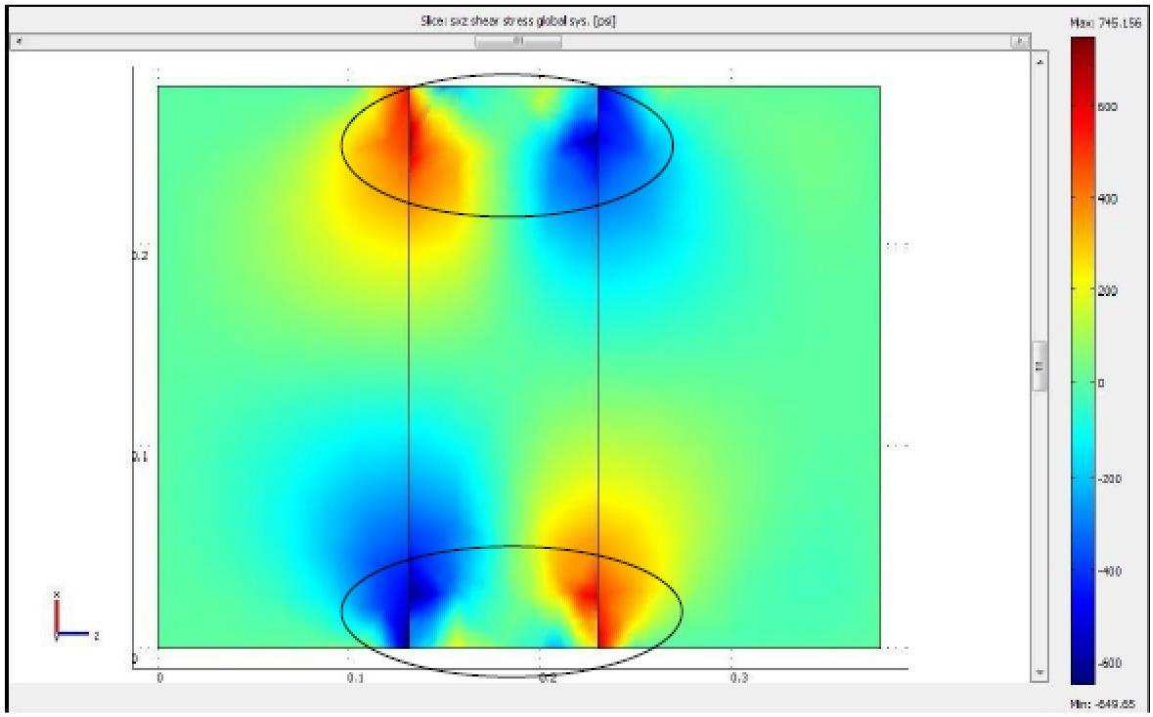

Figure 4.3 – Tri-axially stressed three layer block model laying on its side showing shear stress along material boundaries. Induced shear stresses of about +/-620 psi (from Alqahtani 2010).

Once the numerical model results were validated with analytic solutions, Alqahani (2010) then inserted the wellbore to investigate the effects of a cemented

(epoxy in this case) wellbore bonded to the rock face along its length. The problem with this aspect of an experiment is that it cannot as yet replicate field situations. In the lab, a hole must drilled in the unstressed rock, the casing inserted, and allowed to cure. Then the entire ensemble is placed in the tri-axial press and stress is applied. This process does not mimic what happens in the real world.

In the real world, a hole is drilled into the *already stressed* rock sequence, and the steel casing cemented. Additionally, in proportion to the rest of the model scale, the thickness of the steel casing in the laboratory is much more, when scaled to the field dimensions, than is appropriate. In other words, the amount of steel used in the 11 inch sample is about 150,000 times more than what is used in a 10,000 ft reservoir model with 23 pound, P-110, 5.5" casing. Likewise, the epoxy has a far higher Poisson's ratio than would normal cement used in the field. These two distortions would partially cancel each other out but one should approach the distortions to the stress field due to the casing cemented in the pre-stressed model, as a minimal factor for real world expectations. Figure 4.4 shows two very interesting phenomena: 1) there are the shear stresses across the material property interface as in Figure 4.3 (notice different color scale being used), and 2) there is a large stress concentration at the two right angle corners of the borehole. There is up to 2000 psi of shear stress generated by removing the material at the base of the borehole.

This surprising stress concentration was experimentally verified with the first two cement-only test blocks that were used. It each case the fracture induced at the borehole would initiate horizontally and then begin to rotate to a vertical plane away

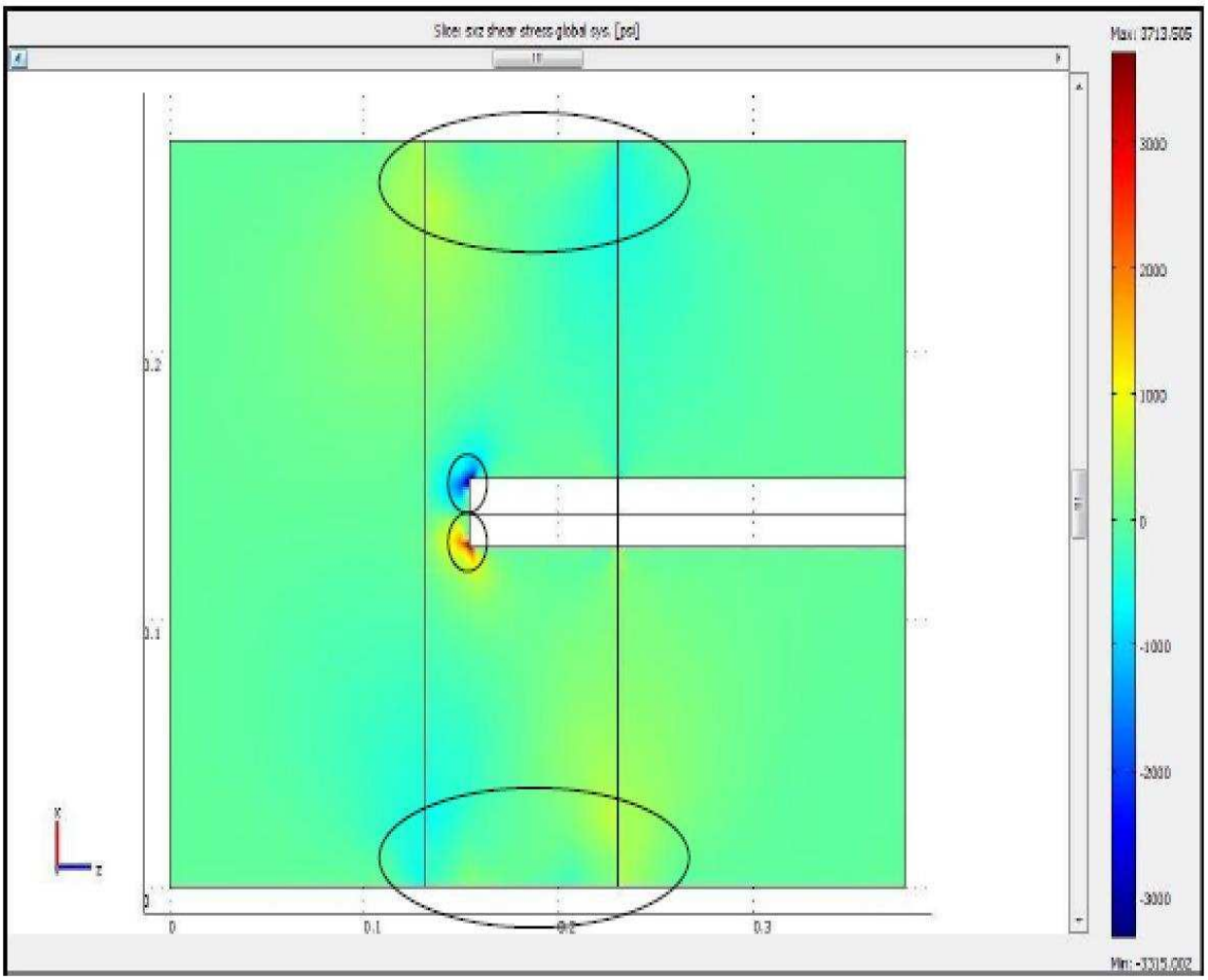

Figure 4.4 – Modeled horizontal stress concentration at the sharp edged base of the borehole shows concentrations over 3300 psi. Borehole is landed in the sandstone section of the three layer model laying on its side (from Alqahtani, 2010).

from the well bore. Even when the overburden stress was much higher than the minimum horizontal stress, the fracture initiated horizontally due to the geometrically induced shear stresses at the base of the well bore. This problem was remedied by placing an epoxy plug at the base of the borehole that formed a slight meniscus and effectively distributed the previous point stress loading at the base of the borehole (see Figure 4.5).

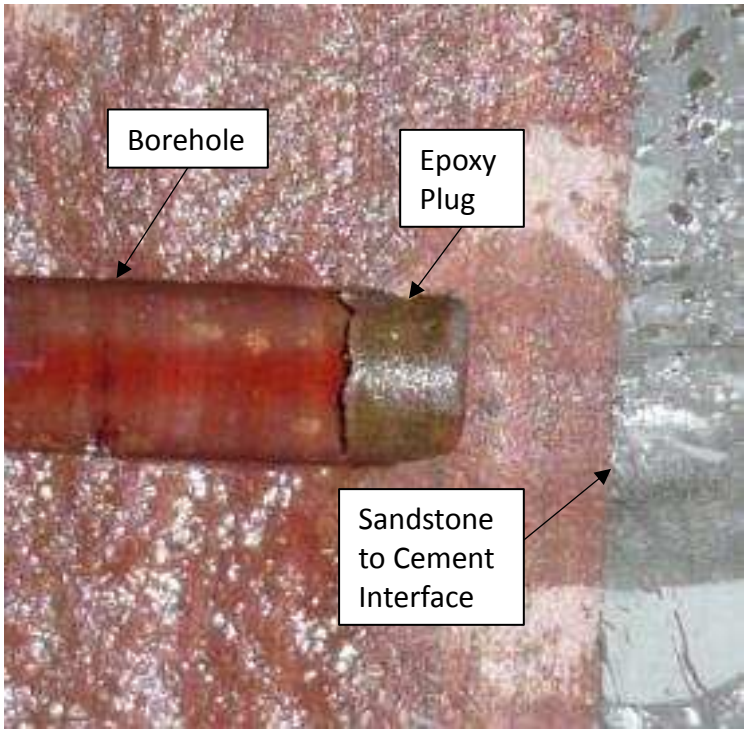

Figure 4.5 – Empirical borehole epoxy plug to distribute horizontal stress concentration at base of borehole and prevent horizontal fracture initiation.

4.2 Block 1 Injection Tests

The Vallene AMSY-5 acoustic emission system was connected to all receivers mounted into the face of the block and the system went through its calibration test to both verify that each receiver was recording a signal and also to measure the velocity between each pair of receivers (Figure 4.6). Notice the amplitudes (in dB) and the velocities (in cm/ms) have some variance and also have some receivers not coupled well enough to gather a reading under unstressed conditions. Once the block was placed in the tri-axial press, the coupling of the receivers to the rock face was much better with each receiver meeting the criteria.

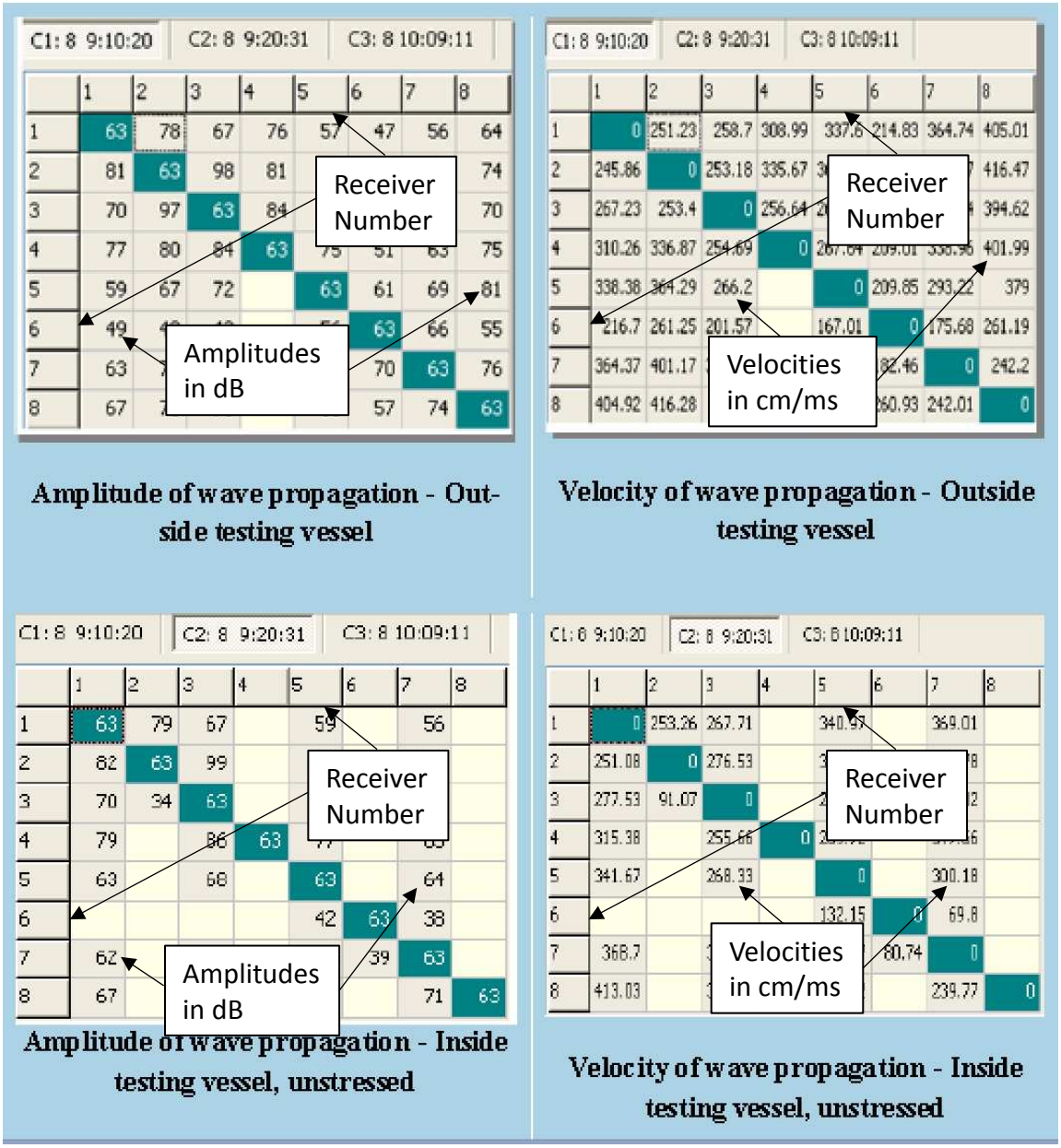

Figure 4.6 – The top row of tables shows the amplitude coupling and the detected velocity of the medium between each pair of receiver labeled both vertically and horizontally in the unstressed state with the sample outside the test frame. The same pair of comparisons is made on the bottom row of tables with the exception that the sample is now under stress in the test frame. Notice that some receivers are not responding (4, 6, and 8), probably due to poor isolation from the flat jacks.

Once the system passed this unstressed test, the block was lowered into the test frame, the hydraulic lines connected and purged of air, flat jacks placed at each side of

the block and shimmed into place, and the top hydraulic ram bolted into the test frame. The pressure loading sequence was initiated, and the acoustic monitoring system was left on to pick up any signals. The AMSY-5 has a feature where it will produce an audible pop through its speakers when an acoustic 'hit' is detected with an amplitude above the trigger which is set by the operator. When the first set of pressures was applied to the block in the press, most of the activity was translating the block laterally to its neutral center position. Experience has found that 200 psi is sufficient to move the block to this position and from that point onward, it is simply taking the stress applied from all five sides (the bottom is stationary).

Interestingly, each pressure step that the block underwent as per the schedule in Table 4.1 produced a plethora of acoustic emission events triggering the system. It literally sounded like a popcorn maker. The intensity of the events was strongest in the beginning but appeared to taper off exponentially over a time period of a few minutes. This apparent log-normal distribution of acoustic emissions was not previously expected. Its meaning is discussed in Chapter 5.

Once the block reached its final stress state of 4200 psi vertical, 2400 psi maximum horizontal, and 1400 minimum horizontal, it was allowed to stabilize for several minutes while preparing the system to begin injecting fluid into the well bore. At this point the final acoustic calibration test was done, just as before but now on the block under stress conditions. The results in Figure 4.7 show that all receivers were well coupled, and if anything, the velocities have slightly increased. For reference, taking an average of the highest velocities from reliable time picks yields a velocity of about 450 cm/ms which translates to about 14,763 ft/s. The independent lab tests for the

compressional wave velocities from Table 3.2 were 14,219 ft/s; or only a 3.7% difference. Well within any experimental error expected.

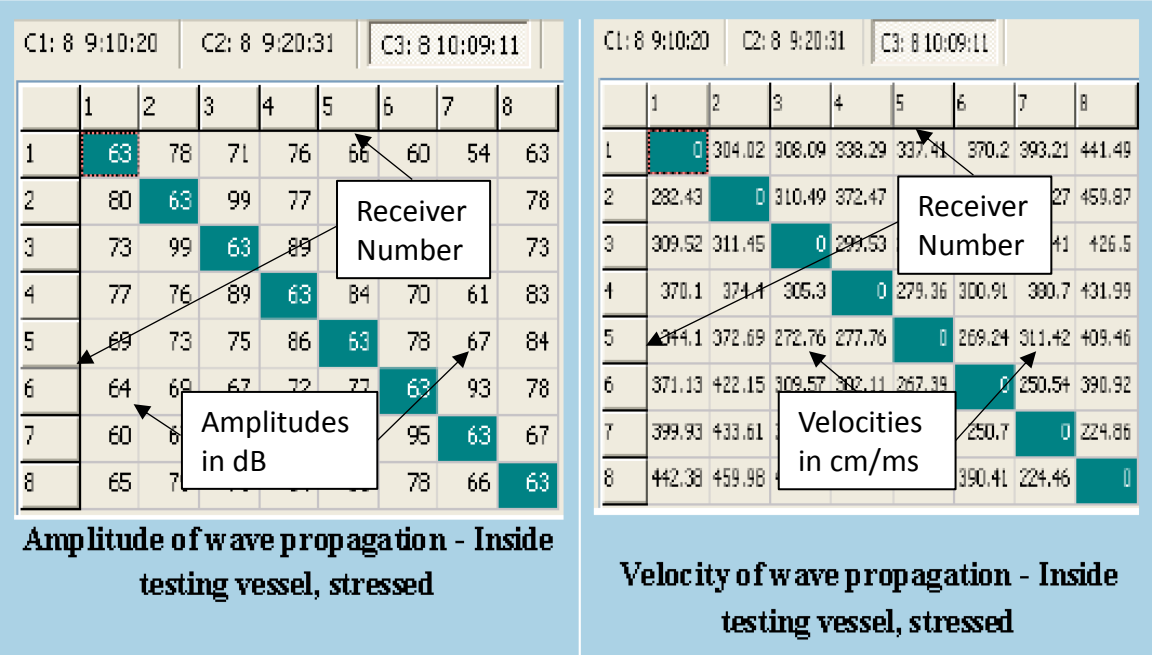

Figure 4.7 – Table of receiver coupling and auto-calibration velocities between each pair of receivers under stressed conditions within the test frame. Notice that coupling improves and velocities stabilize under stressed conditions.

Pumping was designed to proceed at 10 ml/min. The fluid was a silicon based 1000 cp fluid that does not harm the pumping equipment, has relatively easy clean up, and virtually no ability to leak off into the formation. In Figure 4.8 one can see five traces versus time on the horizontal axis. The three top curves (purple, red and light blue) reflect the pressures applied to the surface of the block in the tri-axial press. These pressures step up through the loading sequence in Table 4.1 and stabilize at the final experimental stress state of 4200 psi vertical, 2400 psi maximum horizontal, and 1400 psi minimum horizontal, at about minute 56 of the test.

The two bottom curves, brown and blue, reflect the injected volume, and the injection pressure respectively. The maximum pressure, of 4068.8 psi was reached at 85 minutes and 41.8 seconds of the test. The cumulative injected volume was 191.4 ml of fluid.

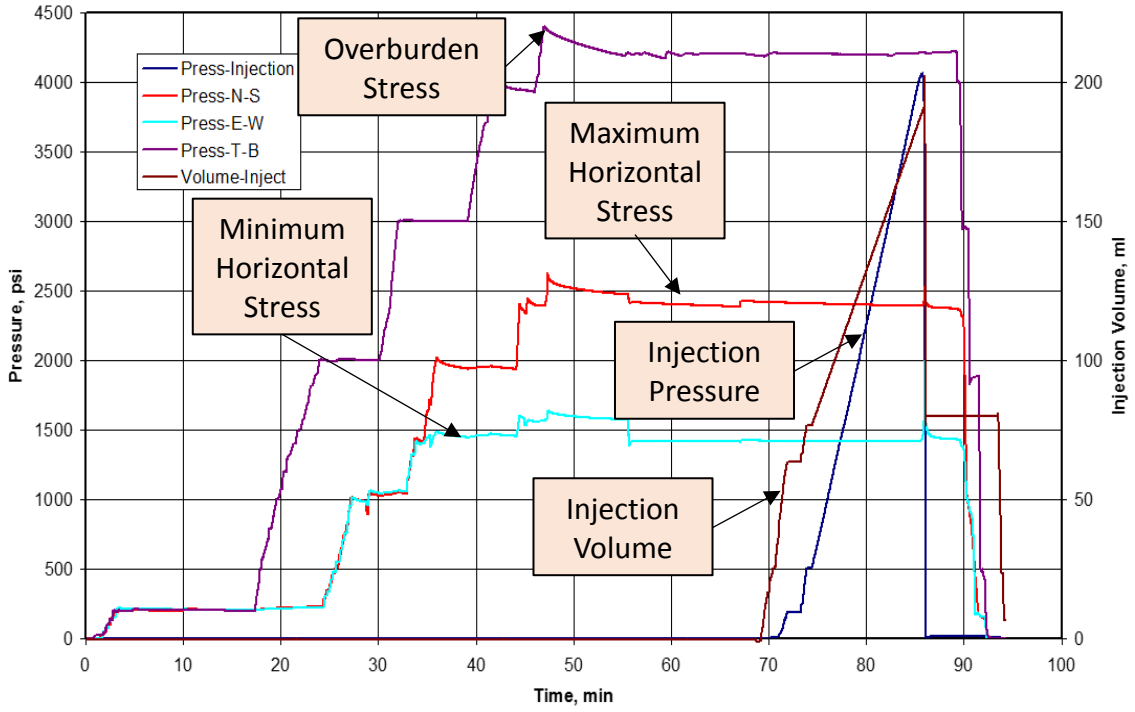

Figure 4.8 – Block 1 treatment pressures, tri-axial stresses and cumulative injection volume. Pressures and stress on the left y-axis in psi. Injection volume in ml on the right y-axis. Treatment time in minutes along the x-axis.

As soon as significant pressure was seen on the minimum stress pair of flat jacks, the pumping was stopped and a manual pressure decay started. This process was not automated and so there was variance test to test. Detecting the fracture initiation was done by closely monitoring the detected pressure on the minimum horizontal stress flat jacks; in this case the light blue pressure curve. The interpreted fracture initiation for this test occurred at 85 minutes and 15 seconds into the test with a

flat jack pressure on the minimum stress flat jacks of 1418 psi and an injected volume of 184.55 ml of liquid. The end of the fracture was interpreted to be at 86 minutes at a minimum stress flat jack pressure of 2564 psi and an injected volume of 191.4 ml of fluid. In summary, the fracture grew for 45 seconds and took a fluid volume of 6.85 ml.

The microseismic activity shows a dramatic jump at the same time the fracture initiation occurs. In Figure 4.9, it can be seen that the number of detected microseismic events goes up dramatically although the size of the events (the detected RMS amplitudes) is largest when the fracture is more developed. At the maximum pressure sensed on the flat jacks oriented perpendicular to the advancing fracture, the fracture was dilated to its maximal extent and reached the edge of the block where the fracture fluid was allowed to escape and thereby cause the sudden drop in pressure sensed on the flat jacks. This is also a time when there is a relatively quiet acoustic period with a drop in the microseismic activity. In essence, the stress is no longer building and causing all the acoustic emissions. But, as the stress continues to fall, in effect there was a relaxation of the high stress put on the material, a reversal begins and another high amount of seismic emission is seen with the stress relaxation mirroring the stress build up earlier.

This first block had eight receivers strategically located on the block faces in the Lyons sandstone unit to optimize direct arrival energy and minimize duplicate ray path ambiguity. However, laboratory conditions are among the most difficult due to all the other modes of energy that are picked up by the receivers. Each free surface provides an excellent acoustic impedance contrast to reflect energy back into the block. This is similar to the free surface ‘multiple’ problem experienced in conventional seismic

reflection recording. However, there are far fewer receivers, less regular data, and six times as many free surfaces to produce reflections.

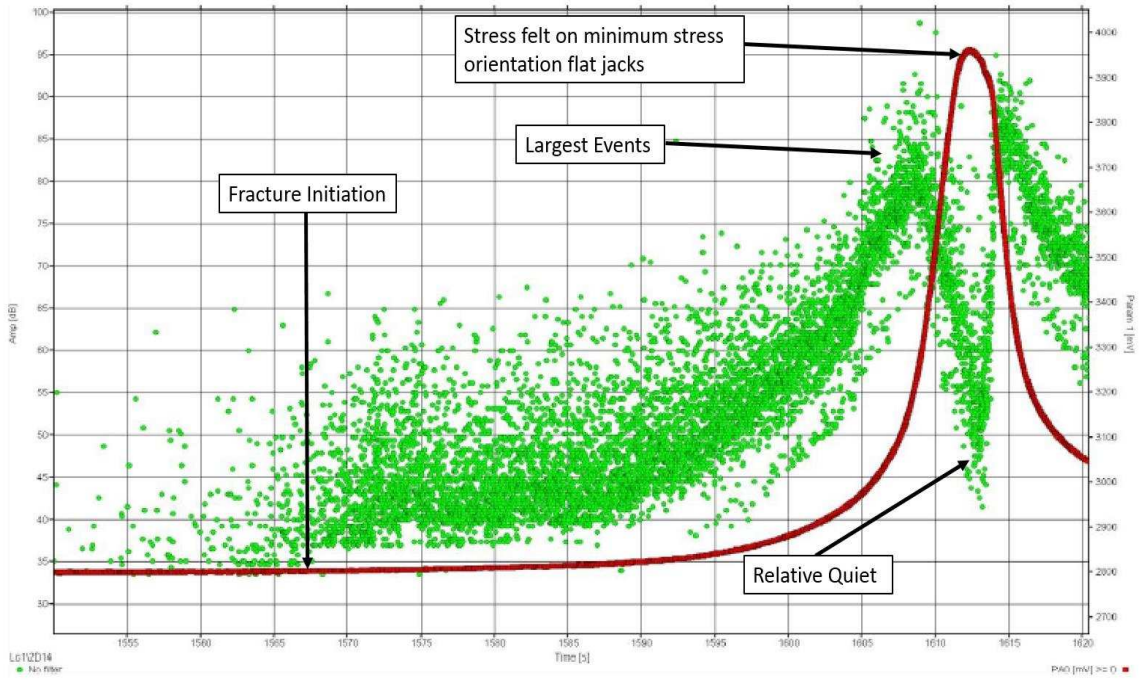

Figure 4.9 – Block 1 acoustic emissions (in green) and minimum horizontal stress flat jack sensed pressure (in red). Green event microseisms occur at the time of treatment indicated on the x-axis in terms of seconds from injection start time and with relative amplitudes in dB as indicated on the left y-axis. The pressure sensed on the minimum stress flat jacks is the one to show fracture dilation strain which causes the jump in the measured pressures. Unfortunately, the left y-axis scale is not scaled to psi so this is only a relative pressure measurement in this graph.

The Vallene AMSY-5 has internal software to do several things. First is an event triggering function where the incoming amplitude levels are constantly monitored and when an amplitude exceeds the preset level an event occurs. This causes the next function of the software whose job it is to capture the information around this event. The software will then write a certain number of time sample amplitudes prior to the event

(the leading portion) and a certain number of samples after the event (the lagging portion) to disk storage. The window length used in this test was 2048 samples at a sampling rate of 2.5 Mhz. So each window contains about one millisecond of waveform data from which the software selects the peak arrival time of an incoming event.

It attempts to do this for all eight receivers in this time window; but, for a host of reasons, not all eight receivers may have amplitudes sufficiently large to get a reliable time pick from them. The localization technique only requires four valid time picks to localize an event, although five is strongly recommended. The more time picks the software has, the more accurately it can position the spatial location of the seismic source in 3D. An estimate of the uncertainty in that position is reflected in a number is called the LUCY number. This is an estimate in mm of the radius of uncertainty in the localized microseism. A lower number is a more reliable pick. This quality measure is used to discard some of the less reliable picks from the dataset for display.

For the entire duration of the experiment, the total number of events detected that produced a solution (having at least four time picks within the window) for a common source was 17,754 (Figure 4.10) however the Vallene software has a requirement of having at least 5 valid time picks which reduces the number of localized events down to 12,915. Further refining the solution with the requirement that the localized event had to occur within the confines of the block, thereby eliminating many of the multiples) reduces the number of constrained localized events to 7950, and of those fewer and fewer met the constraints of tighter LUCY numbers. A LUCY number of 1.0 inch was selected as the best trade-off between numbers of events and precision of localization. 893 Events met the constraint of having a LUCY uncertainty number of less

than 1.0. This is about the number of microseismic events one would detect for an entire well bore in practice, although that would be for several stages of stimulation.

The aerial view of the block (looking down) with all the events posted having LUCY values less than 1.0 is shown in Figure 4.11 The cross section view is shown in Figure 4.12, and the end-on view is shown in Figure 4.13.

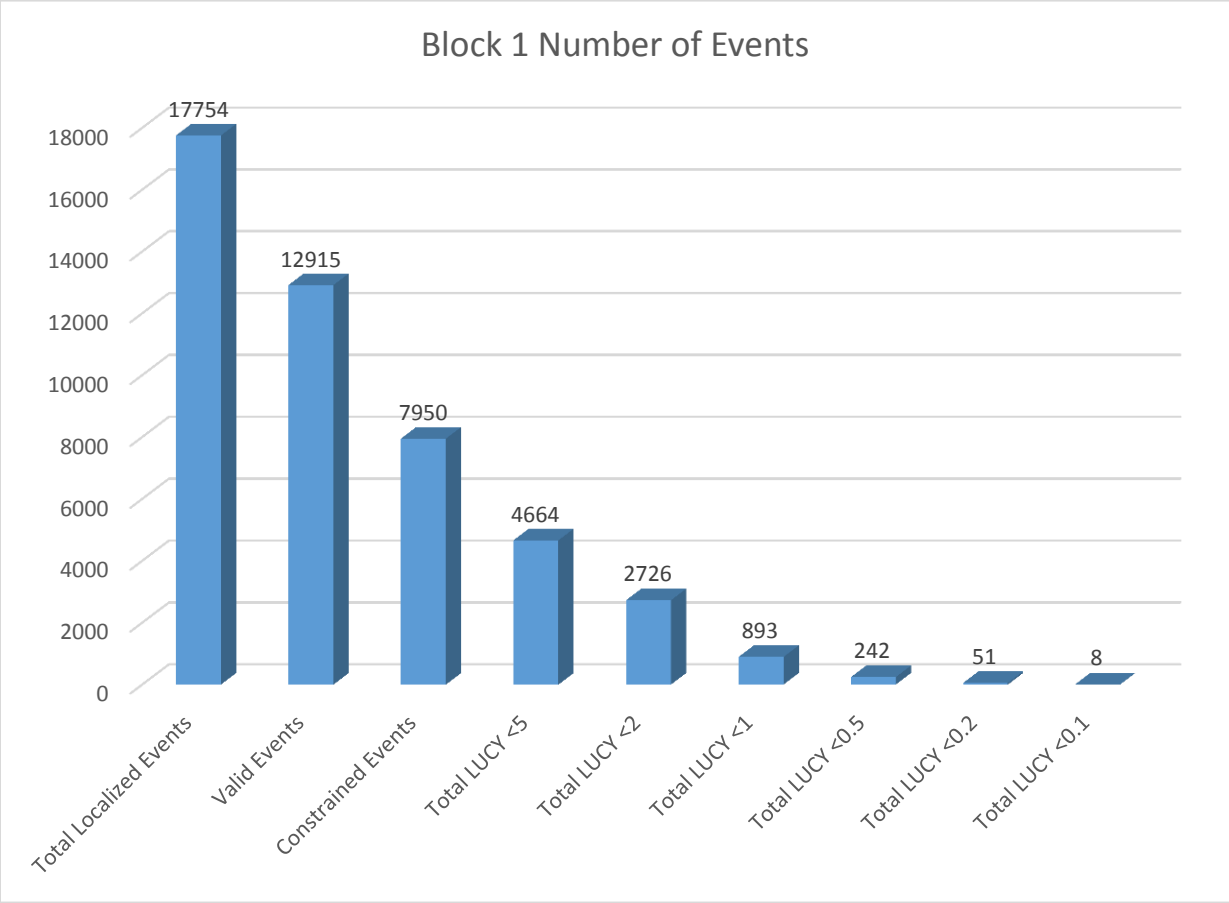

Figure 4.10 – Block 1 total numbers of localized events versus the LUCY (location uncertainty) number in inches.

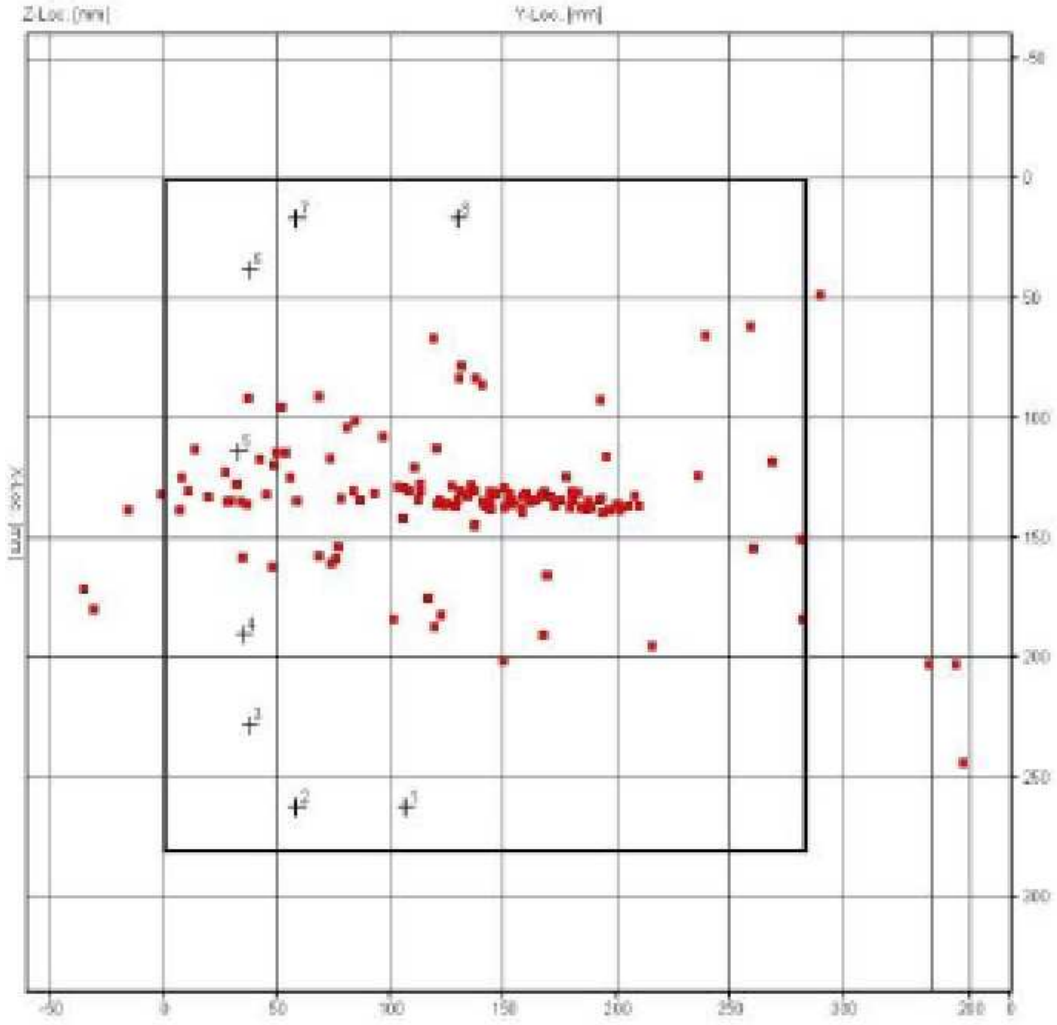

Figure 4.11 – Block 1 aerial view of localized events looking down onto the top of the block outlined in the bold black outline. You can see how the red localized microseisms align very well from the center of the block and emanate in a roughly linear manner in the direction of maximum horizontal stress (right to left).

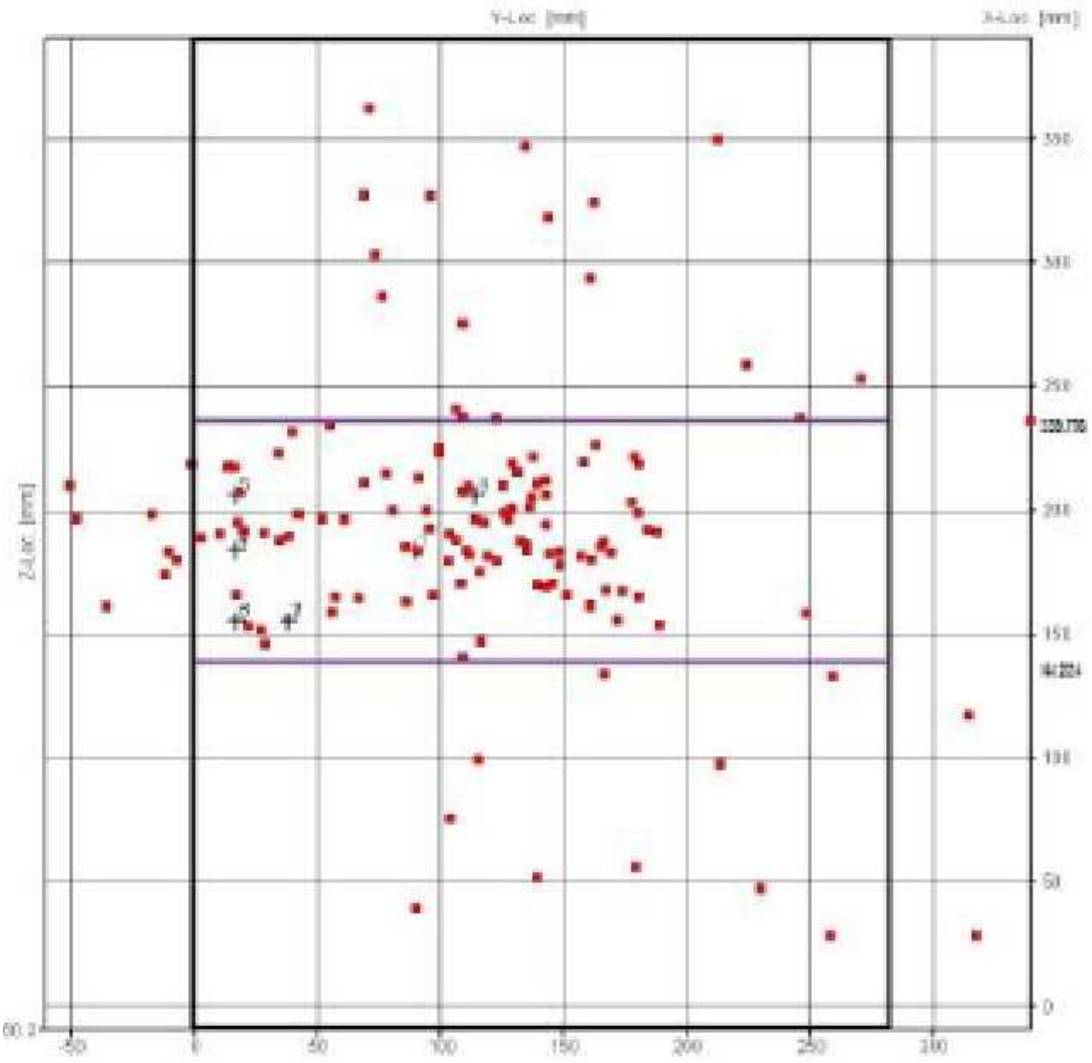

Figure 4.12 – Block 1 cross section view of localized events looking at the side of the block. The purple lines delineate the top and bottom of the sandstone layer in which the fracture was initiated. You can see how the red localized microseisms are largely concentrated in the sandstone layer.

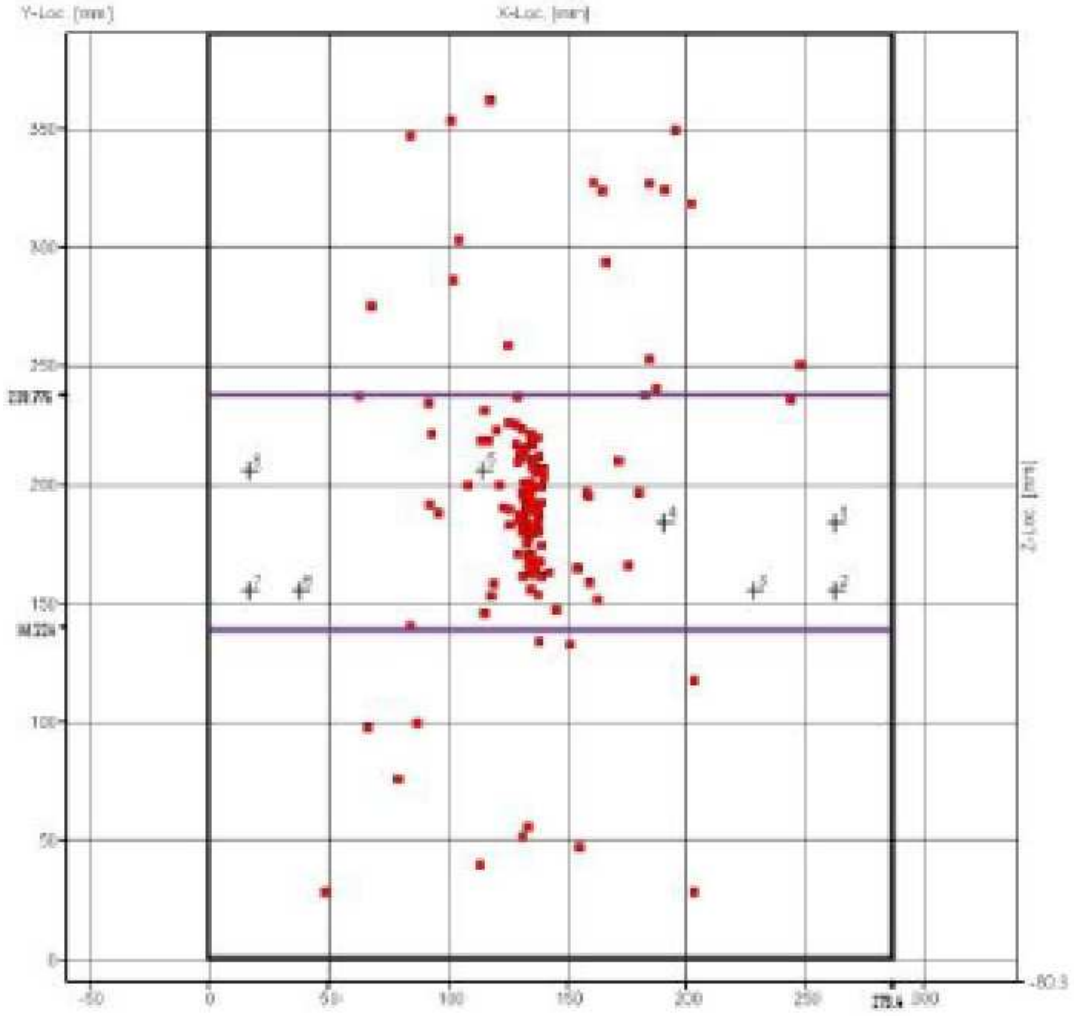

Figure 4.13 – Block 1 end-on view of localized events looking down the fracture along maximum horizontal stress. You can see how the red localized microseisms are almost completely trapped within the sandstone layer and produce a largely vertical fracture plane aligned with the wellbore in the center of the block. The two purple lines delineate the top and bottom of the sandstone layer.

4.3 Block 2 Injection Tests

For the second block test, the channel count for the Vallene AMSY-5 acoustic emission system was increased to accommodate 18 channels of recording. This allowed for six tri-axial locations on the outside of the block, each with a compressional wave receiver (the SE150-M) and two orthogonal shear wave receivers (the SH225-M).

The system was connected to all 18 receivers and bench tested before being placed into the tri-axial press. Once in the press, it was also run through an auto-calibration pass before any stresses were applied to the block faces. Both on the bench and unstressed in the press, a few receivers can be seen to not be responding due to poor coupling to the rock face (blank white boxes in Table 4.4). Notice the amplitudes (in dB) and the velocities (in in/ms) have much more variance than in the former test. This is attributed to the fact that the P-wave receivers (and transmitters) generate fast traveling waves that are picked up by the other P-wave receivers but also the shear wave receivers; especially when mounted on a face of the block orthogonal to the transmitter. In other words, the P-wave transmitters will have their signals received by most of the other receivers as P-waves. However, the shear wave transmitters are trying to generate shear waves that are not easily detected by either the P-wave receivers, or the shear wave receivers orthogonal to the particle motion generated.

Just as in the test for block 1 summarized earlier, for block 2 the acoustic monitoring system was bench tested (Table 4.4), again tested unstressed (Table 4.5). In addition to the coupling tests, the acoustic system was also tested on the bench and unstressed for the velocity between each pair of receivers (Tables 4.6 and 4.7). Then block 2 was placed in the test frame, brought under full experiment design stresses and again tested for the receiver coupling (Table 4.8) and the velocities between each pair of receivers under stress (Table 4.9).

Table 4.4 – Block 2 Amplitude Coupling Tests Bench

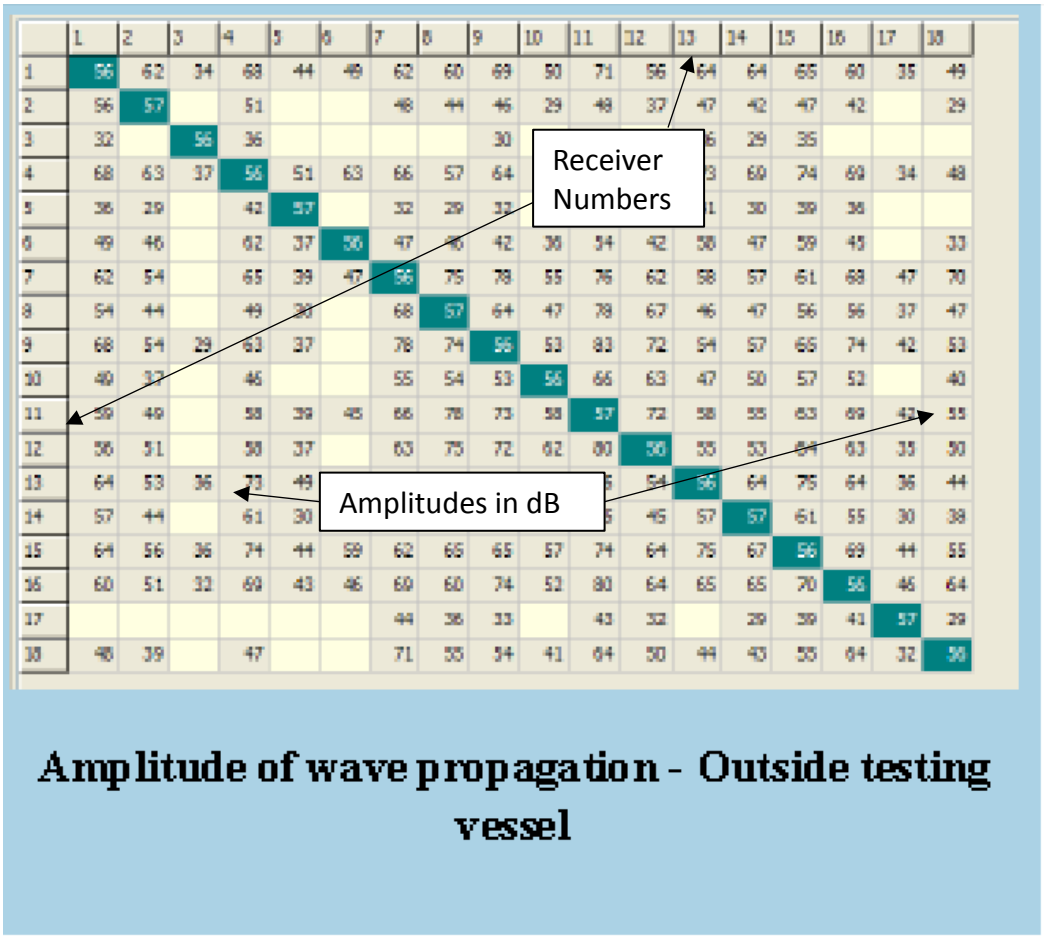

Table 4.5 – Block 2 Amplitude Coupling Tests Unstressed

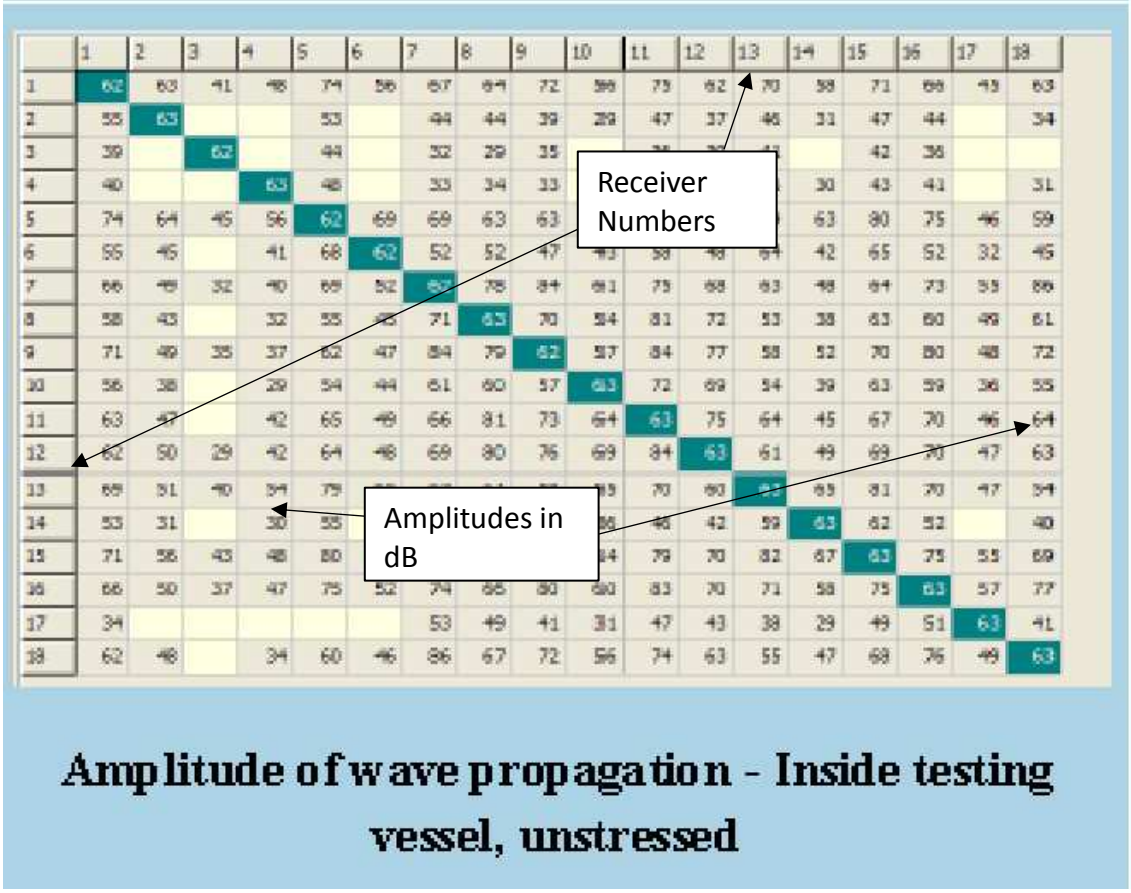

Table 4.6 – Block 2 Auto-calibration Velocities Tests Bench

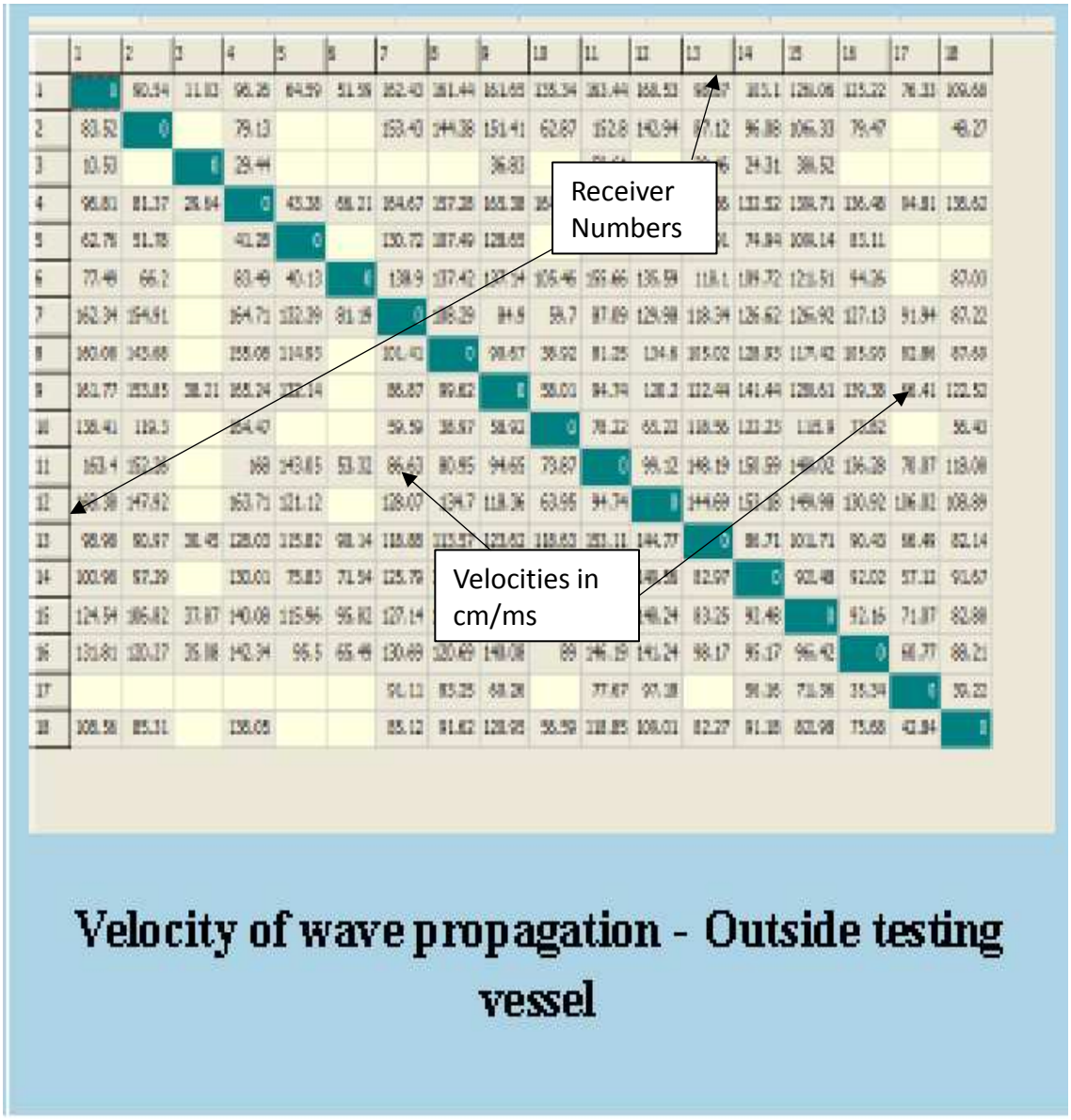

Table 4.7 – Block 2 Autocalibration Velocities Tests Unstressed

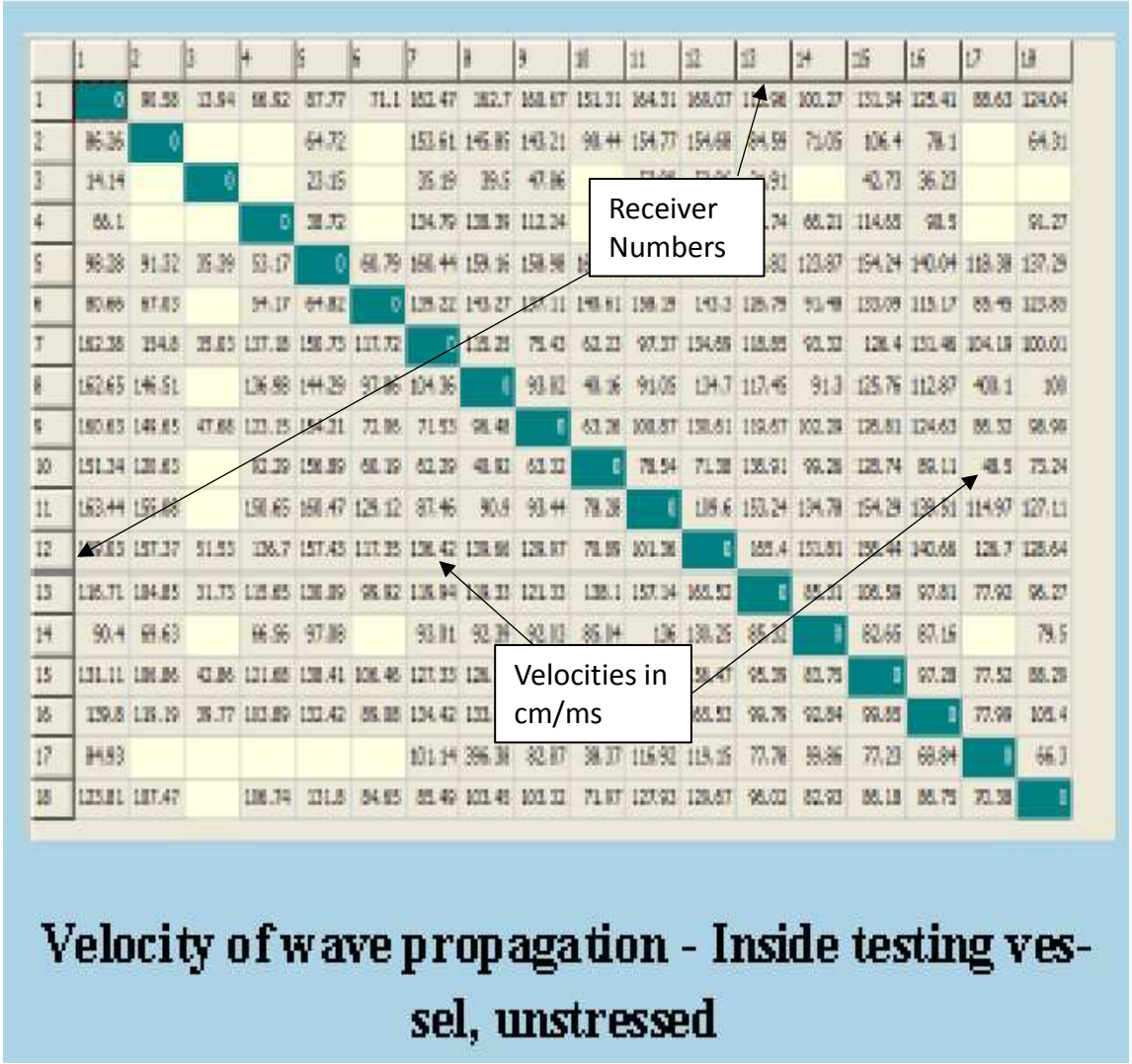

Table 4.8 – Block 2 Amplitude Coupling Results – Stressed

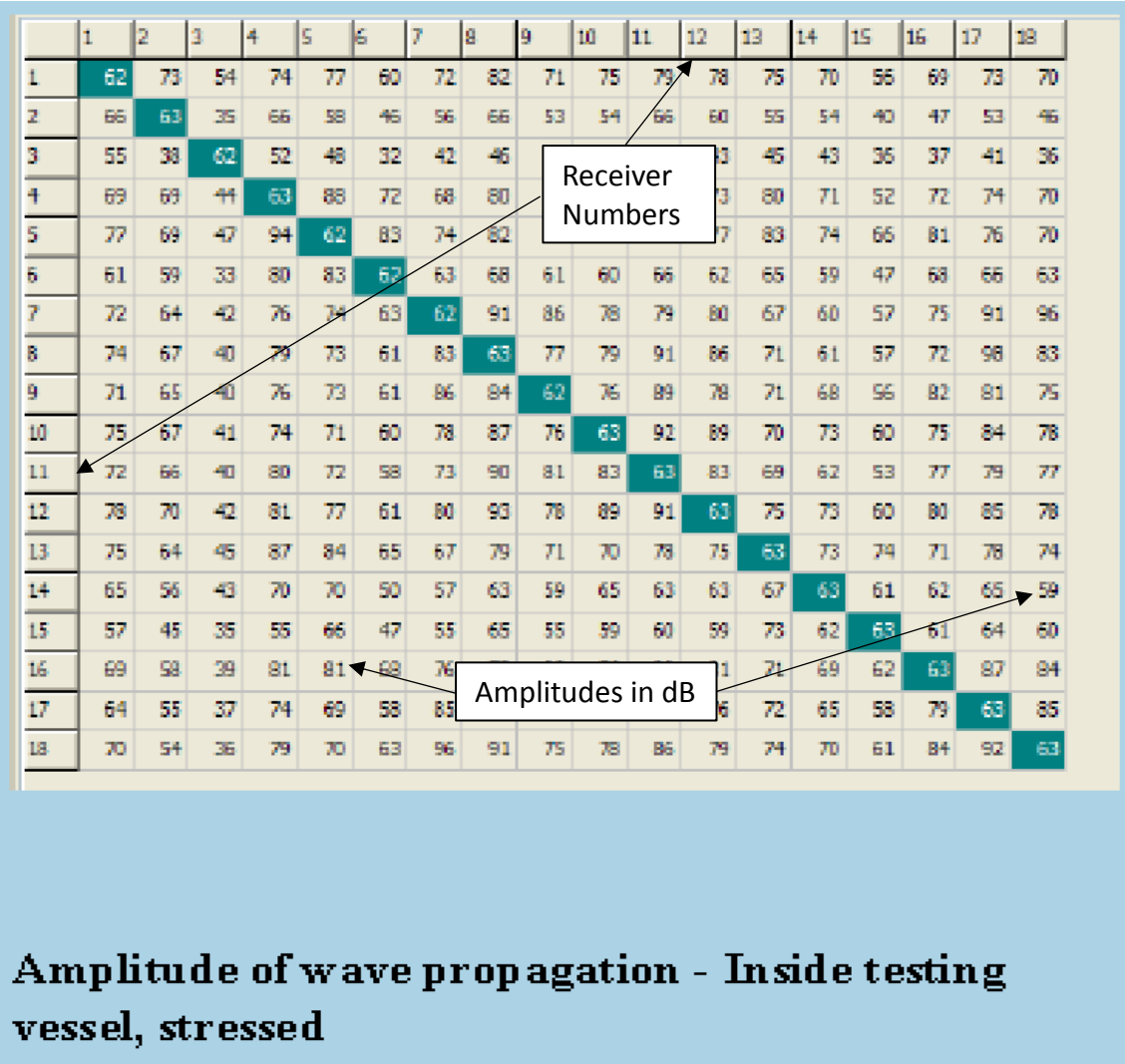

Table 4.9 – Block 2 Auto-calibration Velocity Results – Stressed

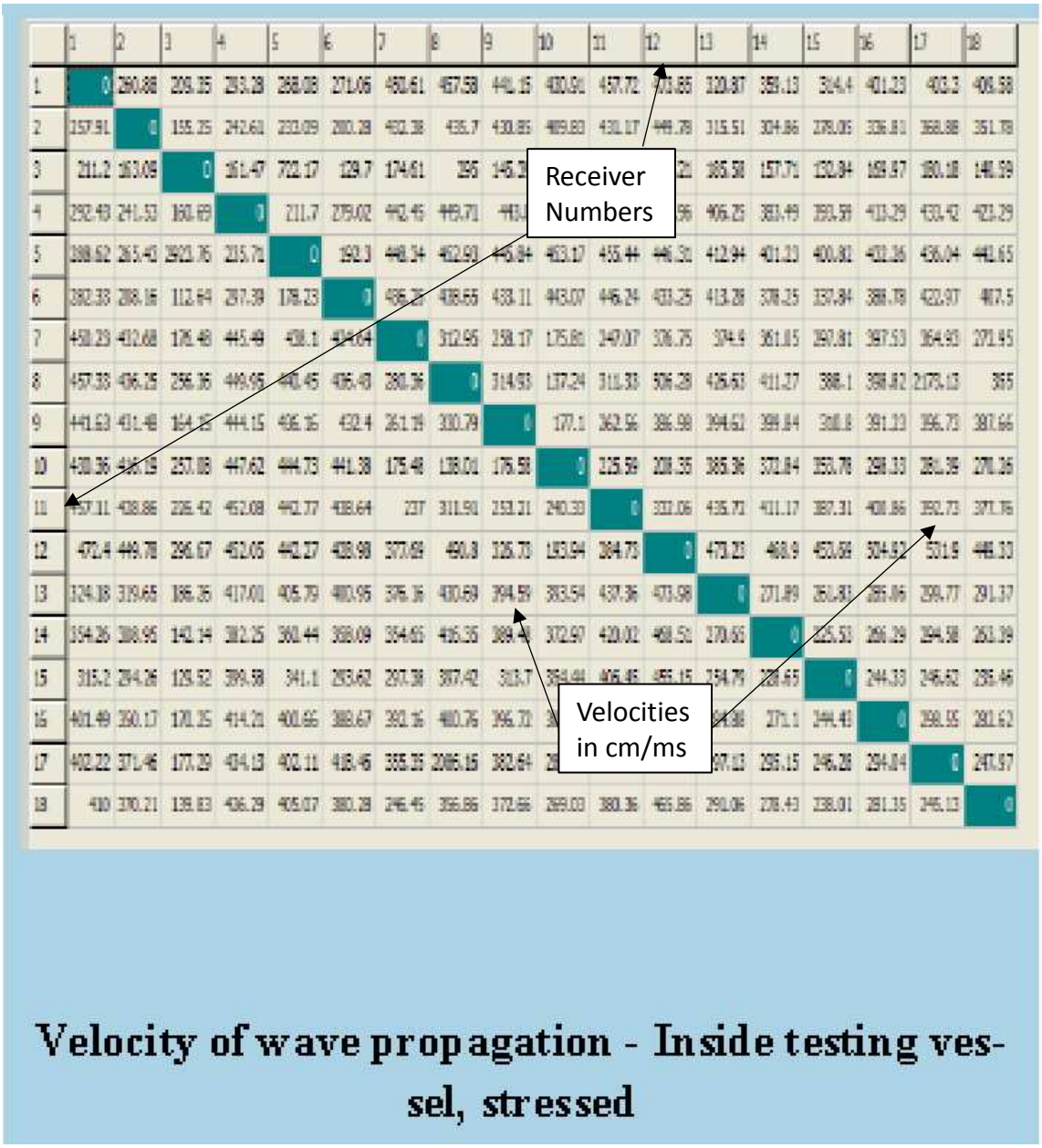

For Block 2, the same target pumping rate, fluid viscosity, stress loading sequence, and final stress state were the same as for the Block 1 tests. In Figure 4.14 one can see five traces versus time. The three largely horizontal flat curves (light blue, pink, and green) reflect the pressures applied to the surface of the Block in the tri-axial press. These pressures were stepped up through the loading sequence in Table 4.1 and stabilized at the final experimental stress state of 4200 psi vertical, 2400 psi maximum horizontal, and 1400 psi minimum horizontal, prior to beginning this recording.

The two other curves, purple and blue, reflect the injected volume, and the injection pressure respectively. The maximum pressure of 3869 psi was reached at 93 minutes and 56.3 seconds of the test. The cumulative injected volume was 358.5 ml of fluid injected at that point. Note that this volume injected was almost double what was injected in the Block 1 test at this point. A gunshot loud pop was heard throughout the laboratory and the pressure curve fell by about 1200 psi almost immediately. Then the system began re-pressurizing the fluid filled crack eventually getting to 3700 psi at 97 minutes and 24.7 seconds before flow was reversed in the crack. At this point, 393.2 ml of fluid had been pumped into the system.

As soon as significant pressure was seen on the minimum stress pair of flat jacks, the pumping was stopped and a manual pressure decay started. This process was not automated and so there is variance test-to-test. Detecting the fracture initiation is done by closely monitoring the detected pressure on the minimum horizontal stress flat jacks; in this case the light green pressure curve. The interpreted fracture initiation

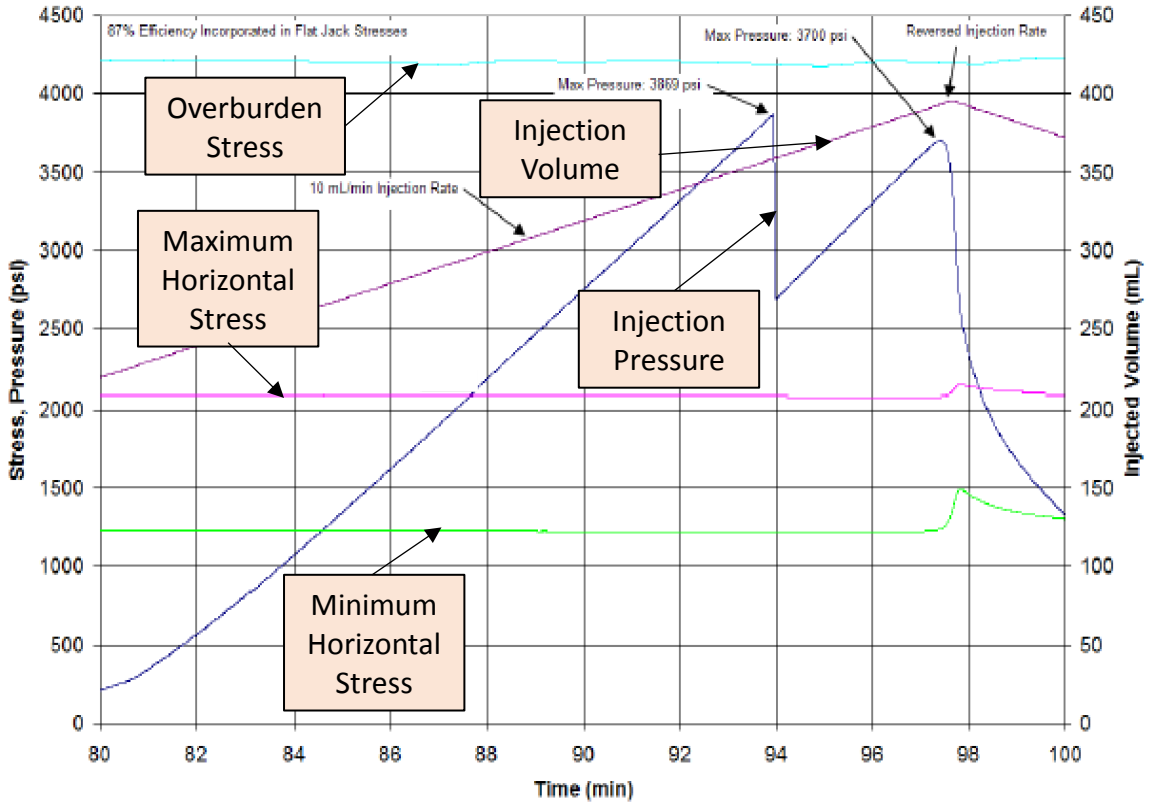

Figure 4.14 – Block 2 treatment pressures, tri-axial stresses and cumulative injection volume. Pressures and stress on the left y-axis in psi. Injection volume in ml on the right y-axis. Treatment time in minutes along the x-axis.

is done by closely monitoring the detected pressure on the minimum horizontal stress flat jacks; in this case the light green pressure curve. The interpreted fracture initiation for this test occurred at 97 minutes and 13 seconds into the test with a flat jack pressure on the minimum stress flat jacks of 1411 psi and an injected volume of 391.23 ml of liquid. The end of the fracture was interpreted to be at 97 minutes and 39.6 seconds at a minimum stress flat jack pressure of 1569 psi and an injected volume of 395.39 ml of fluid. In summary, the fracture grew for 27 seconds and took a fluid volume of 4.16 ml. The fracture in the second block took half as long to grow and took two-thirds of the fluid that the fracture in the first block took.

Clearly this test was very much unlike the first block test. In fact, two fractures were created. The first one was a horizontal fracture along the top bedding plane between the Lyon's sandstone and the cement. After removal from the press, it could be seen that the epoxy had not effectively sealed the well bore down around the end of the casing. This helps explain the much larger volume of fluid injected into what should be a very similar crack volume. The loud noise generated was the instantaneous delamination of the block at the boundary between the two materials. Once the shear stress was relieved, the vertical crack continued to grow as in the other experiment.

The massive and nearly instantaneous horizontal fracture delamination event was caused by two factors: 1) the strong horizontal stress created by the transfer of the overburden stress through Poisson's ratio into a modeled horizontal stress contrast of about 630 psi (Alqahtani 2010) and the loss of well bore isolation due to a poor epoxy fabrication job. But it also affords us a look at a massive fracture which only grew to relieve the shear stress and then immediately closed back up due to the overwhelming overburden stress.

This likely provides a visual picture of the fluid lag zone first detected in the Casas (2005) experiment using pressure probes to detect the advancing fracture tip and the first arrival of the fluid front behind it. Casas used a first derivative of the pressure curve to estimate the dimensions of this fluid lag at between 0.15 inches and 0.3 inches depending on which of the two fractures he analyzed (Note also that different pumping rates were used between those two fractures). However, if one takes the estimated fracture rate from his data and the time delay between the loss of pressure (the tip passing) and the sudden rise in pressure (the arrival of the fluid front), this lag zone is

estimated at almost exactly four inches in both his experiments. In Figure 4.15 you will note the visual fluid front of the horizontal fracture and the dry portion of the fracture indicating a corroborating dimension of approximately four inches.

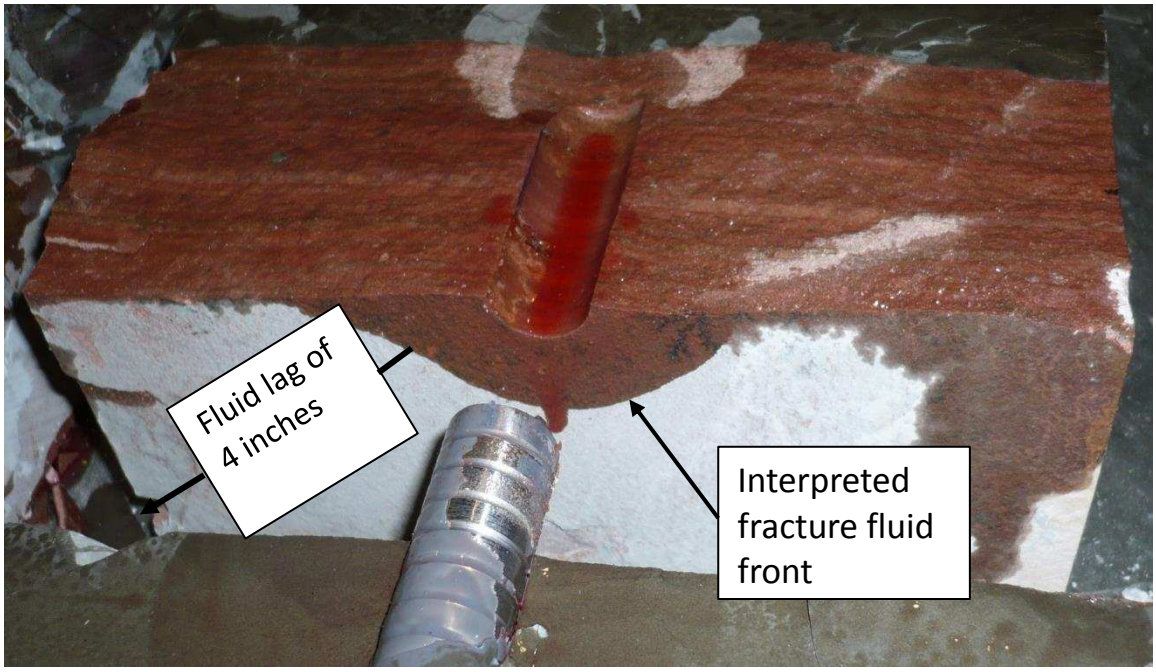

Figure 4.15 – Block 2 horizontal fracture fluid lag. The fluid front can be clearly seen to only advance about one inch into the fracture yet the fracture progressed the full five inches from the wellbore to the edge of the sample.

The microseismic activity also shows a very different picture in that there are three distinct periods of increased microseismicity. At about 420 seconds (the pressure and acoustic time scales are not synchronized. A correction of about 57 minutes is needed to compare the two) on the display in Figure 4.16, a large number of acoustic emissions are detected and a bump in the detected stress on the flat jacks occurred. This is labeled as “Loss of Isolation?” on the graph. The interpretation for this event is that the injected fluid ruptured the epoxy seal around the steel wellbore allowing fluid to

migrate in voids along the wellbore and dilate the rock along the wellbore creating the increased stress sensed at the flat jacks.

Then at about 2200 seconds in Figure 4.16 (corresponding to about 93 minutes and 40 seconds on the pressure plot in Figure 4.14) another surge in microseismic activity was detected. This is interpreted as the instantaneous delamination of the block with a horizontal fracture at the top of the Lyon's sandstone boundary. Once the shear stress is relieved and maintaining the overburden pressure, at about 2400 seconds (corresponding to 97 minutes, 13 seconds on the pressure plot in Figure 4.14) the normal behavior of a vertical fracture growing along maximum horizontal stress is seen.

The acoustically quiet period immediately following the fracture and cessation of pumping is not seen on Figure 4.16 only because the recording was not long enough. Close investigation of Figure 4.17 shows the histogram of acoustical emissions and the characteristic "eye-of-the-storm' quiet period immediately after the fracture passed and pumping stops. The interpretation of this phenomenon is that first the block stabilizes under the external stresses placed upon it. During this stabilization period the microseisms that are going to occur have happened and the block has become acoustically quiet.

Then the fracture initiates and there are a sizeable number of acoustic events due to the stress perturbations of the tip mechanics and the dilating of the fluid filled crack. In essence, significant new stress is placed on the block due to this dilation and a high amount of seismicity is observed. Once pumping stops, and subsequently (remember wellbore storage effects) no more dilation occurs, the system stabilizes once

more (no more changing of the stress state) and it becomes acoustically quiet again. But as the pressure in the wellbore continues to fall, fluid is removed from the dilated crack and once again there is a relaxation of stress. This relaxation again causes a change in the stress state which causes the second resurgence of acoustical emissions.

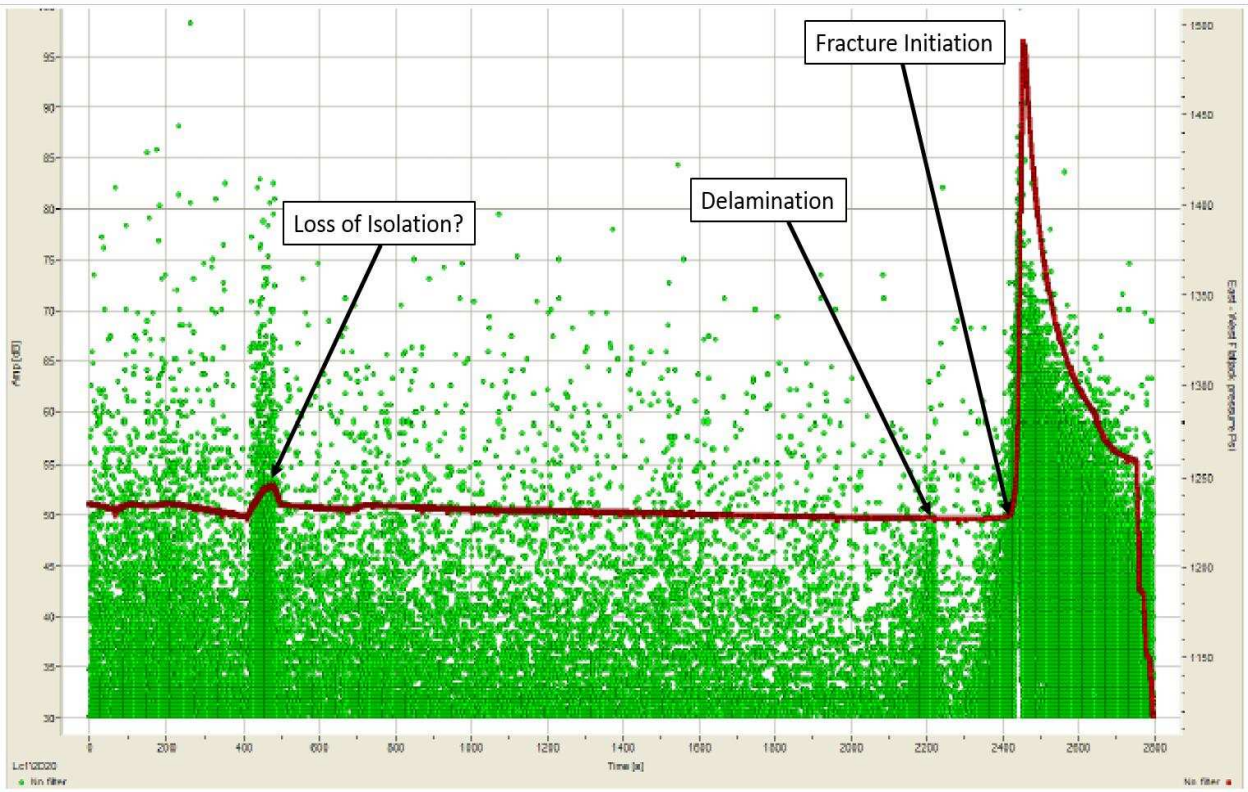

Figure 4.16 – Block 2 acoustic emissions (in green) and minimum horizontal stress flat jack sensed pressure (in red). Green event microseisms occur at the time of treatment indicated on the x-axis in terms of seconds from injection start time and with relative amplitudes in dB as indicated on the left y-axis. The pressure sensed on the minimum stress flat jacks is the one to show fracture dilation strain which causes the jump in the measured pressures as shown on the right y-axis in psi.

One very important conclusion can be made from observing these data. The amount of seismicity is approximately equal from the increasing stress of the advancing (and dilating) fracture as is due to the receding and associated stress reduction after

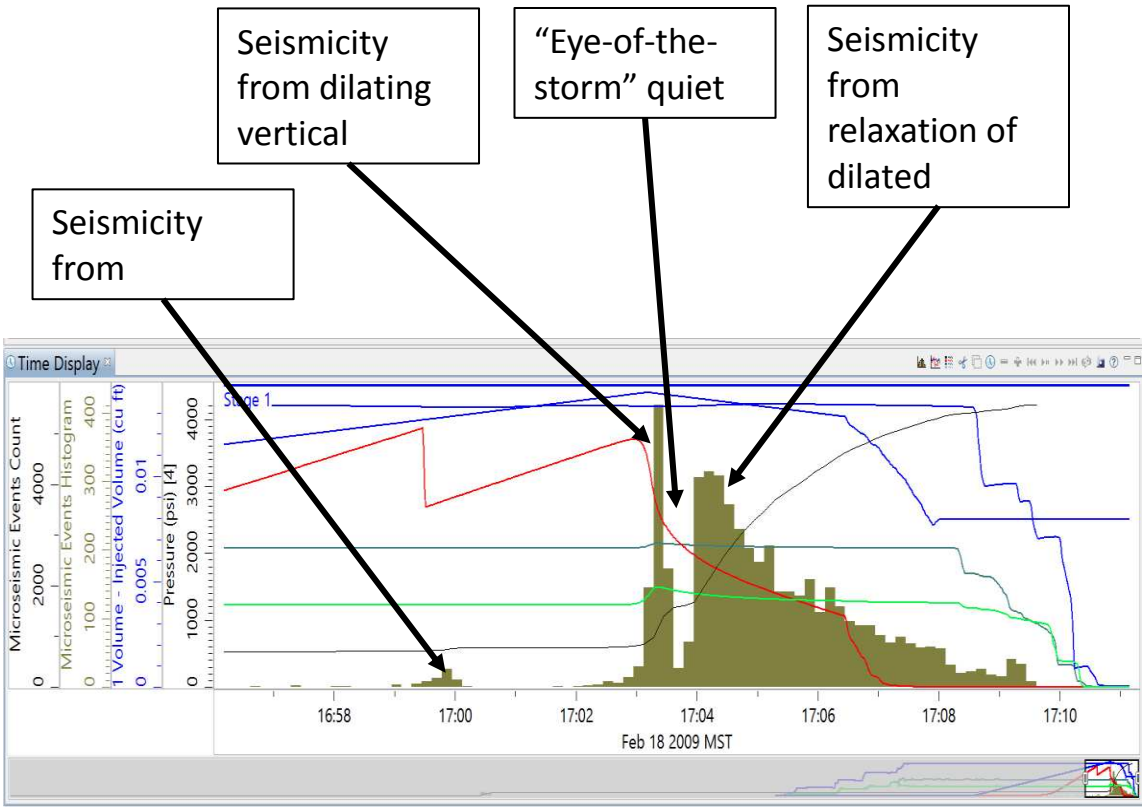

Figure 4.17 – Histogram of Block 2 acoustic emissions as the fracture tip passes and the pumping is stopped. Time runs along the X-axis and pumping pressure and stress curves are plotted in different colors over the seismicity histogram. The characteristic quiet period associated with a stabilized stress state from no more dilation but prior to relaxation is termed here “the eye-of-the-storm”.

cessation of pumping. This leads us to believe that the seismicity and driving stress changes are due far more to the fluid dilation stress effect than due to the advancing tip facture mechanics.

This second block had eighteen receivers, six P-wave and twelve shear- wave, strategically located on the block faces in the Lyons sandstone unit to optimize direct arrival energy and minimize duplicate ray path ambiguity. However, laboratory conditions are among the most difficult due to all the other modes of energy that are picked up by the receivers. Each free surface provides an excellent acoustic impedance

contrast to reflect energy back into the block. This is similar to the free surface 'multiple' problem experienced in conventional seismic reflection recording. However, there are far fewer receivers, less regular data, and six times as many free surfaces to reflect off of.

There is no facility to discriminate between shear wave and compressional waves. The software has no understanding of these two modes. So, either you take all time picks and use a compressional wave velocity to image them, or you take all time picks and use a shear wave velocity to image them. Figure 4.18 shows the actual waveform data from one of the typical microseismic events after the fracture has initiated. As you can see from the data, the first break picks are in fact much higher signal-to-noise ratio than typical field recorded microseismic data. The fact that the first break picks are not linear across all receivers is due to the special geometry of the receivers on the block (on all sides) relative to what is typically seen in down-hole field microseismic recording.

No facility exists in the processing software to exploit *both* the P-wave and shear wave data simultaneously (like is commonly done in processing field microseismic results). The internal Vallene software is really only capable of handling one mode of direct arrival energy. Coupled with this limitation is the fact that shear wave receivers on three orthogonal faces of a cube are actually quite good at picking up P-waves. In the end, the idea of using shear wave receivers to utilize the P-wave to shear wave separation as a localization method was overly optimistic. Hence, all data was treated as P-wave data with compressional velocities. Unexpectedly, using 2.5 times as many receivers (and two-thirds of them in theory not optimized to pick up compressional

energy) resulted in approximately 50 times more detected events at the same level of precision as shown in Figure 4.16 (assuming we use the LUCY number of 1 as the cut off criteria).

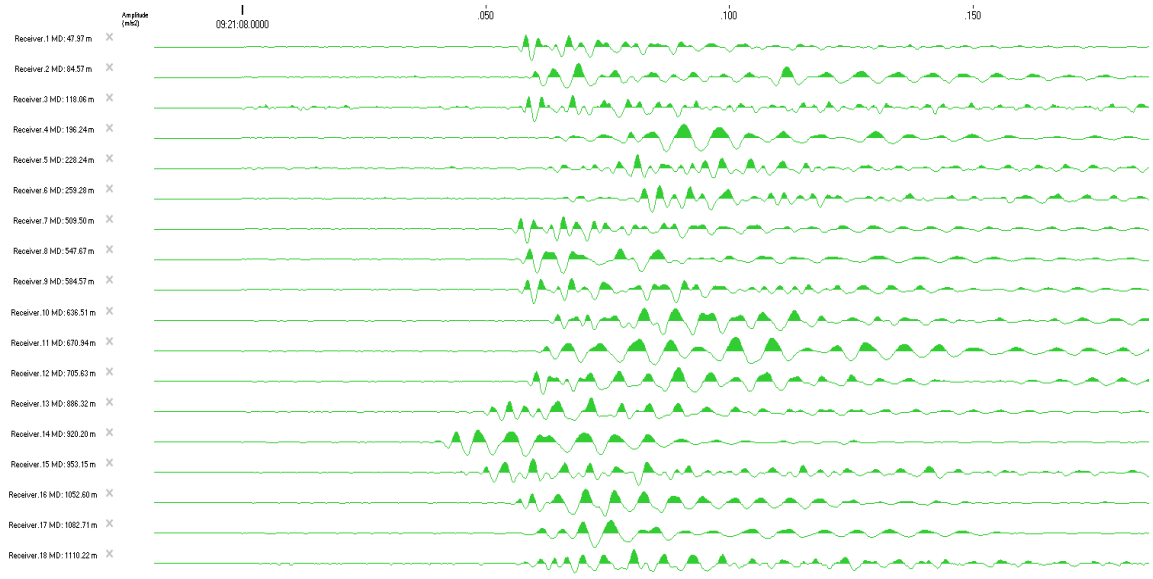

Figure 4.18 – Block 2 raw waveform data from a typical event recorded onto all 18 channels. Note that 12 of these channels are actually shear wave transducers. Excellent signal-to-noise ratios were common throughout the data set.

For the entire duration of the experiment, the total number of events detected that produced a solution (four or more time picks in the window) for a common source was 139,872 (Figure 4.19). Only 114,427 were valid (had the Vallene requirement of five or more valid time picks in the window). Further constraining the localized events to have occurred inside the block (thereby eliminating many of the multiples) reduced the number of events to 85,118 and, of those, fewer and fewer met the constraints of tighter LUCY numbers. A LUCY number of 0.1 inches was selected (although a ten times

tighter solution tolerance than used for Block 1) so as to not overwhelm the display with the microseismic events. 971 events met the constraint of having a LUCY uncertainty number of less than 0.1 and is a similar total number of events as used in Block 1 which used a LUCY number of 1.0. This is about the number of microseismic events one would detect for an entire well bore in practice, although that would be for several stages of stimulation.

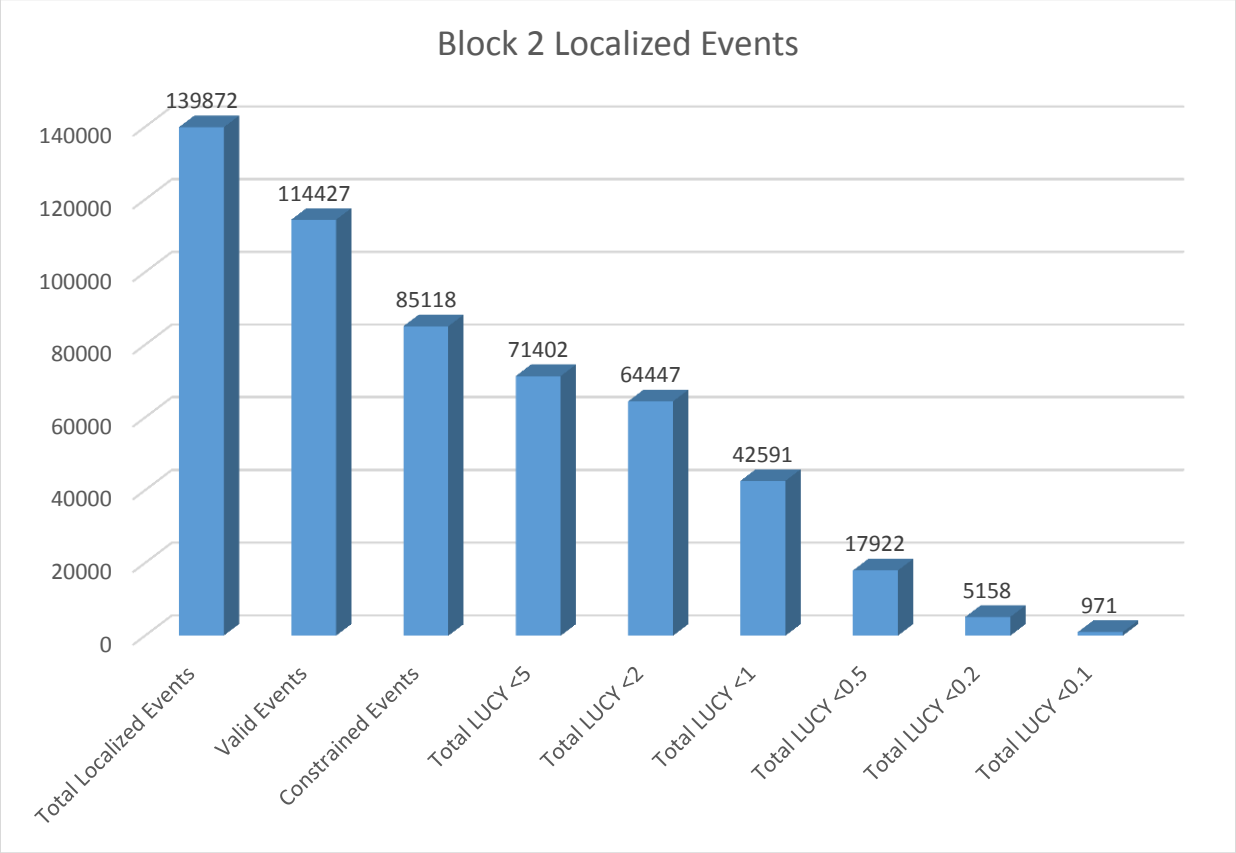

Figure 4.19 – Block 2 total numbers of localized events versus the LUCY (location uncertainty) number. Note, the LUCY number represents the location uncertainty in inches just as in the first block in Figure 4.11.

The aerial view of the block (looking down) with all the events posted having LUCY less than 0.2 is shown in Figure 4.20. The cross section view is shown in Figure 4.21 and the end-on view is shown in Figure 4.22.

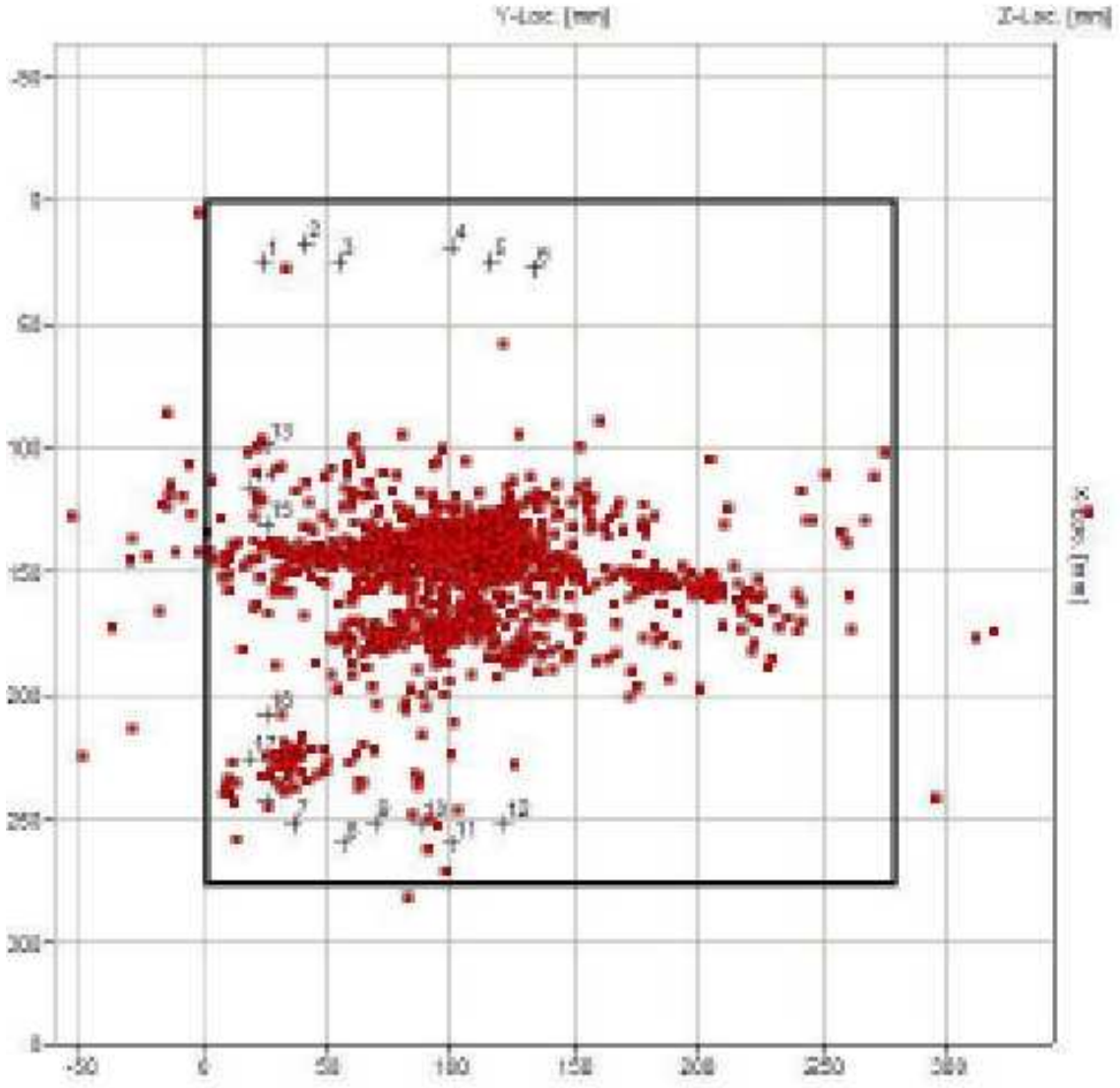

Figure 4.20 – Block 2 aerial view of localized events looking down onto the top of the block outlined in the bold black outline. You can see how the red localized microseisms align very well from the center of the block and emanate in a roughly linear manner in the direction of maximum horizontal stress (right to left).

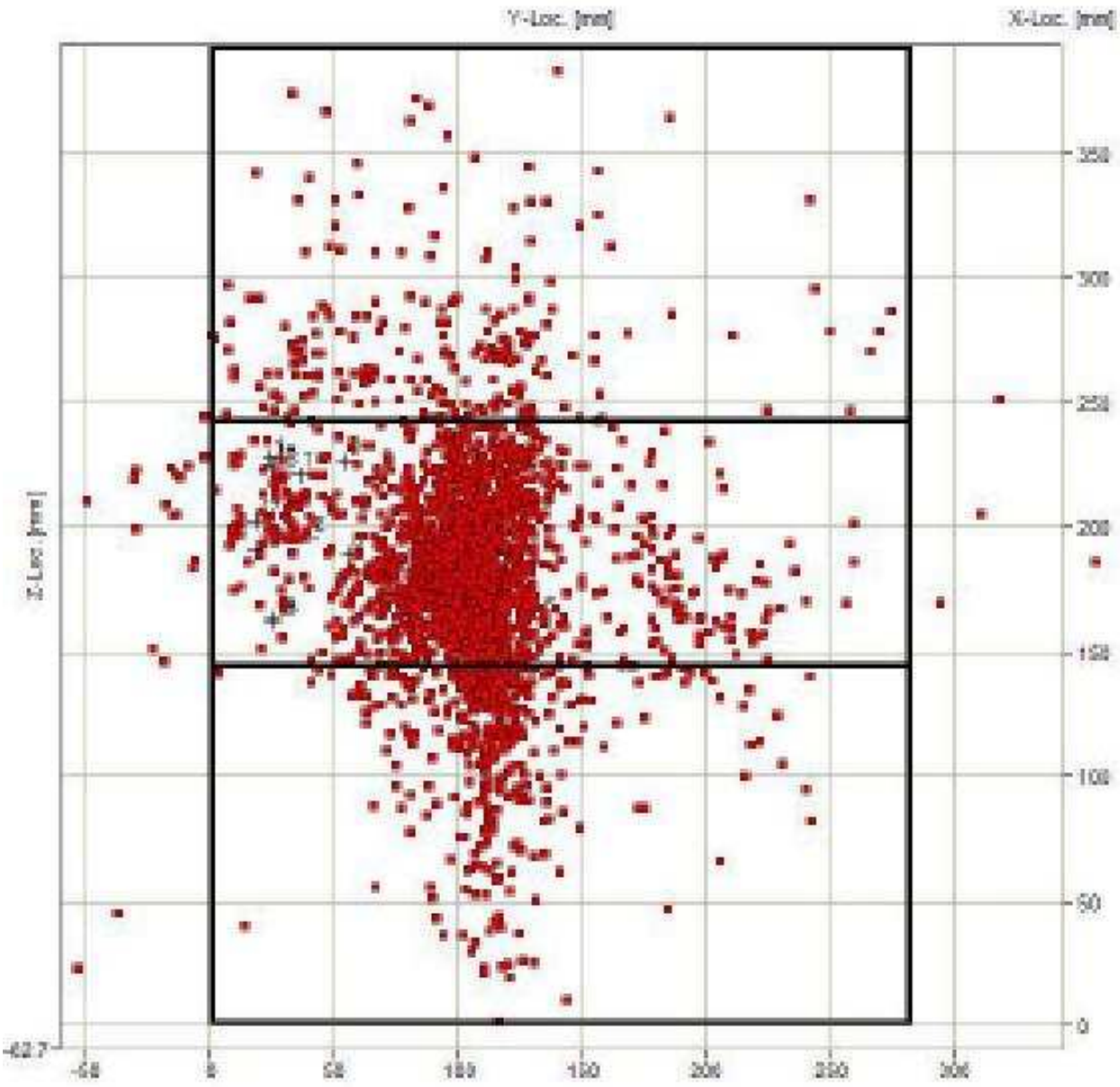

Figure 4.21 – Block 2 cross section view of localized events looking at the side of the block. The black horizontal lines inside the block delineate the top and bottom of the sandstone layer in which the fracture was initiated. You can see how the red localized microseisms are largely concentrated in the sandstone layer.

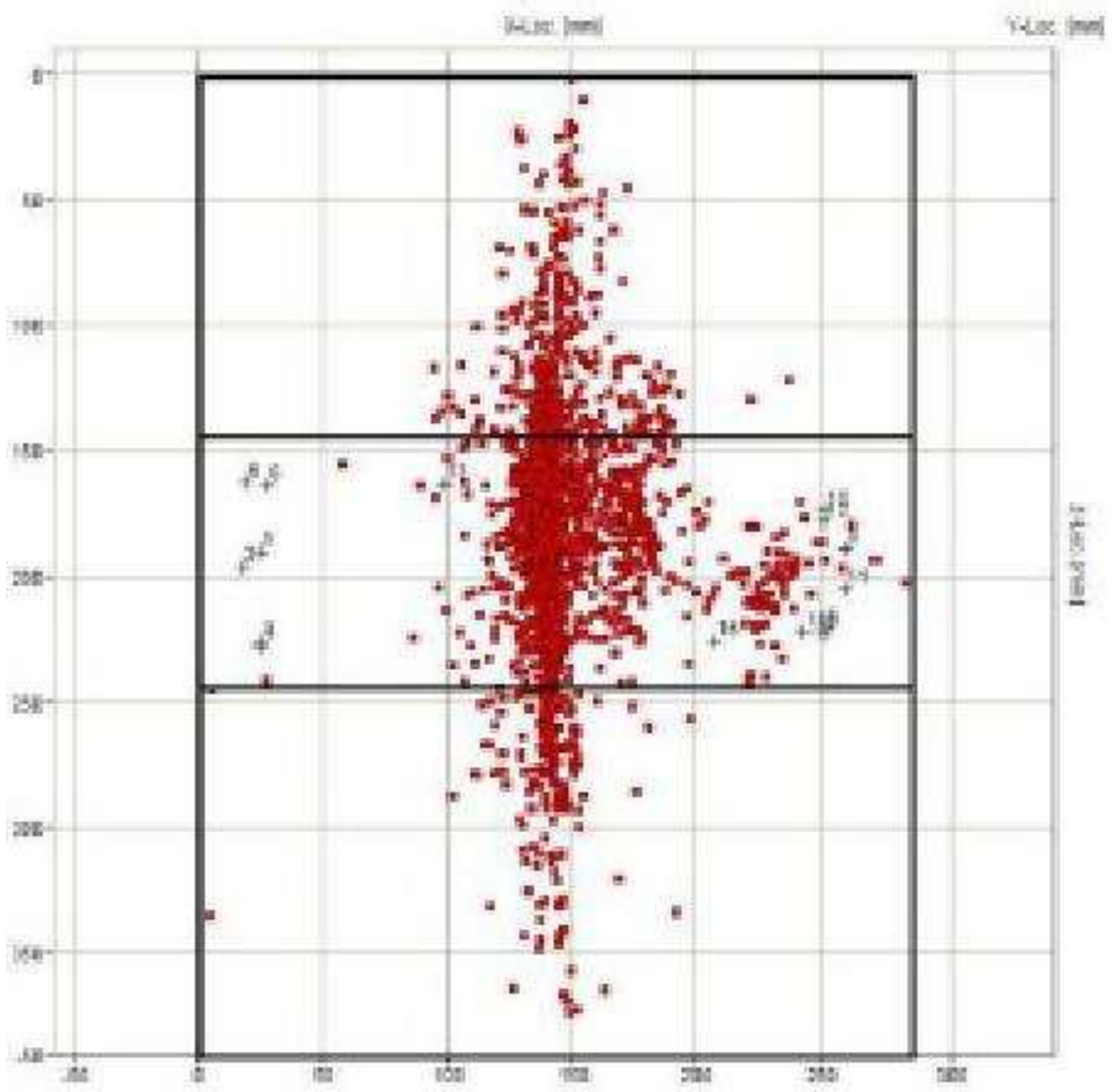

Figure 4.22 – Block 2 end-on view of localized events looking down the fracture along maximum horizontal stress. You can see how the red localized microseisms are almost completely trapped within the sandstone layer and produce a largely vertical fracture plane aligned with the wellbore in the center of the block. The two black horizontal lines within the block delineate the top and bottom of the sandstone layer.

CHAPTER 5

DISCUSSION OF RESULTS

This chapter reviews the results obtained in the research. It identifies the successful answers to questions posed, but it also identifies areas of unexpected results, and/or limitations in definitively answering some of the original objectives posed. As a refresher it is worthwhile to revisit what the original intentions of the research where:

1. Prove the effective use of a seismic acquisition system in the laboratory conditions for hydraulic fracture testing;
2. Better understand the behavior of the controlled hydraulic fracture as it impinges upon a known material boundary interface; and,
3. Quantify the differences between the physical fracture dimensions and those indicated by indirect microseismic mapping.

5.1 Effective Use of Passive Acoustic Monitoring in the Laboratory

This project, the first one of its kind attempted in the TerraTek laboratories, but also one of the very first, and most comprehensive uses of passive microseismic in a lab for hydraulic fracture testing at this scale anywhere. Microseismic data were acquired, were processed, and did reveal microseismic activity associated with the creation of the hydraulic fracture. These results, even for a first experiment, were of similar quality as those from field work that has been evolving for decades. Some key

learnings were also made to allow further optimization of the use of this technology in the future.

Receiver Size - the decision was made to go with relatively large (and sensitive) receivers due to the fact that the size of expected signals was not known. This was a last minute choice after smaller, true three component collocated receivers were fabricated in the Rock Abuse lab at CSM. These were however not used due to the possibility that they were too small to be sensitive enough to detect the low level signals being generated. In hindsight, the signal levels recorded were large enough to have been detected with the fabricated three component receivers. These receivers had the advantage of being low enough cost that they could be epoxied to the rock face (increasing their coupling) and not reused. Further, with all three receivers being collocated, the use of industry accepted P-wave to S-wave time difference algorithms could have been used as was the original intent.

Receiver Placement – significant effort was expended to model and attempt to place the receivers such that duplicate time arrival paths would not confuse the processing algorithms. This was probably more effort than it was worth with the very fine sample rates used in the acquisition system and the ability of the internal processing package to handle duplicate time arrival differences. Different processing packages may not exhibit this level of robustness, but the internal Vallene package did.

Numbers of Receivers – this experiment, with all other factors being held constant, had one test with eight receivers and one test with 18 receivers. The results from the higher number of receivers were astronomically better. Fifty times as many

events were detected, and the location error was ten times more precise. These results are far more dramatic than expected and show the high value of a larger number of receivers. There is likely to be a point of diminishing returns but clearly 18 receivers was much more beneficial than the eight used in the first test. TerraTek has continued to increase the number of receivers with experiments using 36 receivers and are planning even higher channel counts in the future (personal communication with Aniket Surdi, Salt Lake City, April, 2015).

Use of Shear Wave Receivers – the original plan was to use shear wave receivers (much as are used in field recordings) and the wealth of P-wave to S-wave time difference algorithms to locate the events as well as other source characterization parameters. This capability got compromised when the three-component receivers were not co-located. However, for the small sample size in the laboratory, the angles of arrival energy into the surface mounted receivers meant that the shear wave receivers were also excellent at picking up P-wave energy. For this reason, the 18 channel results (of which 12 channels were shear wave sensors) were very effective at detecting and processing P-wave energy and localizing the microseisms associated with this. Presumably, equivalent results could have been obtained with 18 P-wave receivers instead of the mix of receiver type used. However, should a more exhaustive analysis of the waveform data be performed to characterize the source parameters, the S-wave receivers and identified waveforms must be used.

While co-locating the receivers is prerequisite to utilize existing commercial processing mode time-difference based algorithms, it is possibly that the significant advantage the 18 receivers produced in this experiment were ostensibly better because

they were not collocated. In effect there were 18 unique receiver locations. These 18 unique locations may very likely have produced better results than six three-component locations could have using mixed mode processing algorithms.

One unexpected result obtained with the use of the acoustic monitoring system, which was observed but unfortunately not recorded, was the high level of microseismicity associated with relatively small changes in the block's stress state. By accident, the acoustic monitoring system was left on while the sample was brought up to the final designed stress state. Making stress changes as small as 200 psi produced an apparent log-normal distribution of acoustic events than would instantly begin with the stress increase and then die down over the period of three to ten minutes. This was repeated at each stress step increase up to the final stress state. None of these stress increases was anywhere close to the fracture gradient of the material. Hence, a significant amount of microseismicity was observed well below the stresses necessary to fracture the rock.

This means that normal rock samples are meta-stable. They have been under a host of different paleo-stress regimes while they were being lithified. In their current state they have thousands and thousands of grain-to-grain contacts under differing levels of stress that have finally reached equilibrium. There are no more grain-to-grain slippages and they are acoustically quiet. This all changes when even the smallest stress is applied to the sample. The theory being that at least one of those grain-to-grain contacts is at or near the critical stress level to cause slippage. Applying an external stress to the block with be enough to cause several of these grain-to-grain contacts near critical stress to slip and produce the acoustical signature of a microseism. This

microseismic activity below the fracture gradient is seen both as the stresses are increased in the block under test, but also as the stresses are reduced after the test is complete.

It is not an uncommon perception in the microseismic and hydraulic fracturing industry to associate microseismicity with the advancement of a hydraulic fracture. This in fact is generally a very valid assumption corroborated by reams of data collected over the years but, as the results found in this test show, this is not the only source of microseismicity. In other words, it is generally valid to say advancing hydraulic fracture equals microseismicity. But the reverse is not true. Microseismicity does not necessarily equal advancing hydraulic fracture. As shown here, any small change in the stress state is the source of the microseismicity. One common source of changing stress state happens to be an advancing hydraulic fracture.

This is an important result for those hoping to take a microseismic display as a proxy for the geometry of a hydraulic fracture. The earthquake seismologists have understood this relationship for a long time; that any small stress perturbation may be enough to cause the slip along a critically stressed fracture. However, the hydraulic fracturing practitioners have struggled mightily to accept how hydraulic fracturing operations could possibly cause microseismicity (and sometimes not so micro) at any significant distance from the advancing fracture tip. Stress changes can and do propagate away from the disturbance and these stress changes, while small, may be enough to cause slippage along critically stressed boundaries within the rock.

These relatively small stress perturbations can also propagate a considerable distance from hydraulic fracturing operations (on the order of miles in practice) and still be large enough to trigger slippage along a pre-existing critically stressed fault. Industry attempts to limit any casual association between stress changes as a result of hydraulic fracturing and induced seismicity to the immediate proximity of the wells being fractured are not founded on solid science.

5.2 Better Understanding of Hydraulic Fracture Approaching an Interface

The work published by Casas (2005) and Athavale (2007) in the earlier FAST Consortium project quite thoroughly addressed the experimental aspects of hydraulic fractures impinging upon material interfaces. Three dominant factors influence this behavior: 1) the material property differences, 2) the stress conditions, and 3) the bonding, or adhesion, between the two interfaces.

Warpinski (1985) noted that while material properties can significantly change between layers, the dominant factor controlling the fracture is the localized stresses created by those material property changes. But without a doubt, the most dominant factor controlling fracture behavior approaching a layer boundary is the adhesion between the boundaries. Athavale (2007) showed excellent examples of how bonded and unbonded interfaces will control fracture propagation along and across that boundary.

As a result of the prior work, the effort in this experiment was to eliminate the effect of a low cohesion boundary. To the greatest extent possible, the cement to sandstone interface was made as strong as possible in these tests. Testimony to this

success is the fact that all fractures indeed did cross the interface boundary. As can be seen in Figure 5.1, both fractures were also nearly vertical between both tests. In Figure 5.2 bi-wing planar penny shaped fractures, with dimensions as shown, occurred in both tests. The fractures were elliptical in nature with aspect ratios of about three to four; height versus width (Figure 5.2). All attempts to use the injected volume of fluid and the measured fracture area to estimate the fracture width were rendered invalid due to the inability to retain the fracture within the sample. Both fractures escaped fluid outside the blocks which prevented any volume of fracture calculations impossible.

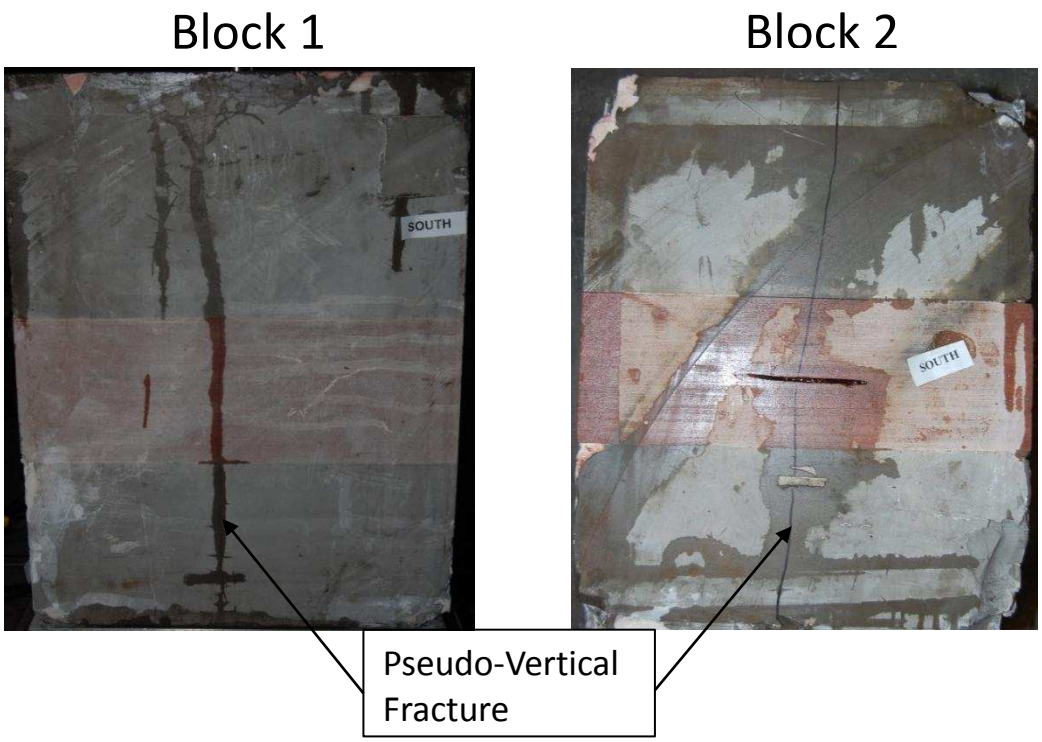

Figure 5.1 – Both blocks immediately after fracturing and removal from test frame. The dark pseudo vertical line on both blocks is the intersection of the fracture and the block wall. In Block 1, this fracture was completely fluid saturated as the fracture blew out the side of the block. For Block 2, a pressure relief cut was made preserving the fracture intersection that was subsequently marked with a black felt tip marker as shown.

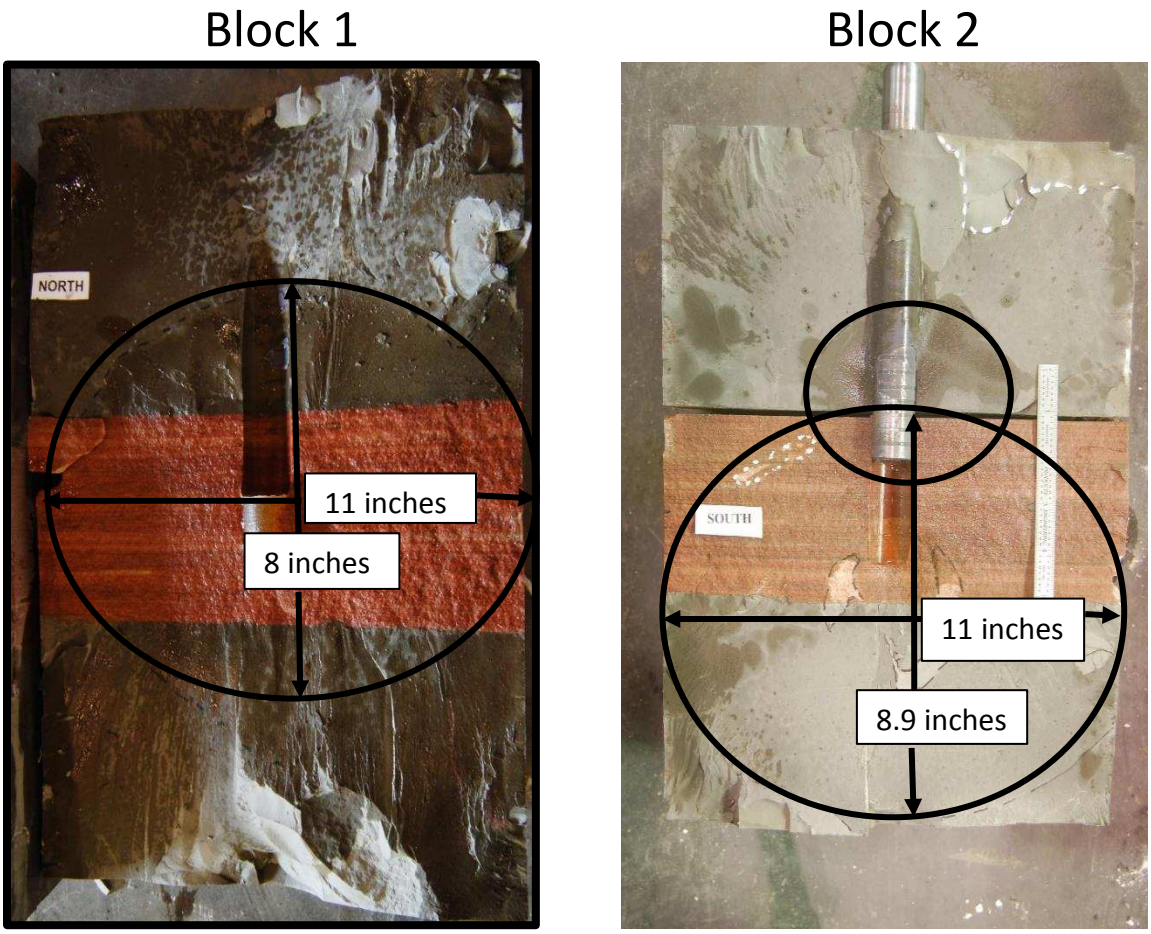

Figure 5.2 – Both blocks immediately after removal from the test frame and cracking open the rock sample along the fracture plane. The fluid boundary was marked while still fresh showing the extent and shape of the created fracture as indicated with the black ellipse in each case. Very nearly the same aspect ratio for the created fracture exists in both cases. Block 2 shows a second ellipse which is probably a second fracture created when the wellbore lost integrity and delaminated the sample creating another fracture initiation point.

Both samples had no external differences in the applied horizontal stresses vertically along the block. The two primary factors causing the fracture geometry to not be circular in nature are: 1) the predicted fracture tip blunting from a higher Poisson's ratio material in the cement layer, and 2) the induced stress change in the cement layer due to the conversion of overburden stress into differential horizontal stress on the order

of 600 psi along the cement to sandstone interface (Alqahtani 2010). The material induced stress change is the most likely candidate as per Warpinski's early work in this area.

What is of particular interest is the second, smaller ellipse of a fracture created above the larger one in Block 2. Recall that this block had an operational problem when the wellbore lost integrity due to an imperfect epoxy seal about the wellbore. Injected fracturing fluid was able to make its way up the imperfectly sealed wellbore to the sandstone-cement interface. This coupled with the modeled 630 psi shear stress along that interface caused the entire sample to virtually instantaneously delaminate along the cement-sandstone boundary. This also created a new fluid conduit from the wellbore to the formation which created a secondary fracture ellipse centered at the cement-sandstone interface.

This unplanned experimental result demonstrates how a growing fracture can arrest and restart in a different place due to a host of different conditions. This new fracture initiation point then builds a fracture governed by the same physics but from a different initiation point. In this case, both fractures grew in the same plane. In the field these fracture disruptions could often be due to breaking into a natural fracture system. The resulting secondary fracture may not be in the same plane as the original. This then shows experimental evidence of how fracture complexity can occur.

5.3 Compare Fracture Geometry to that Indicated by Microseismic

As stated in the previous section, microseismicity results from changes in the stress environment. While an advancing fracture front does, in fact, create a very significant moving stress perturbation, a sizeable zone associated with the fracture sees this altered stress environment. In the case of the laboratory experiment conducted here, two virtually identical blocks were fractured with virtually the identical pumping treatment schedule. The main difference was the number, and type of transducers used to record the signals. There was also an operational problem with the loss of wellbore containment in the second experiment.

From Figure 5.2, it can be seen that the fracture initiated in the sandstone layer and propagated outward eventually crossing into the bounding cement layers both above and below the sandwiched sandstone layer. It is expected, with the myriad of grain-to-grain boundaries and a likely pre-existing stress environment when the sandstone was lithified, that most of the acoustic emissions would come from this layer. In fact this is the case as can be seen in Figure 5.3. Even though there is a large discrepancy between the numbers of events in the two different blocks (due primarily to different numbers of receivers) and with different tolerances of location accuracy, largely the same percentage of the microseismicity come from the sandstone layer as predicted.

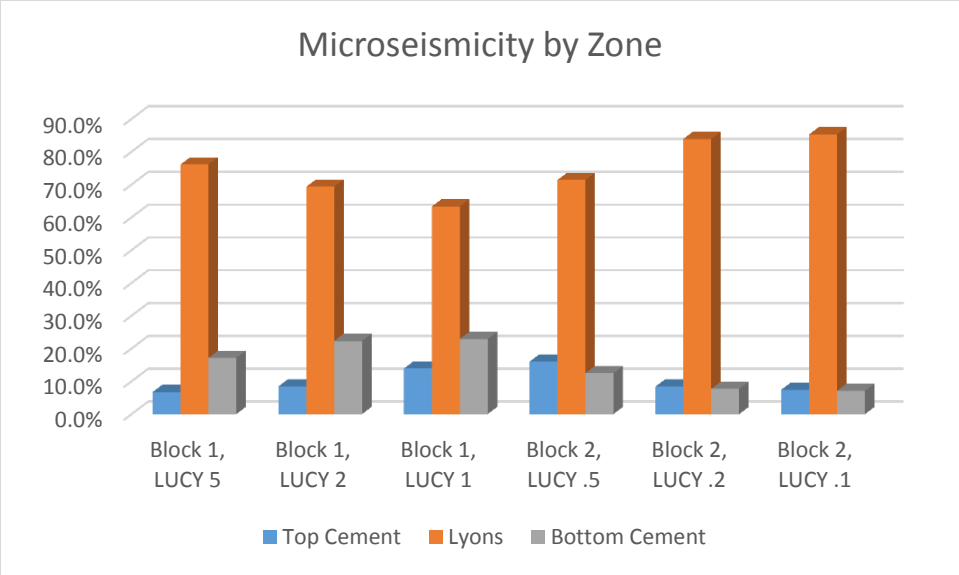

Figure 5.3 – A comparison of what percentage of microseismic event locations are located in the bounding cement layers versus the Lyons sandstone layer. Using three different LUCY number (location uncertainty) which yield radically different numbers of localized events, the percentage of those events is dominated by the sandstone layer.

However, without being able to contain the hydraulic fracture within the block, it is not possible to map the envelope of microseismic activity to create a 'microseismically derived' fracture shape as was hoped in the original scope of the project. In hindsight a much higher viscosity fluid should have been used to promote slower quasi-static fracture growth and possibly contain the fracture inside the block, significant insight can be drawn from the microseismic event distributions.

Figure 5.3 shows that the majority of the localized microseismic events occur in the sandstone layer where the fracture was initiated, further investigation is warranted to better understand the microseismic events within the propagating fracture. First let us remember that the fracture has an advancing fracture tip controlled by all the fracture tip mechanics and the toughness of the medium through which it is propagating. Then

there is a vacuum created behind the advancing tip prior to the advancing fluid front that hydraulically pries the crack open. The fluid front functions as a hydraulic wedge forcing the crack open far wider than it is in front of this advancing fluid front. The width of the fracture depends on several variables but the geometry of the fracture and the viscosity of the fluid are the predominate factors. Most of the stress imparted upon the fracture face from the fluid and the resulting strain of the medium occur in this hydraulic wedge zone.

The distance between the advancing fracture tip and the advancing fluid front is called the fluid lag. In Figure 5.4 below from the Casas project, a pressure probe was inserted into his 30 inch Colton sandstone block and actually detected the vacuum associated with the advancing fracture tip. Knowing the distance between the wellbore face and the location of the pressure probe (5 inches) he was able to calculate the rate of stable fracture growth of 0.0158 inches per second. Three hundred seconds later the pressure began to once again climb indicating the passing fluid front. For his larger estimated 12 inch radius fracture, this calculates to be about a 4.5 inch fluid lag behind the advancing fracture tip.

The size of the fluid lag is dependent upon the size of the fracture and the fluid viscosity. With these smaller blocks the estimated radius of the fractures in these experiments is limited to between 5 and 6 inches. Hence with smaller fractures and lower viscosity fluids used, one would expect to have a fluid lag zone somewhat smaller than was experimentally observed with the pressure probe in Casas' experiment. The unexpected delamination event described earlier in Block 2 provided the corroborating

evidence of the limited fluid front advancement when the fracture delaminated Block 2 between the Lyons sandstone and the overlying cement layer.

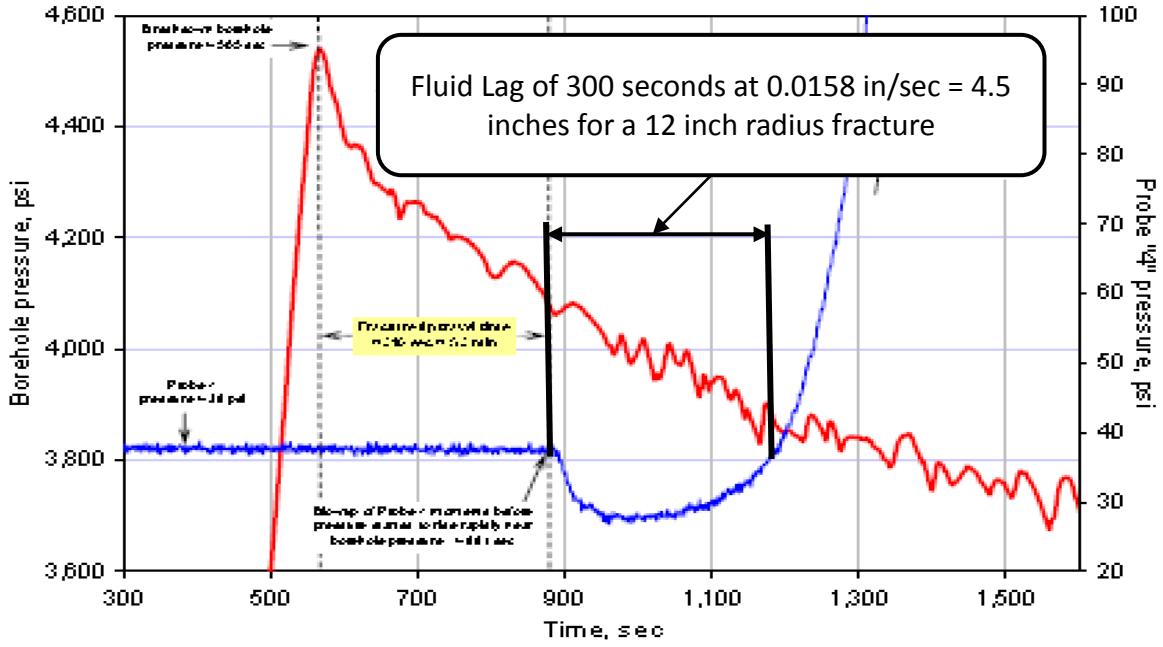

Figure 5.4 – From Casas (2005), calculated fluid lag dimension for a 12 inch estimated fracture radius. Blue curve illustrates 10 psi drop in pressure as the fracture tips passes the pressure probe before liquid front catches up 300 seconds later. Casas calculates fracture growth rate at 0.0158 inches per second.

In Figure 5.5 below, the photograph shows the post fracture delamination of Block 2. The cause of this delamination was due to a poor epoxy job in isolating the wellbore from the casing. Fluid traveled up the wellbore to the interface between the Lyons Sandstone and the overlying cement layer. As stated earlier, finite element modeling of the block indicates that an induced shear stress of approximately 630 psi exists along the sandstone – cement interface due to the stress applied and the material property differences at the interface. Once the fluid pressure reached the effective fracture gradient, the crack grew to the edge of the block relieving the shear stress

along the interface. Once that stress was relieved, the overburden stress once again prevailed and closed the crack back down. The unintended consequence of this was that it also preserved the location of the advancing fluid front in the block as seen in the picture. In this case the fluid front only extended 1.25 to 1.5 inches into the block. The distance the fracture propagates is five to six inches (wellbore face to edge of block). This then provides experimental evidence of the fluid lag dimension of between 3.75 and 4.5 inches. This finding correlates well with what Casas found in measuring the fluid lag with pressure probes.

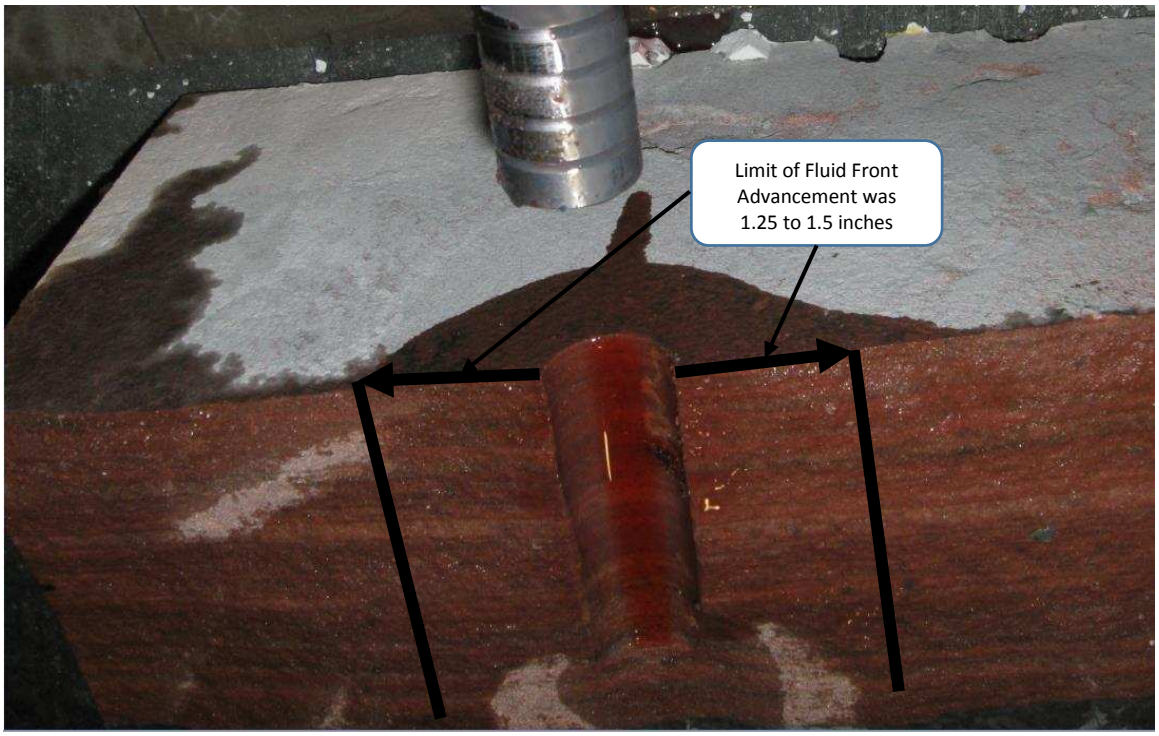

Figure 5.5 – Block 2 after hydraulic fracture treatment showing limit of advancing fluid front when catastrophic delamination event separated the Lyons sandstone layer from the overlying cement layer due to lack of wellbore containment and induced shear stress along interface. Once the fracture propagated to the edge of the block and relieved the shear stress, the fracture stopped growing, the fluid front was frozen in time, and the overburden stress closed the crack in effect re-healing the block.

In Figure 5.6, a 3D display is shown of the open fracture face with the fracture extent indicated by the faint black quasi-elliptical shape drawn on the face of the rock. On top of this is the distribution of microseismic events. Notice they align very well starting at the edge of the wellbore. While there are disparate event locations beyond the fracture front itself, a tremendous statistical preponderance of data resides not only in the sandstone layer between the borehole wall and the tip of the fracture, but that this dense accumulation of events is largely limited to the fluid dilated portion of the crack. If in fact a fluid lag lag of approximately 3.75 inches is correct, then by and large, the microseismicity is predominantly due to the stress perturbation from the advancing hydraulic wedge of the crack, not the fracture mechanics of the progressing fracture tip.

In Figure 5.7 a histogram of the number of events versus the distance from the wellbore shows that fully 93% of all microseismic events occur within the first 1.25 inches of the wellbore. This zone is therefore characterized by suffering tremendous stress changes to induce this much seismicity. The strain associated with this hydraulic wedge is interpreted to be the source of this tsunami of seismicity. Only 7% of the microseismic events characterize the rest of the advancing hydraulic fracture.

At field scale the fluid lag zone may not be of large concern when the fracture length is 100's if not 1000's or feet in length (although the fluid lag would also increase for a larger fracture), but in the lab it is important to realize that the microseismic activity is much more indicative of the advancing fluid front than from the fracture tip and all its associated stress mechanisms. Also, the detected presence of significant microseismicity in this experiment well below the fracture gradient of the material,

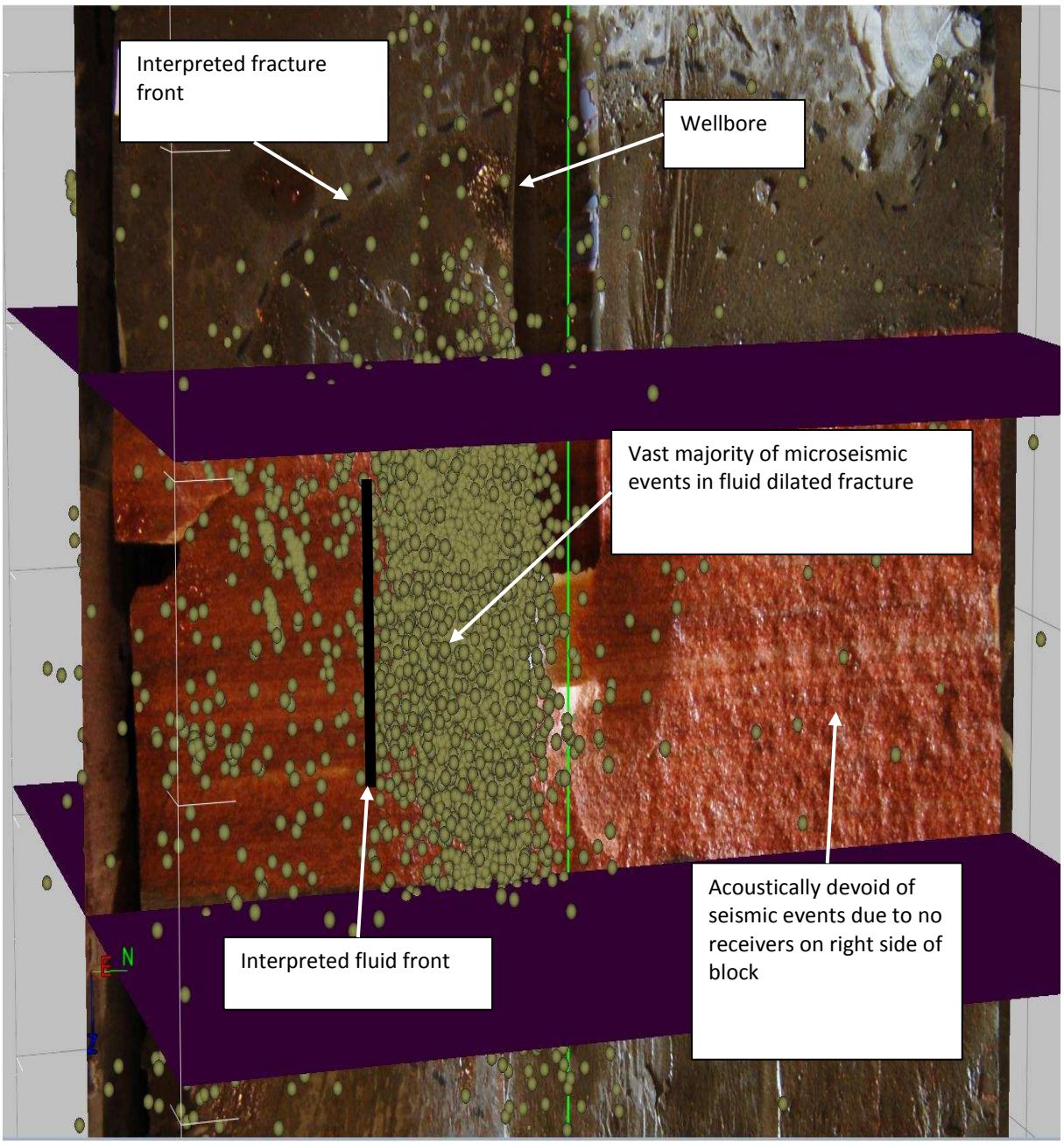

Figure 5.6 – Block 2 3D display of microseismically indicated fluid front. The fracture is indicated with a dashed black elliptical line drawn on the block itself. The distribution of the microseismic events as green dots is dominantly on the left side of the block (where the receivers were placed), between the wellbore wall and the interpreted fluid front in the fracture. Most events are constrained to the Lyons sandstone layer.

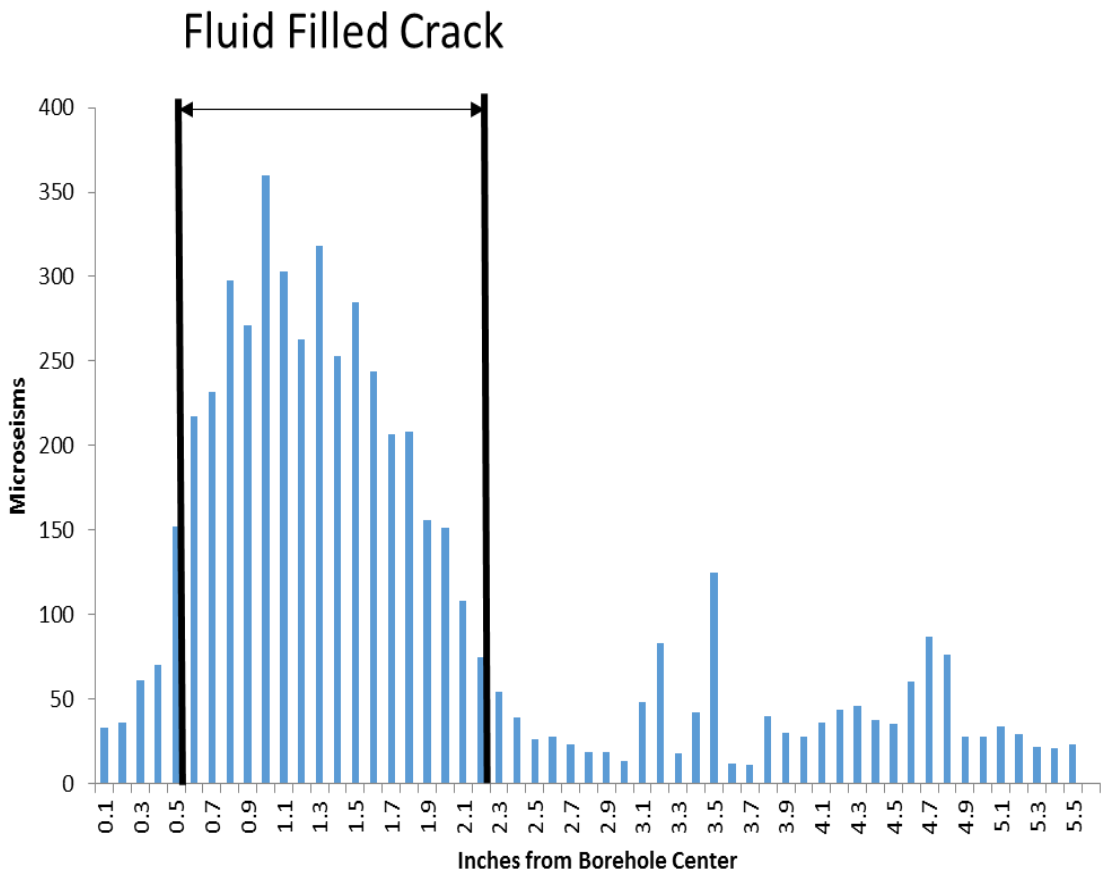

Figure 5.7 – Histogram of the distance of each microseism from the borehole. Notice the preponderance of events (93%) that fall within the interpreted fluid wedge zone versus the relative dearth of events for the rest of the hydraulic fracture.

demonstrate that the conventional wisdom in most field level microseismic surveys needs to be recalibrated as to where and why the microseismic events occur. This helps explain that a wider distribution of events, often attributed to a lack in precision locating them, may in fact be due to existing near-critical stress fracturing receiving a small necessary stress change to cause a microseism. At field scale the fluid lag behind the advancing hydraulic wedge is expected to be relatively small so the interpreted geometry of the field scale hydraulic fracture would not be expected to change much.

However, the interpretation of tip's induced shear stress being responsible for the preponderance of the shear waves we detect during hydraulic fracturing is called into question with this research.

An alternate interpretation based on the data presented in Figure 5.6 and 5.7 is that the hydraulic wedge has more of an effect than previously thought. That in fact the relatively large strain on the fracture faces due to the fluid wedge are causing an advancing shear stress differential perpendicular to the advancing fluid front. In effect a huge normal stress is placed in the fracture face at the fluid front and this occurs immediately behind a slightly negative (caused by a virtual vacuum in the lag zone) normal stress in the fluid lag zone. The differences between these two normal stresses on the fracture face provide ample shear stress to induce the majority of the microseismic activity we see in field and laboratory recordings.

CHAPTER 6

CONCLUSIONS AND FUTURE WORK

This chapter summarizes the conclusions that can be taken from this project. Some of these findings were planned, and even anticipated, in which case the data corroborated the expected outcome. But several were completely unexpected outcomes, often from a flaw in the experimental design or the operational execution of the project. No project of this extent leaves every question answered and this project is certainly no exception to that. While the benefits and value to the use of acoustic emissions in this type of laboratory work are clear, many challenges and advancements, primarily in the area of processing of the seismic signals, are needed to reap all the potential benefits.

6.1 Conclusions

Below are the primary findings and conclusions that can be reasonably derived from this research project:

1. Acoustic emission monitoring and microseismic event locations for passive recordings are quite viable in a laboratory environment. There should be at least 8 transducers to localize them in 3D, and more will yield far superior results in terms of the number of localized events as well as the precision with which the locations can be calculated. The optimal number of receivers is at least 16.
2. Using smaller and less expensive (perhaps even disposable) transducers permanently attached to the sample face, thereby establishing far better coupling, frequency bandwidth, and sensitivity, is strongly recommended. The sensitivity of the larger and more expensive transducers is not mandatory and

could be detrimental to microseism location certainty due to the smearing from the over-sized element.

3. The use of shear wave transducers should be seriously considered but only if there is a possibility for the processing of the results for source mechanism characterization. In this case the data were recorded but without a viable facility to process them. Fortunately, the geometry of the problem lends itself to multiple modes being picked up on the transducers so the shear wave transducers became very effective at picking up compressional waves as well.
4. Modeling the induced shear stresses from applying stresses to materials of differing material properties must be considered. Carefully isolating the borehole to prevent borehole fluid pressure from traveling up the borehole to the material interface is required to prevent full sample delamination as was exhibited in the second block test.
5. The stress concentration created by the geometry of a right circular cylinder borehole can cause fractures to initiate horizontally and then turn vertically as they extend across the specimen. This can be alleviated by the use of an epoxy insert at the bottom of the open borehole to dissipate the stress concentration.
6. Many spurious localized events can be eliminated by restricting the allowable uncertainty in their location and by forcing them to originate inside the sample (eliminating a large number of multiples). But this is the brute force way of dealing with a more complex problem requiring some passive seismic signal processing work, especially for laboratory conditions. As of the current date, there is still no available software for processing the full CODA suite of seismic

wave arrival modes. The theory of full Green's function solutions is well known but as of yet no commercial code solutions allow using this enhanced information. In the field these solutions would tremendously help in areas where head waves dominate the first arrival events. In the laboratory, with six nearby acoustic impedance contrast free surfaces, a tremendous number of multiple events are generated clouding the resulting localization results. Developing code to treat these events as signal versus just trying to remove them as noise would benefit our entire industry of microseismic data processing.

7. Proper materials selection, construction techniques and scale modeling must be done to design a successful laboratory scale hydraulic fracturing experiment where meaningful results can be extended to better understand the observations seen at field scale.
8. The reduction of viscosity from 100,000 cp in the previous experiment (Athavale 2007) to 1000 cp in this one was too much. This resulted in a scaled experimental time value from 508 to 86. In the pressure treatment curves from Athavale's work, the stable period of quasi-static fracture growth was already dangerously short (Figure 6.1) between approximately 20 and 30 seconds. For the work presented here (Figure 6.2) notice that there is no discernible quasi-static fracture growth period post breakdown and declining pressure fracture extension period. The fracture initiation occurs at about minute 85 and one minute later, it is complete.

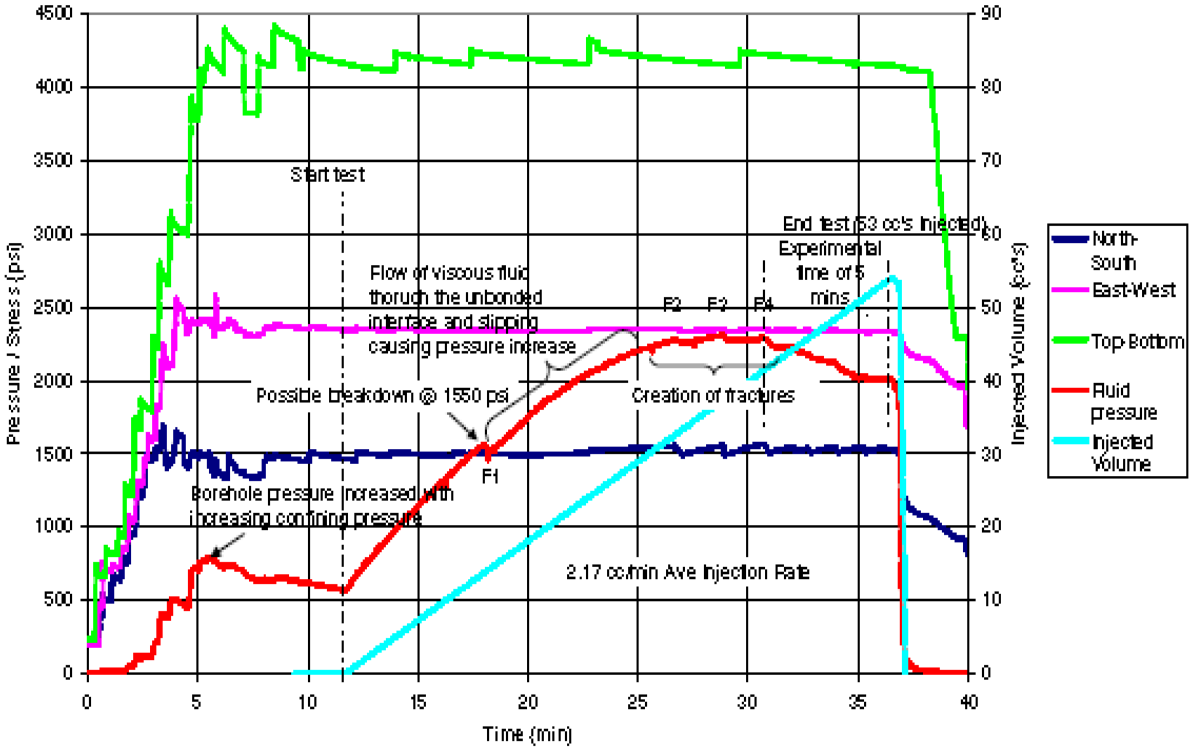

Figure 6.1 – Time pressure treatment plot for Athavale's seven layer block. Note that after the identified breakdown at about 18 minutes, quasi-static fracture growth continues until 30 or 35 minutes of injections. This stable fracture extension period is made possible with an appropriately high viscosity fluid.

6.2 Future Work

The recommendations for future work fall into three primary categories. The first is one where additional theoretical work is needed to understand the role and interaction of a few parameters we use to understand the physics at or near the tip of an advancing fracture. The second is the area of operational best practices to minimize unexpected effects from laboratory scale experiments. The last is an appeal to commit significant research to enhance our ability to correctly process the microseismic information and extract the maximum value from it.

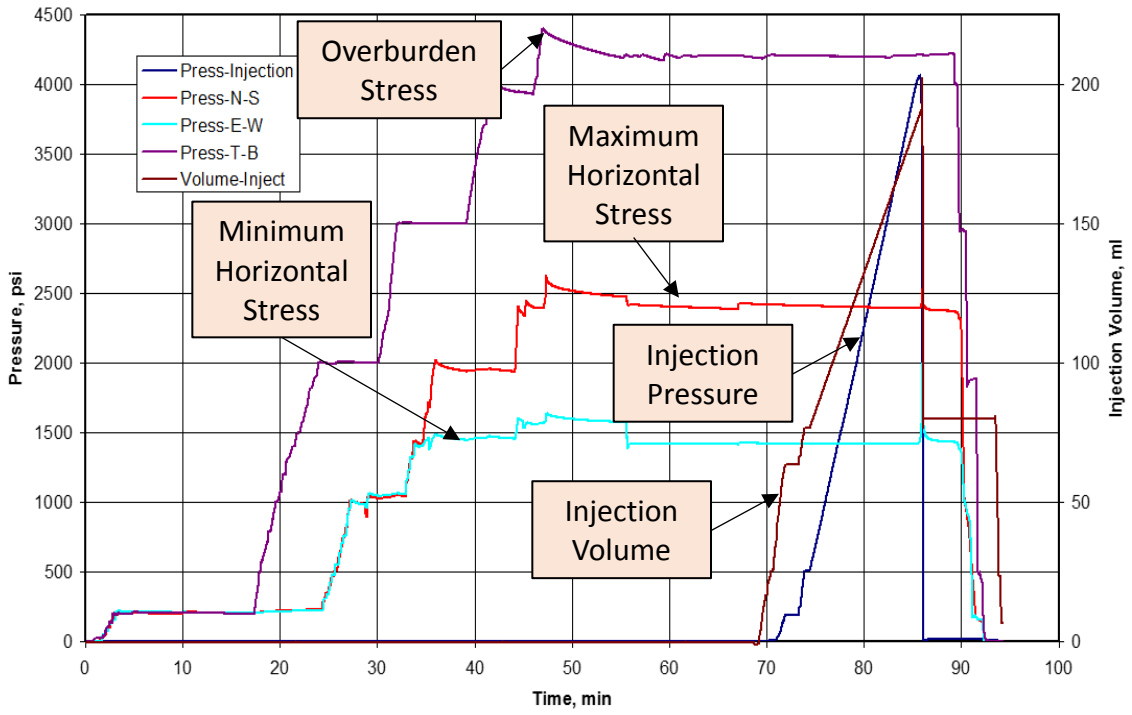

Figure 6.2 – Time pressure treatment plot for block number 1 using a 1000 cP fluid. Note that fracture initiation does not begin until about minute 85 but by minute 86 the fracture has blown out the side of the block and injection must be immediately ceased.

6.2.1 Tip Processes

A triad of factors are not well understood in the propagation of fractures especially as they approach interfaces. This triad is: the fluid lag behind the fracture tip, the role of fracture intensity factor K_I, and fracture toughness, $K_{IC.}$ At the field scale it is often assumed that one factor or the other dominates the process and the others can be safely ignored, but at the laboratory scale all factors need to be better understood.

Estimates for the fluid lag range between an inch and about four inches. Questions arise as to whether this dimension is constant for a material, or dependent on the treatment parameters used during fracturing. The coupling of the linear elastic

fracture mechanics of tip processes and the elastic strain associated with a viscous fluid propping and extending the fracture are two very different processes. What determines how quickly they transition is the dimension of this fluid lag zone. If in fact this zone is several inches in size then if we are creating fractures of that half-length, almost all the fracture behavior is in this transition between different physics. We must better understand the interaction of these variables to predict and interpret laboratory scale hydraulic fracturing experiments.

Another factor that needs further study is the role of fracture intensity factor and how this behaves early in the fracture development and as the fracture approaches well coupled material interfaces where the fracture length can be quickly changing, be diverted, offset, or blunted. The ability for a fracture to cross a material interface depends on the amplifying effects of the fracture intensity factor but the dynamics of the fracture near the interface can rapidly diminish the available energy to cross the interface and cause it to change direction or simply arrest.

The last factor in this triad of variables worthy of more investigation is the role of fracture toughness. It is often assumed that this is an intrinsic rock property that can be measured and remains constant. Further, it is often assumed that the localized stress concentrations caused by the advancing fracture tip will overwhelm the fracture toughness and it can be ignored. This assumption is probably valid when considered at the field scale where the fracture length is 100's of feet and the fracture height is many 10's of feet. But fracture toughness may not in fact be an intrinsic rock property. It is probably scale dependent in which case, its importance and consideration for laboratory scale experiments warrants more attention than it is often given.

6.2.2 Operational Best Practices

Consistent scale modeling of the physical processes involved in hydraulic fracturing model experiments needs to be matured and adopted to make the results more consistent. Significant effort has been made along these lines but it is not yet widely adopted. The effort of de Pater et al. (1994) and Bunger et al. (2005) needs to be simplified and implemented in a consistent manner to avoid costly experimental results of dubious value.

Construction techniques to insure well bore isolation, pressure and acoustic transducer placement, and the synchronization of recording between disparate systems should be done to make the results more useable. The trick of using an epoxy plug at the base of the borehole to prevent horizontal fracture initiation is an excellent example of a best practice that should be extended across all labs. Better reproduction of the scoring along the well bore to assist in fracture initiation needs to be done to create more repeatable results.

Finally, the role of the wellbore storage affect is simply too large for scale model experiments. Down-hole fracture face check valves need to be used to eliminate the large energized fluid column that is difficult to control when pressures need to be relieved to prevent the fracture from blowing out the extent of the block. The drive to use smaller blocks for cost and ease of handling exacerbates the role of eliminating this well bore storage effect.

Other tips and tricks have been, or will be generated over time. But the researchers doing experimental work should commit more effort to sharing these best

practices versus allow them to become a competitive advantage for each of the different labs. Committing mistakes that jeopardize the experimental results is a huge waste of institutional funding and student researcher time. An effort to proactively share the factors that help insure laboratory success would improve the value from the industry experimental investments.

6.2.3 Microseismic Processing Advancements

There are some microseismic processing capabilities in industry that could be made available to improve the processing capabilities in the laboratory. But many of the processing challenges in the laboratory are unique to that environment and will require special processing capabilities to properly handle. Specifically, with the ability to precisely measure the velocity field of the sample, it is only appropriate that this complex velocity field be used in the processing.

With six free surfaces on a cube in the laboratory, there are many more free boundaries from which one would expect to get multiple reflections. This largely violates the assumption that everything is a direct arrival. The advantage is of course that a lab sample can be very accurately modeled to understand and predict these non-direct-arrival modes, for both the compressional and shear waves. In effect a modeled Greens function can be generated for the sample at each possible source and receiver location. This template can then be cross correlated with the actual recorded times series and in effect treat most, if not all, incoming energy as signal. Significant progress is being made by Rob Skoumal (personal communication, April, 2015) on his PhD working under Mike Brudzinski at Dayton University in Ohio but this work is as yet unpublished.

The potential value of seismic recording in the lab will be compromised until such processing technology is developed. Much of this is well aligned with the needs of industry as well, but with significant additional challenges not seen in the field. Using common processing and visualization technology between the lab and industry will leverage the mutual areas of expertise and provide a much broader base to fund the necessary research.

NOMENCLATURE

b_w = Characteristic frac width at wellbore (in.)

b^* = Characteristic width (in.)

C' = modified Carter leakoff coefficient (in/sec$^{1/2}$) ($C' = 2C_l$)

C_l = Carter leakoff coefficient (in/sec$^{1/2}$)

$E = \text{Young's modulus}$ (psi)

E' = plane strain modulus (psi) ($E' = \frac{E}{4(1-\nu^2)}$)

$\bar{E}$ = plane strain modulus (psi) defined as $\bar{E} = \frac{E}{4(1-\nu^2)}$

i = injection rate (in^3/sec)

K_I = stress intensity factor (psi·in$^{1/2}$)

K_{IC} = fracture toughness (psi·in$^{1/2}$)

K' = defined as (psi·in$^{1/2}$) $K' = 4\left(\frac{2}{\pi}\right)^{1/2} K_{IC}$

N_t = Experimental time

N_Γ = Crack energy

$N_{\bar{E}}$ = Elastic deformation

N_{C_l} = Leakoff

$N_{\sigma_{hmin}}$ = Confining stress

p_{net} = net pressure (psi)

p^* = Characteristic net pressure (psi)

Q_0 = injection rate (in^3/sec)

r_w = wellbore radius (in.)

r_f = fracture radius (in.)

t = experiment time (sec)

$\mathbf{M} = \left(\frac{t_m}{t}\right)^{2/5}$ = system invariant

$\mathbf{\Sigma} = \left(\frac{t}{t_0}\right)^{1/5}$ = system invariant

$\mathbf{C} = \left(\frac{t}{t_c}\right)^{3/10}$ = system invariant

t_m, t_0, t_c = characteristic time scales

Sr_w = Wellbore scaling factor

St = Time scaling factor

Si = Injection scaling factor

Sμ = Viscosity scaling factor

SK_{IC} = Fracture toughness scaling factor

SC_l = Leakoff scaling factor

$S\sigma_{min}$ = Confining stress scaling factor

$\gamma_r, \gamma_p, \gamma_b$ = functional coefficients (.083, 1, and 1 here)

Γ = separation energy (lbF/in)

μ = viscosity (cp)

μ' = channel viscosity ($\mu' = 12\mu$) (cp)

v = Poisson's ratio

ω = effective fluid lag zone (in.)

σ_{hmin} = minimum confining stress orthogonal to fracture face (psi)

σ_0 = confining stress orthogonal to the fracture face (psi)

τ^*= Characteristic time (sec)

$\varphi_1 = \frac{t_m}{t_0}$ = simplified existence criteria

$\varphi_2 = \frac{t_0}{t_c}$ = simplified existence criteria

REFERENCES

Alqahtani, N. B. 2010. “3D Finite Element Modeling of Laboratory Hydraulic Fracture Experiments”, MS Thesis, Colorado School of Mines, Colorado, USA.

Athavale, A. S. 2007. “Experimental Study of Hydraulic Fracture Propagation Processes in Laminated Reservoirs”, MS Thesis, Colorado School of Mines, Colorado, USA.

Bahorich, B., Olson, J. E., and Holder, J. 2012. “Examining the Effect of Cemented Natural Fractures on Hydraulic Fracture Propagation in Hydrostone Block Experiments”. SPE 160197 presented at the Annual Technical Conference and Exhibition held in San Antonio, Texas, USA, 8-10 October 2012.

Bunger, A.P., Jeffrey, R.G. and Detournay, E. 2005. "Application of Scaling Laws to Laboratory-Scale Hydraulic Fractures". ARMA/USRMS Paper No.05-818, Prepared for presentation at the 40th US symposium on Rock Mechanics (USRMS): Rock Mechanics for Energy, Mineral and Infrastructure Development in the Northern Regions, held in Anchorage, Alaska: p. 1-8.

Carter, E. 1957. In. Howard, G. and C. Fast, editors, Drilling and Production Practices: p. 261-270, American Petroleum Institute, Tulsa, OK.

Casas, L. 2005. "Large Scale Hydraulic Fracturing Test on a Rock with Artificial Discontinuities", MS Thesis, Colorado School of Mines, Colorado, USA.

Cleary M. P. 1978. Primary Factors Governing Hydraulic Fractures in Heterogeneous Stratified Porous Formations. Paper 78-Pet-47 presented at the 1978 ASME ETC Conference, Houston, Texas, USA, 5-9 November.

Chudnovsky, A., Fan, J., Shulkin, Y., Dudley, J.W., Nichols, W.B., and Wong, G.K. 2001. "Hydraulic Fracture Containment in Layered Media, Experiment and Computer Simulation", Rock Mechanics in the National Interest, Tinucci & Heasley (eds), ISBN 90 2651 827 7, p. 273-279.

de Pater, C.J., Cleary, M.P., Quinn, T.S., Barr, D.T., Johnson, D.E. and Weijers, Leen 1994a. "Experimental Verification of Dimensional Analysis for Hydraulic Fracturing". SPE Paper No. 24994, SPE Production and Facilities (November 1994): p. 230-238.

Dong, Z., S. A. Holditch, D. A. Mcvay, and W. B. Ayers 2011. “CSUG / SPE 148365 Global Unconventional Gas Resource Assessment.” In *The Canadian Unconventional Resources Conference*, 16. Calgary, Alberta, Canada: CSUG/SPE 148365.

Energy Information Administration, “World Wide Unconventional Natural Gas Reserves”. http://www.eia.gov/naturalgas/reports.cfm#/T170,T82, 2009

Ferraris, C. F., “Concrete Mixing Methods and Concrete Mixers: State of the Art”, Journal of Research of the National Institute of Standards and Technology, Vol. 106, No. 2, 391-399, March-April 2001.

Fisher, M.K., Wright, C.A., Davidson, B.M., Goodwin, A.K., Fielder, E.O., Buckler, W.S. and Steinsberger, N.P. 2002. "Integrating Fracture Mapping Technologies to Optimize Stimulations in the Barnett Shale". SPE Paper No. 77441, Presented at the SPE Annual Technical Conference and Exhibition held in San Antonio, Texas (September 29 - October 2): p. 1-7.

Fisher, K. and Warpinski, N. R. 2011. “Hydraulic Fracture-Height Growth: Real Data”. SPE Paper No. 145949 presented at the SPE Annual Technical Conference, Denver, CO, USA, 30 October – 2 November, 2011.

Fortin, J., Stanchits, S., Dresden, G. and Gueguen, Y. 2006. “Acoustic Emission and Velocities Associated with the Formation of Compaction Bands in Sandstone”. Journal of Geophysical Research, Vol. 111, B10203.

Geertsma, J. and de Klerk, F. A.: “Rapid Method of Predicting Width and Extent of Hydraulically Induced Fractures,” *JPT* (Dec. 1969) 1571-81; *Trans.*, AIME, 246.

Goncalves da Silva, B., Moradian, Z., Li, B., Germaine, J., and Einstein, H.: “Development of a test set up capable of producing hydraulic fracturing in the laboratory with image and acoustic emission monitoring”, ARMA 15-141, presented at the 49th US Rock Mechanics/Geomechanics symposium held in San Francisco, CA 28 June – 1 July, 2015.

Green, S. J.: Personal Communication, Salt Lake City, January 2015

Groenenboom, J. 1998. "Acoustic Monitoring of Hydraulic Fracture Growth", PhD Dissertation, Section of Applied Geophysics, Faculty of Applied Earth Sciences, Delft University of Technology.

Groenenboom, J., van Dam, D. B., and de Pater, C. J. 2001. “Time Lapse Ultrasonic Measurements of Laboratory Hydraulic Fracture Growth: Tip Behavior and Width Profile”. SPE Paper No. 68882, p. 14-24.

Howard, G. C. and Fast, C. R.: Hydraulic Fracturing, Society of Petroleum Engineers of AIME, Monograph 2, New York City 1970.

Ishida, T. 2001. “Acoustic emission monitoring of hydraulic fracturing in laboratory and field”. Elsevier: Construction and Building Materials, Vol. 15, 2001, pages 283 – 295.

Jeffery, R. G., Zhang, X. and Thiercelin, M. 2009. “Hydraulic Fracture Offsetting in Naturally Fractured Reservoirs: Quantifying a Long-Recognized Process”. SPE 119351, presented at the SPE Hydraulic Fracturing Conference held in The Woodlands, Texas, USA, 19-21, January 2009.

Johnson, D. E. and Cleary, M. P. 1991. “Implications of Recent Laboratory Experimental Results for Hydraulic Fractures”. SPE Paper No. 21846, Presented at the Rocky Mountain Regional Meeting and Low Permeability Reservoirs Symposium held in Denver, CO (April 15-17): p. 413-428

Kirsch, E. G., 1898. “Die Theorie der Elastizität und die Bedürfnisse der Festigkeitslehre”. Zeitschrift des Vereines deutscher Ingeniere 42, 797-807.

Mack, Marck G. and Warpinski, N.R. 2000. Mechanics of Hydraulic Fracturing. Reservoir Stimulation. M. J. Economides and K. G. Nolte. Chichester, UK, John Wiley & Sons Ltd. Third Edition: p. 6-1, 6-49.

Miskimins, J.L. and Barree, R.D. 2003. "Modeling of Hydraulic Fracture Height Containment in Laminated Sand and Shale Sequences". SPE Paper No. 80935, Prepared for presentation at the SPE Production and Operations Symposium held in Oklahoma City, Oklahoma, U.S.A. (March 22-25): p. 1-11.

Molenda, M., Brenne, S., Stoeckhert, F., and Alber, M. 2014. “Acoustic Emission Monitoring of Laboratory Scale Hydraulic Fracturing Experiments”. Poster 17 presented at the 31st Conference of the European Working Group on Acoustic Emission (EWGAE) held in Dresden, Germany, September 3 -5.

Nuller, B., Ryvkin, M., Chudnovsky, A., Dudley, J. W., and Wong, G. K. 2001. “Crack interaction with an interface in laminated elastic media”. American Rock Mechanics Association. ARMA Conference Paper No. 01-0289.

Perkins, T. K. and Kern, L. R.: “Widths of Hydraulic Fractures,” *JPT* (Sept. 1961) 937-49; *Trans.*, AIME, 222.

Potluri, N., Zhu, D., and Hill, A. D. 2005. “Effect of Natural Fractures on Hydraulic Fracture Propagation. SPE Paper No. 94568. Presented at the SPE European Formation Damage Conference held in Scheveningen, The Netherlands, 25-27 May 2005.

Savic, M., Ziolkowski, A. M., and Cockram, M. J. 1991. “Acoustic Monitoring of Laboratory Scale Dynamic Processes Under High Pressure,” expanded abstract, 61st SEG meeting, Houston.

Savic, M. and Cockram, M.J. 1993. "Active Acoustic Monitoring of Laboratory-Scale Hydraulic Fracturing Experiments". SPE Paper No. 26263: p.1-8.

Sonnenberg, S. A., and R. J. Weimer, 1981, “Tectonics, sedimentation, land petroleum potential, northern Denver basin, Colorado, Wyoming, and Nebraska”: Colorado School of Mines Quarterly, v. 76, p. 35–36.

Stanchits, S., Fortin, J., Gueguen, Y. and Dresden, G. 2009. “Initiation and Propagation of Compaction Bands in Dry and Wet Bentheim Sandstone”. Pure and Applied Geophysics, 166 (2009) 843-868.

Stanchits, S., Mayr, S., Shapiro, S. and Dresden, G. 2011. “Fracturing of Porous Rock Induced by Fluid Injection”. Tectonophysics, 503 (2011) 129-145.

Stanchits, S. (2015) Personal communication, Salt Lake City, January, 2015.

Stoeckhert, F., Molenda, M., Brenne, S., and Alber, M. 2015. “Fracture propagation in sandstone and slate – Laboratory experiments, acoustic emissions, and fracture mechanics”. Journal of Rock Mechanics and Geotechnical Engineering, Volume 7, Issue 3, June 2015, pages 237-249.

Teufel, L. W. 1979. An Experimental Study of Hydraulic Fracture Propagation in Layered Rock. PhD Dissertation, Texas A&M University, College Station, Texas.

Teufel, L. W. and Clark, J. A. 1984. Hydraulic Fracture Propagation in Layered Rock: Experimental Studies of Fracture Containment. SPE Journal 24 (1): 19-32. SPE-9878-PA.

Vincent, M. C., 2013. “Five Things You Didn’t Want to Know about Hydraulic Fractures”, ICHF-2013-045. International Society of Rock Mechanics Conference Paper, 2013.

Warpinski, N. R., Tyler, L. D., Vollendork, W. C., and Northrop, D. A. 1981. “Direct Observation of a Sand Propped Hydraulic Fracture”. Sandia National Laboratories Report No. SAND81 0225. Livermore, CA (May).

Warpinski, N. R., Clark, J. A., Schmidt, R. A., and Huddle, C. W. 1982. “Laboratory Investigation on the Effect of In-Situ Stresses on Hydraulic Fracture Containment”, Society of Petroleum Engineers Journal, SPE Paper No. 9834 (June, 1982).

Warpinski, N.R. 1985. "Measurement of Width and Pressure in a Propagating Hydraulic Fracture". SPE Paper No.11648, Society of Petroleum Engineers Journal (February 1985): p. 46-56.

Warpinski, N. R., Branagan, P. T., Sattler, A. R., Cipolla, C. L., Lorenz, J. C., and Thorne, B. J. 1990. “Case Study of a Stimulation Experiment in a Fluvial, Tight-Sandstone Gas Reservoir”. SPE Production Engineering, November 1990.

Warpinski, N. R., Wolhart, S. L., and Wright, C. A. 2001. “Analysis and Prediction of Microseismicity Induced by Hydraulic Fracturing”. Paper SPE No. 87673 presented at the SPE Annual Technical Conference and Exhibition, New Orleans, Louisiana, USA, 30 September – 3 October, 2001.

Weijers, L., de Pater, C. J., Owens, K. A., and Kogsbøll, H. H. 1992. “Geometry of Hydraulic Fractures Induced from Horizontal Wellbores”, SPE paper 25049 presented at European Petroleum Conference held in Cannes, France, 16-18 November, 1992.

Wu, K. and Olson, J. E. 2014. “Mechanics Analysis of Interaction Between Hydraulic and Natural Fractures in Shale Reservoirs”. URTeC 1922946 presented at the Unconventional Resources Technology Conference held in Denver, Colorado, USA, 25-27 August 2014.

APPENDIX A

Summaries of Prior FAST Consortium Work

LARGE SCALE HYDRAULIC FRACTURING TEST ON A ROCK WITH ARTIFICIAL DISCONTINUITIES, Luis Casas, 2005

The Casas thesis was the first in a series of research projects sponsored by the FAST Consortium at the Colorado School of Mines to investigate height containment in the presence of material interface changes when being hydraulically fractured. His work was experimental utilizing a large 30” x 30” x 36” block of Colton sandstone.

The block was prepared by creating two parallel channels through about two thirds of the block; one filled with epoxy and the other with grout. The experiment was designed to stress the block and create a hydraulic fracture that would not intersect either of the two created discontinuities, then reverse stresses and fracture the block again forcing the fracture to intersect the two very different discontinuities.

Several pressure probes were drilled and epoxied into place to be able to detect and measure how the pressures changed as the fracture tip and fluid filled fracture passed the probe. This turned out to be one of the most interesting aspects of the research with actual fracture rate calculations possible and the measurement of the fluid lag zone prior to the migrating fluid front.

Aspects of the fracture pressure history and geometry were recorded and showed very different results depending on if the fracture intersected the permeable but hard grout channel, or the impermeable and relatively plastic epoxy filled one. Proper

experimental scaling of treatment variables allowed for good quality data and the use of a high viscosity 600,000 cp silicon fluid with extremely low leak-off properties. This gave confidence for the design of the next experiment in the sequence to use smaller and much less expensive blocks to test.

EXPERIMENTAL STUDY OF HYDRAULIC FRACTURE PROPAGATION PROCESSES IN THINLY-LAMINATED RESERVOIRS, Amrut Athavale, 2007

Following the successful work of Casas, the next project in the series was to test the behavior of hydraulic fractures in a layer medium. The decision was taken to try and do this work on much smaller 11” x 11” x 15” blocks. Two were fabricated for the work. One was a simple monolithic cement block. The other was a complicated seven layer block with three layers of Lyons sandstone interlayered with two types of cement and a layer of epoxy.

One specific goal of these tests was to understand the effects of layer-to-layer cohesion. Hence careful construction was done to allow the cement to bond with the sandstone blocks but also to create interfaces where this bonding was prevented. Virtually every combination of material contrast and bonding was present in the carefully designed block.

As would be expected, very different fracture response and geometry occurred at the different layer interfaces of the block. However, in hindsight, the block may have had too many variables to completely unravel in the complex pressure history of the experiment. This led to a substantial effort in finite element modeling of the block to understand the stress state at each of these boundaries prior to the hydraulic fracture.

This finite element modeling was one of the most significant pieces of the research. Huge stress contrasts where found to be induced across the material property boundaries due to the conversion of stresses through Poisson ratio changes. This helped explain much of the complexity encountered in the data and reinforced other research that showed that not only are the material property differences important in understanding how the fracture will behave in close proximity to the interface, but perhaps the stress contrasts are even more important.

Proper model scaling of parameters was used and the selection of a 100,000 cp treatment fluid was used. This confirmed that these parameters could be scaled to the smaller block size and hence numerous experiments could be run at a lower cost than that incurred in the larger block test done by Casas earlier. The important of finite element modeling of the stress state was also proven and utilized in later experiments.

3D FINITE ELEMENT MODELING OF LABORATORY HYDRAULIC FRACTURE EXPERIMENTS Naif Alqahtani, 2010

Building on the results of the prior three laboratory tests, the need for more thorough modeling of the stress states was justified. Three different experiments in the FAST Consortium had covered the use of seven different block configurations. Some of these were only slightly different from each other but still provide ample conditions to model the differences not only in the material configuration of the bocks but also the stress conditions they were put under, how they were loaded (stress application in the test frame) and what the configurations of the wellbores were.

The sequence of analysis was repeated for each of the block configurations started first with a monolithic block stressed through the loading sequence used in the laboratory and all stresses evaluated. Then the analysis moved to layered blocks with the different materials in each of the layers to represent those used in the actual laboratory experiments. Finally, the wellbores were introduced.

It was the addition of the wellbores that created some of the more interesting results. Unfortunately, it is impossible to create an isolated wellbore for laboratory conditions to mimic what is done in the field. In the field we drill the hole into a pre-stressed sequence of laminated layers and cement it in place creating the isolation between layers. This cannot be done in the laboratory where we drill the hole and cement (with epoxy) the stainless steel “casing” into the unstressed sample. Then the combined unit is placed into the tri-axial press and put under stress.

The wellbore, with all its known stress localization effects (hoop stress) also presents a significantly different material (steel) with very different properties from the surrounding rock layers. In effect, the epoxied steel casing strongly resists the primary vertical stress being applied to the rock. The effects of this were modeled and analyzed by Alqahtani.

Additional factors such as the rate of stress change in the sample were also addressed. The time dependence aspect was not previously addressed. Not only does the sequence of stress loading matter in getting to the final experimental designed stress state, but also the rate the stress changes occur and the time allowed for the stress state to stabilize all play roles in the operational planning for experimental lab work.

APPENDIX B

Data Disk Containing all Laboratory Data and Analysis

Name	Date modified	Type	Size
Block 1 Photos	11/1/2015 7:12 AM	File folder	
Block 2 Photos	11/1/2015 7:12 AM	File folder	
Explorer	11/1/2015 7:12 AM	File folder	
Block 1 TerraTek Report	8/26/2008 1:38 PM	Adobe Acrobat Doc...	1,353 KB
Block 1 Treatment Raw Data	8/26/2008 2:40 PM	Microsoft Excel 97-...	3,057 KB
Block 2 TerraTek Report	3/4/2015 4:15 PM	Adobe Acrobat Doc...	2,235 KB
Block 2 Treatment Raw Data	3/2/2015 2:44 PM	Microsoft Excel 97-...	9,696 KB
Block Test 1 MS Events - All Time - All Conf...	4/20/2015 9:42 AM	Microsoft Excel Wor...	876 KB
Block Test 2 MS Events - All time - All Confi...	4/20/2015 7:56 PM	Microsoft Excel Wor...	7,516 KB
Dissertation Defense Presentation	4/23/2015 2:08 AM	Microsoft PowerPoi...	5,759 KB
Explorer	4/21/2015 12:21 PM	7Z File	174,341 KB
Horizons	4/20/2015 7:15 PM	Microsoft Excel Wor...	9 KB
PhD Dissertation V1.7	1/17/2016 8:54 PM	Microsoft Word Do...	39,761 KB
Properties - Scaling - Seismic Location	4/7/2015 8:06 AM	Microsoft Excel 97-...	15,649 KB
Well Spot X1000	4/19/2015 1:43 PM	Microsoft Excel Wor...	8 KB

The contents of the included data files is listed above and named to make the contents as easy to find as possible. A brief description of each file/sub-directory is listed below:

- “Block 1 Photos” and “Block 2 Photos” are sub-directories containing the photos taken of the two Blocks both before and after the hydraulic fracture treatments.
- “Explorer” is a sub-directory contains all the necessary files to run the Transform Software 3D visualization software that is preloaded with all the microseismic and pressure treatment data presented in this dissertation. The user can install and run this software without requiring an additional license and can both manipulate and create all the displays presented in the dissertation.

- “Block 1 TerraTek Report” and “Block 2 TerraTek Report” are the final pdf reports that TerraTek delivered at the conclusion of the two respective block experiments.
- “Block 1 Treatment Raw Data” and “Block 2 Treatment Raw Data” are Excel files containing the pressures recorded and the injected volumes for each hydraulic fracture treatment respectively. Note that the pressure curves are not perfectly synchronized with the microseismic files.
- “Block Test 1 MS Events – All Time – All Confidence” and “Block Test 2 MS Events – All Time – All Confidence” are Excel files containing the final microseismic localized events and their associated uncertainties (called the LUCY number). The files have a time adjustment column to synchronize them with the treatment files. These files have had all events physically outside the boundaries of the block removed.
- “Dissertation Defense Presentation” is the PowerPoint file of the 30 minute presentation presented during the dissertation defense.
- “Explorer” is a ZIP file containing the contents of the “Explorer” sub-directory discussed above.
- “Horizons” and “Well Spot X1000” are Excel files containing the information to initialize and build the 3D cube complete with the treatment well, well tops at the lithologic boundaries, and the lateral extents of the horizons through those well tops.
- “Properties – Scaling – Seismic Location” is an Excel spreadsheet with three workbooks for calculating the physical properties of the block, the scaling factor

for the laboratory scale, and the analysis to optimize receiver locations to minimize simultaneous arrival times to stabilize the processing of the microseismic event locations.

- “PhD Dissertation V1.7” is the MS Word file containing the published dissertation.